Active Magnetic Bearings used as an Actuator for Rotor Health Monitoring in Conjunction with Conventional Support Bearings

Travis Joel Bash

Thesis submitted to the faculty of the Virginia Polytechnic Institute and State University
in partial fulfillment of the requirements for the degree of

Master of Science
In
Mechanical Engineering

Dr. Mary Kasarda
Dr. Gordon Kirk
Dr. Don Leo

June 27, 2005
Blacksburg, VA

Keywords: active magnetic bearings, health monitoring, shaft rub, actuator, crack, modal analysis

Active Magnetic Bearings used as an Actuator for Rotor Health Monitoring in Conjunction with Conventional Support Bearings

Travis Joel Bash

ABSTRACT

This thesis describes the test rig and results from a project expanding the field of rotor health monitoring by using Active Magnetic Bearings (AMBs) as actuators for applying a variety of known force inputs to a spinning. Similar to modal analysis and other nondestructive evaluation (NDE) techniques which apply input signals to static structures in order to monitor responses; this approach allows for the measurement of both input and output response in a rotating system for evaluation. However, unlike these techniques, the new procedure allows for multiple forms of force input signals to be applied to a rotating structure. This technique is used on a rotating shaft supported in conventional bearings with an AMB actuator added to the system. This paper presents the results from this project including shaft rub and notch. An EDM notch was also tested to attempt a breathing scenario similar to breathing cracks.

Acknowledgements

I would like to first thank my advisor Dr. Mary Kasarda for the many opportunities over the last four years that she has given me. She has always been understanding of any needs that I might have had, and always willing to help in any way that she could. If it were not for her, I would not be graduating with a Masters degree. I would also like to thank Dr. Kirk for all his teachings and assistance. He is always willing to talk rotordynamics and to help out in any way that he can. I will miss the annual rotor-palooza! Thanks also to Dr. Leo for taking on the responsibility as my other committee member.

I would next like to thank my wife Nicole. She has always been supportive and encouraging of my choice to pursue a Masters degree. Without her by my side cheering me on, this Masters degree would have been a flop. I guess this means her Masters is next, or maybe a law degree. I would also like to acknowledge my Mom and Dad and thank them for always offering to help in any way that they could. My parents have always supporting me and the decisions that I have made. Thanks also to my brothers and sister who have always been kind and supportive and at least tried to act interested in my research. Who can forget to thank the in-laws. Well in truth, my wife's family has also done what ever was possible to help out during the past few years whether it was lawn mowing, changing transmissions, or baby sitting. Thanks also to my brother-in-law Jason. He has always boosted my confidence in the smallest and largest tasks that I have attempted. Jason has always helped me whether it be digging holes or building swing sets.

A special thanks goes out to Rob Prins. We have worked together for four years, and shared many laughs and stories. He was always willing and has helped me in numerous occasions at home and at school. Rob is also the most street savvy and logical guy I know and his advice shows it.

I would also like to thank the mechanical engineering staff for all the help these past two years. (Ben, Jamie, Lynn, Eloise, Cathy, Beth, Johnny, Timmy, James, Bill, and Randy) Every one of these people has helped me on more than one occasion.

Thanks finally to Joe Lakas. Joe sponsored me with free bearings from Timken for this research.

Table of Contents

List of Tables

List of Figures

Chapter One

Introduction

1.1 Introduction to health monitoring of rotating machinery

Health monitoring of rotating machinery is a field of study that describes and quantifies the running integrity of a rotating machine. Rotating machinery encompasses many different types of machines such as turbines, pumps, compressors, and generators. These types of machines generally require large investments of time and money to develop, and carry large responsibilities in the areas of power generation and transportation.

The purpose of health monitoring is to observe and prevent possible problems with a rotating machine before a failure occurs. This type of health monitoring is termed preventive, but the new industry aim is predictive. Instead of a machine receiving scheduled maintenance, predictive health monitoring would determine the level and type of damage a machine has and then predict how much longer the machine can safely continue to operate. In past preventive examples, a machine may have been taken off line only to learn that the damage was not severe enough to warrant a shut down. Unfortunately, the opposite scenario is also true, which has lead to loss of life.

Monitoring rotating machines is a mature field of study that has documentation as early as 1869 (Kirk, 2002). With the introduction of non-contact displacement probes, also known as proximity probes, direct displacement data could be taken along a shaft. This was extremely valuable because up until this time most monitoring came from velocity probes at the bearing caps. This time period also includes the introduction of the computer, which was used to calculate frequency content from the displacement data. With the introduction of proximity probes and computer processing, vibration data from these probes have since been used to categorize particular machine faults to present day.

1.2 Research Objectives

The objective of this research was to construct a small rotor test rig supported in conventional bearings that could be used to simulate and determine machinery faults using an active magnetic bearing (AMB). Specifically, shaft crack and rub are the targeted faults under investigation. The AMB on this test rig serves not as a support device, but as an actuator to add force inputs to the rotor. This method of forcing a rotor has been done previously, but with rotors supported with magnetic bearings (Humphris, 1992). The goal of this research is to prove that conventional supported rotors with faults can be diagnosed with an AMB that is incorporated into the machine. AMB's could then be used as often as needed to test a machine for possible problems and damage. This data could be used to trend and predict the possible running time left on a machine or even heal the system by adding a corrective force.

1.3 Literature Review

Health monitoring of rotating machinery has been actively practiced for several decades in the aerospace, power generation and petrochemical process industries (Pusey,(1995), Eisenmann,(1998), Mitchell,(1993)). Most of the diagnostic methods used involve vibration monitoring simply because machinery distress very often manifests itself in vibration or a change in vibration pattern. The development of machinery diagnostic techniques have been motivated by the enormous economic incentive to keep rotating machinery operational. These techniques have successfully identified such problems as cracked shafts, loose assembly of components, and serious bearing defects well before these problems propagated into machine failures (Eisenmann, (1998), Eshleman, (1990)). These diagnostic techniques are so common in the rotating equipment community that numerous organizations and programs extensively support the use and development of these techniques including The Vibration Institute and its National Division, The Society for Machinery Failure Prevention Technology (MFPT), The American Helicopter Society, and the COMADEM 13th International Congress and Exhibition on Condition Monitoring and Diagnostic Engineering Management which was held in Houston, TX in December of 2000.

In addition to the general class of machinery health monitoring, there is a significant body of literature involving the analysis and diagnostics of shaft cracks. Papadopoulos (1992) discusses unambiguous coupling due to the presence of a shaft crack between longitudinal, torsional, and bending vibrations obtained with a harmonic sweeping excitation throughout a large frequency range. This experimental portion of this work was completed on a stationary beam. Iwatsubo (1992) presented work detailing the excitation of a rotor by external forces at specific frequencies for crack detection. In this study, a laboratory rotor was rotated at slow speeds and forces were applied by an exciter mounted to the shaft through a rolling element bearing. There are numerous references to detection of cracks in shafts. A good recent reference documenting many of the work in this area is Sabnavis (2004). The new magnetic actuator technique presented here allows for advances to these earlier studies and facilitates their application to a broader class of rotating machinery for actual on-line analysis.

This research is also focused on detecting shaft rub for both non-running and running speeds. Bently (1983) presented work that showed partial rubs with subharmonics of running speed and forward and backward precession due to full rub. At shaft speeds up to twice the natural resonance frequency, the fundamental rub frequency will coincide with the shaft speed with multiples at 2X, 3X, etc (Reliability Direct). The work presented here is more directed at constant speeds instead of using run up or run down data.

The procedure presented here is an extension of work performed by Humphris (1992). In his work, Humphris utilized the AMBs that were supporting a rotor as a source for applying various perturbations to the shaft and monitoring the response for health diagnosis. In addition to expanding the work by Humphris, the work here focuses on applying the approach through a separate actuator for machines not supported magnetically. This allows for a much broader application of the technique to the general class of rotating machinery. Additional work similar to Humphris was done by Pottie (1999), which included finding modal parameters of a destaged boilerfeed pump supported with AMBs.

While the addition of AMB actuator(s) to a rotating machine for improved health monitoring is not without cost, the actuators can potentially be economically justified by utilizing

them to improve rotor dynamic performance. For example, Kasarda (1991) has demonstrated that the midspan use of an AMB as a "third bearing," or magnetic damper, for the reduction of up to three modes of rotor synchronous vibration.

Chapter Two

Experimental Set-up and Procedure

2.1 Active Magnetic Bearing Overview

An Active Magnetic Bearing (AMB) is a type of machine that incorporates electromagnets to generate attractive forces. AMB's have many different types of applications, but for this research they will be used as a non-contact actuator to apply different forcing functions to a shaft. The goal of this research is to demonstrate that AMB's can be used to find faults in a conventional supported rotor while it is running by applying forces to the shaft and monitoring the response.

As the name suggests, AMBs are typically used as bearings, and have the unique feature of no contact between the stationary housing called the stator and the rotating target called a rotor. AMBs can only produce attractive forces, therefore, a closed loop controller with additional hardware components are required to maintain stable operation of the bearing. A simple example of a magnetic bearing can be seen in Figure 2.1 where one axis of force exists. If the controller monitors a change in rotor position, the controller will send a correction signal to the power amplifier, which then sends the appropriate current correction to the electromagnet coils. The example shown in Figure 2.1 only allows 1-D control, and even that control is balanced with gravity. A better scenario is multiple axes with the ability to produce attractive forces in both directions along an axis. Figure 2.2 shows a 2-D actuator, which is a better representation of the bearing used in this research.

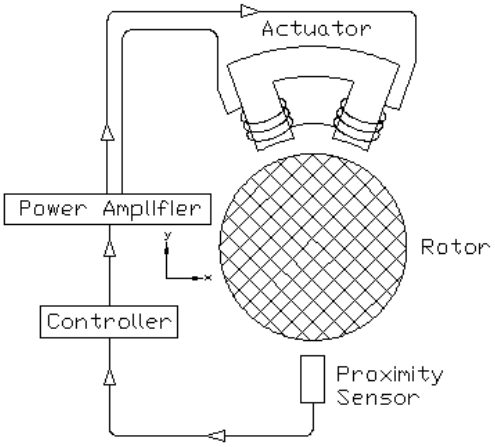

Figure 2.1. 1-D AMB actuator.

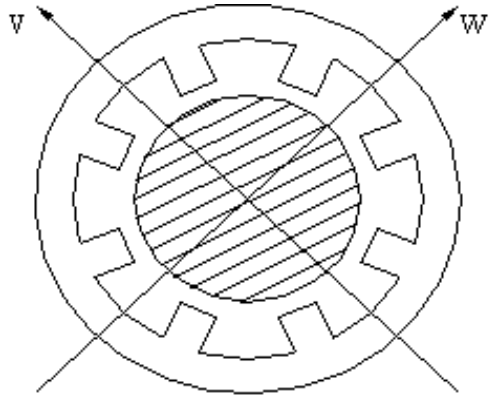

Figure 2.2. 2-D AMB actuator.

2.2 Rotor test rig

Due to the complex nature of active magnetic bearing design, the AMB used for this research was purchased from Revolve Magnetic Bearing Inc. This system included two magnetic stators and rotors as well as the PID controller and MBScope 2000™ software for parameter control. Revolve™ also supplied two balance disks as well as a base plate for mounting all the components.

The AMB used for this research is an 8-pole heteropolar design with two axes of control and four poles per axis. Figures 2.3 and 2.4 show the axis orientation of the magnetic bearing with the W axis positioned at 45 degrees and the V axis at 135 degrees. The air gap between the rotor and the stator is 0.015 inches (0.381 mm), while the catch bearing to shaft clearance is 0.005 inches (0.127 mm). Catch bearings are necessary to prevent the rotor from contacting the stator, which is called smearing the laminations. This condition can degrade magnetic bearing performance. A 0.015 inch air gap will allow a maximum static force of 60 lbf (266.9 N) at 1.25 tesla for each magnetic bearing actuator. Additional AMB geometry can be seen in Table 2.1.

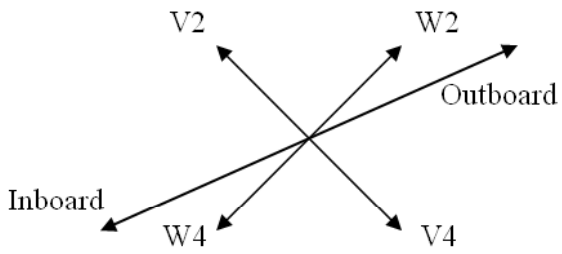

Figure 2.3. Magnetic bearing axes.

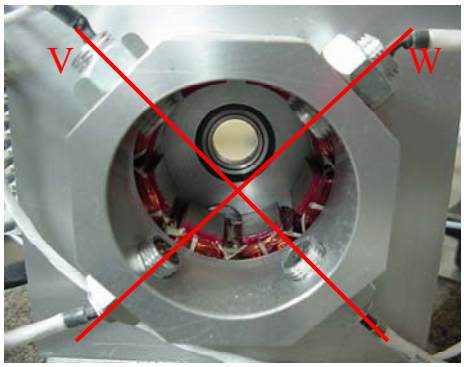

Figure 2.4. Picture of magnetic actuator.

Table 2.1. Active magnetic bearing geometry.

Bearing Geometry	Imperial Units		Metric Units	
Stator OD	4.528	in	115.011	mm
Stator ID	1.92	in	48.768	mm
Back Iron Width	0.519	in	13.183	mm
Pole Height	0.784	in	19.914	mm
Small Pole Width	0.514	in	13.056	mm
Pole Offset Angle	22.5	deg	0.393	rad
Slot Width (@ID)	0.233	in	5.918	mm
Stator Stack Length	0.85	in	21.59	mm
Rotor OD	1.89	in	48.006	mm
Rotor Lamination ID	0.81	in	20.574	mm
Nominal Gap	15	mils	0.381	mm

One key feature of active magnetic bearings is the ability to change mechanical properties of the bearing. The PID controller supplied has many different software programs such as position calibration and trending analysis, but the most commonly used is the Single In Single Out (SISO) Tune program. SISO Tune allows an operator to change, on a per axis basis, the proportional, derivative, and integral gains, which correspond to stiffness, damping, and position accuracy. Other features available include set point change, which is position within the bearing, and top and bottom bias currents for each axis. All of the above mentioned parameters are values that control closed loop operation of the bearing and can be seen in Table 2.2. For this research, one other important parameter was needed. This was open loop signal injection. Signal injection allows a user to send a voltage signal to the magnetic bearing independent of the closed loop control. There are two types of signal injection. The first is called a post injection signal, which adds current after PID control, but before the power amplifiers. The second

method, which was used for this research, is called pre-injection. Pre-injection mimics a position error, and the PID controller attempts to correct this error with the appropriate current.

Table 2.2. AMB controller parameters.

PID Values	Value	Units
Integral Gain	125	n/a
Proportional Gain	80	n/a
Derivative Gain	0.05	n/a
Total Gain	0.0005	n/a
Top Bias	0.75	A
Bottom Bias	0.75	A
Set point	0	um

The test rig for this research, with the incorporated AMB, can be seen in Figure 2.5, and the diagram showing exact placement of components can be seen in Figure 2.6. This test rig is equipped with a variable speed permanent magnetic DC motor capable of 10,500 rpm. The rotor is supported by rolling element bearings and has a bearing span of 24 inches (610mm) and a shaft diameter of 0.625 inches (15.9mm). Attached to the rotor is a 2.75 lb (1.25kg) disk used for adding balance or unbalance to the system. This test rig is also outfitted with two inboard and two outboard Bently-Nevada® proximity probes located at approximately ¼ and ¾ span, which share the same angular placement as the magnetic bearing axes. The magnetic bearing uses four variable reluctance proximity probes that give one position per axis.

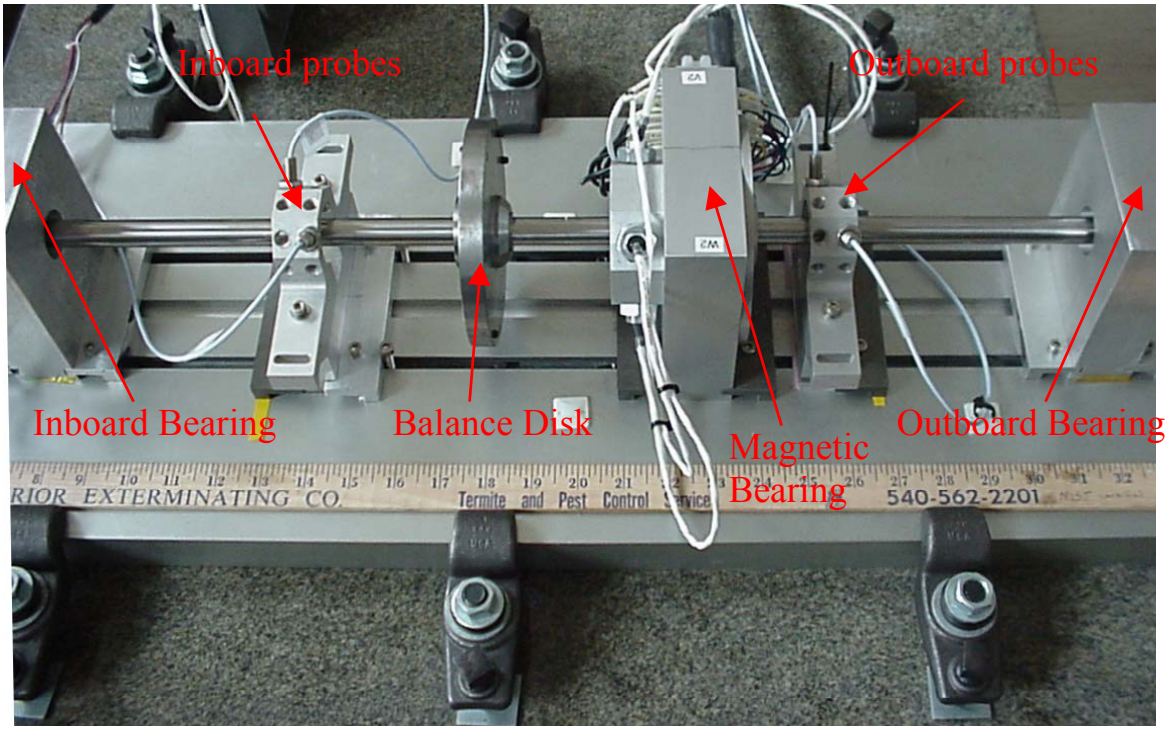

Figure 2.5. Picture of test rig in midspan AMB configuration.

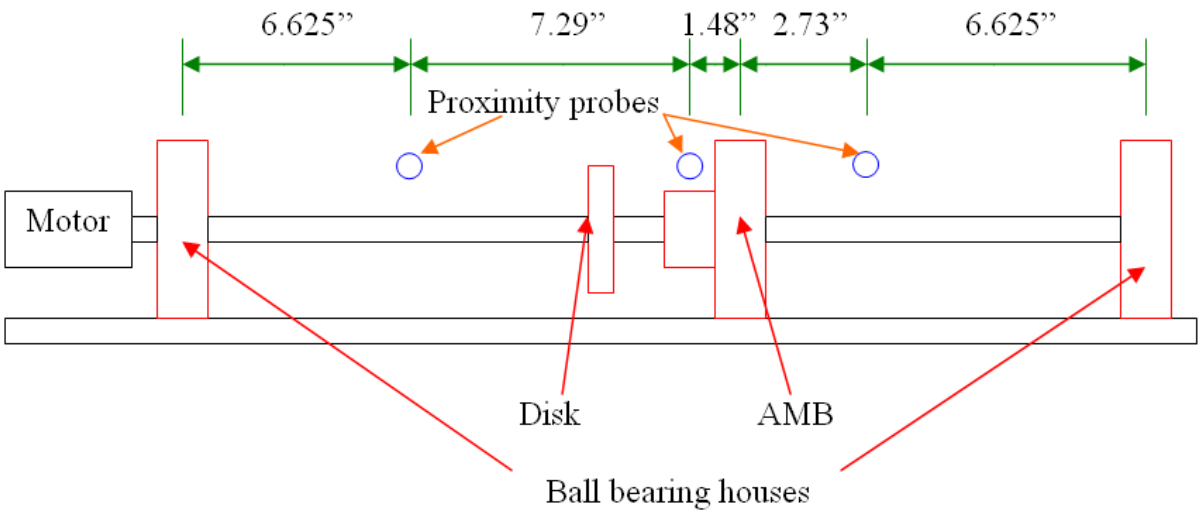

Figure 2.6. Diagram of test rig in midspan AMB configuration.

The test rig shown in Figure 2.5 is in the midspan configuration with the magnetic bearing near midspan of the shaft. This test rig was also configured with the magnetic bearing closer to the outboard bearing position shown in Figure 2.7, and the diagram in Figure 2.8. Two configurations were used for this research to show position effectiveness of the AMB, but most tests presented here were run with the midspan configuration.

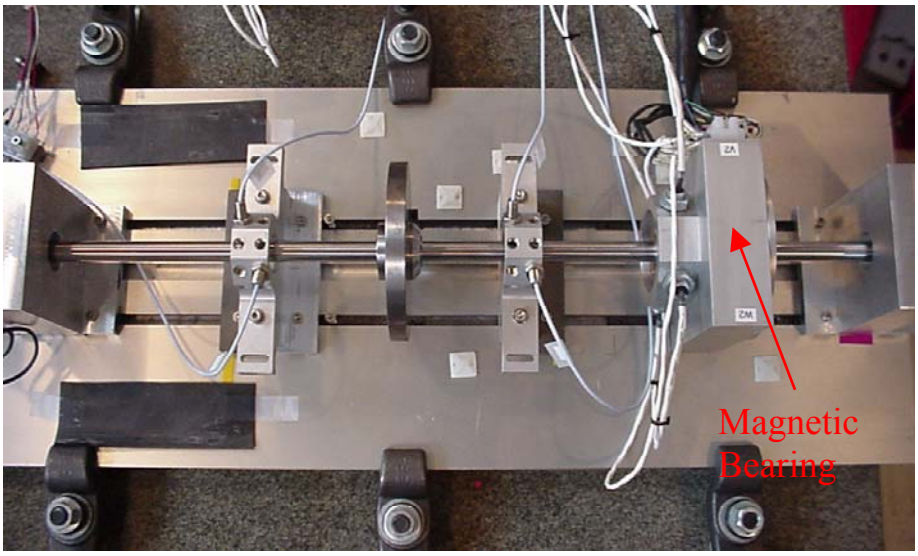

Figure 2.7. Picture of test rig with outboard AMB configuration.

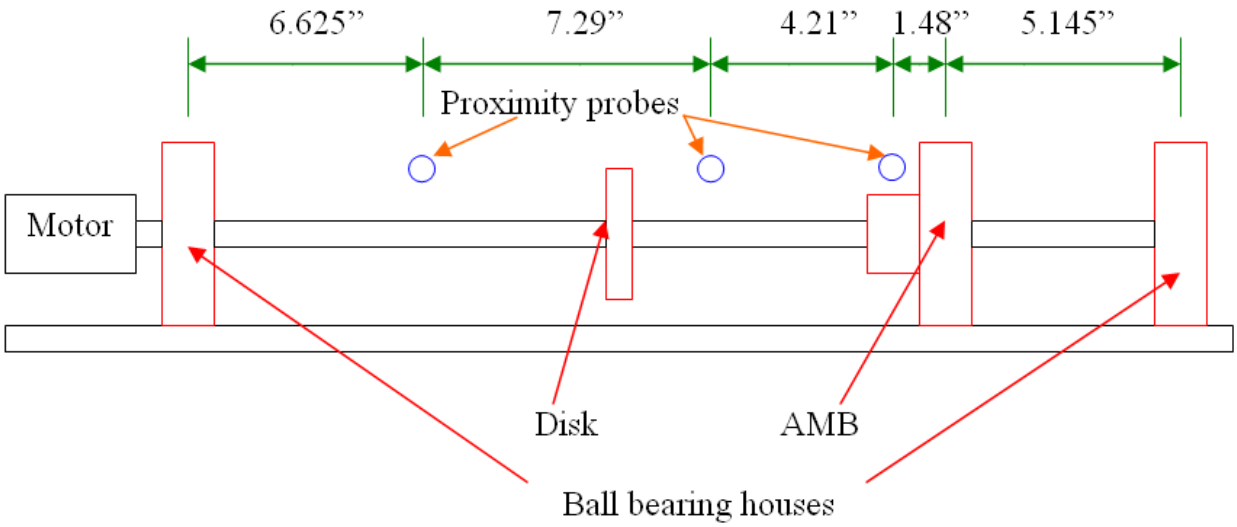

Figure 2.8. Diagram of test rig with outboard AMB configuration.

The test rig seen previously was used to investigate three types of rotor dynamic faults. These faults include shaft rub, large notch, and small notch, the latter two chosen to mimic shaft crack. The first fault investigated was shaft rub, which will be discussed next.

2.2.1 Shaft Rub Setup

One of the goals of this research was to investigate shaft rub. Shaft rub can occur in two ways. First, the shaft orbit grows until contact is made by a stationary component surrounding the shaft. Second, a surrounding component moves into the orbital path of the shaft. To mimic a shaft rub, a threaded brass screw was placed in the proximity probe mounts already installed on the test rig at the inboard and outboard locations. The screw had five possible radial positions at 0°, 45°, 90°, 135°, and 180° and two axial locations as seen in Figures 2.9 and 2.10. To simulate a rub, the brass screw was rotated until the desired contact was made.

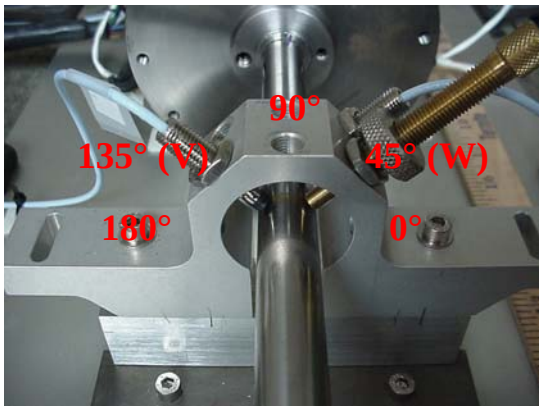

Figure 2.9. Radial rub locations.

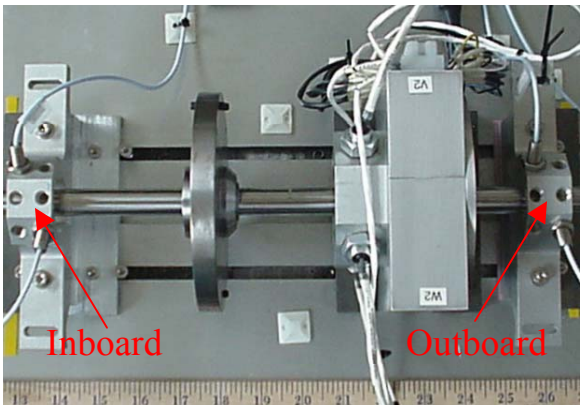

Figure 2.10. Axial rub locations.

2.2.2 Notch shaft setup

In an effort to approximate a shaft crack, a 0.025 inch (0.635 mm) wide notch was cut into the midspan of the shaft in three increments of 10%, 25%, and 40% of the shaft diameter. A picture of the final notch depth of 40% or 0.25 inch (6.35 mm) assembled on the test rig can be seen in Figures 2.11 and 2.12. Notch testing began with a "healthy" system, which means no damage. Then, 10% of the shaft diameter was removed and the system retested. This procedure was the same for the next two depths with the final product being a progressively worsening shaft. To the author's surprise, there was an additional complication from removing material from a shaft. There are some residual stresses in the shaft that cause the shaft to bow towards the notch. This problem of progressive bowing with damage did require up to 0.141 oz-in (9 gram-in) of balance weight to safely pass thru the first critical speed.

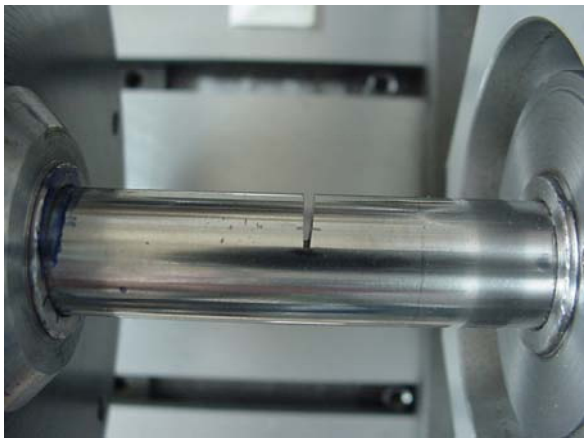

Figure 2.11 Close up of 40% notch.

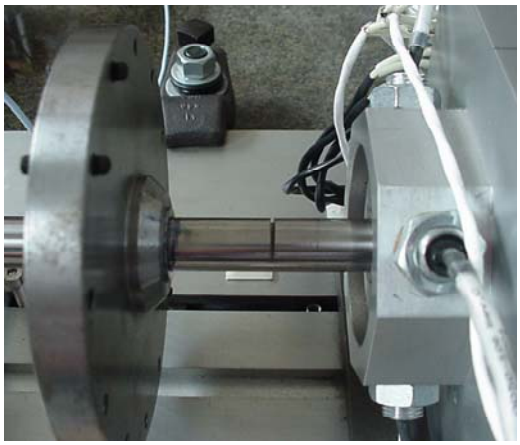

Figure 2.12. 40% notch from greater distance.

2.2.3 EDM shaft setup

The next step in mimicking a crack was to make the notch much smaller. This was done with a wire electric discharge machine (wire EDM). Wire EDM has 0.001 inch (0.0254mm) width cutting capability, but the shafts used for this research had notches made with 0.0022 inch (0.0559 mm) thick wire instead, due to availability. Even though the wire diameter is 0.0022 inch across, the wire EDM process results in some burn off, which left a final approximate notch width of 0.0027 inch (0.0686mm). It is important to realize that even though this notch is equivalent in diameter to a human hair, it is still not a crack. The hope was however that the notch would be sufficiently small enough to open and close simulating a breathing crack. To keep consistent with previous notch depths, EDM notches of 25% and 40% were made with an example of the 25% notch shown in Figures 2.13 and 2.14. As with the large notch, the EDM notches were made at midspan on the shaft, but testing occurred with the AMB positioned at the two locations previously mentioned.

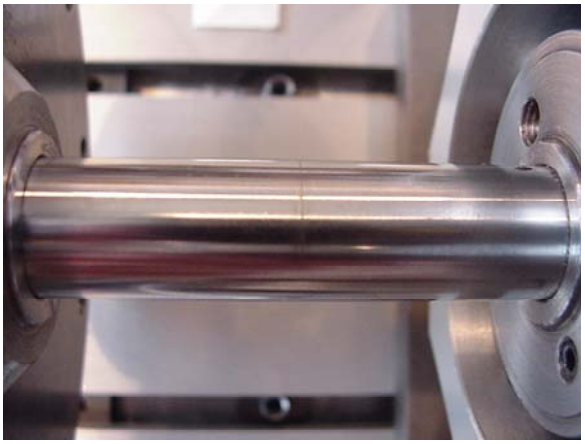

Figure 2.13. 25% EDM notch on test rig.

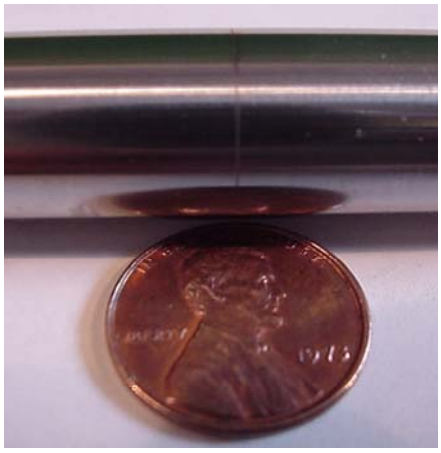

Figure 2.14. Zoomed 25% EDM notch.

2.3 Research Data acquisition

Testing during this research involved sampling voltages from the six proximity probes mounted on the test rig. Monitoring and recording this data was accomplished with two different data acquisition systems. The first system, shown in Figure 2.15, was Bently Nevada's® ADRE® 208 system, which is an industry standard for rotating machinery. ADRE® was used for run up and run down data as well as calculating Fast Fourier Transforms (FFTs) at different running speeds. The second system was a National Instruments PXI system fitted with a 4472B and 4461 data acquisition card shown in Figure 2.16.

Figure 2.15. Bently Nevada's® ADRE® data acquisition system.

Figure 2.16. National Instruments PXI chassis.

PXI systems are generally high performance systems that communicate to a computer thru a high speed serial cable into a PCI card. The 4472B card has eight simultaneously sampled channels and the 4461 card has two input and two output channels. Testing requires forcing output from the 4461 card to the signal injection of the AMB, and the 4472B records the resulting position data from the six position probes as well as the tachometer and forcing signal. Figure 2.17 shows the data flow path using the PXI data acquisition system.

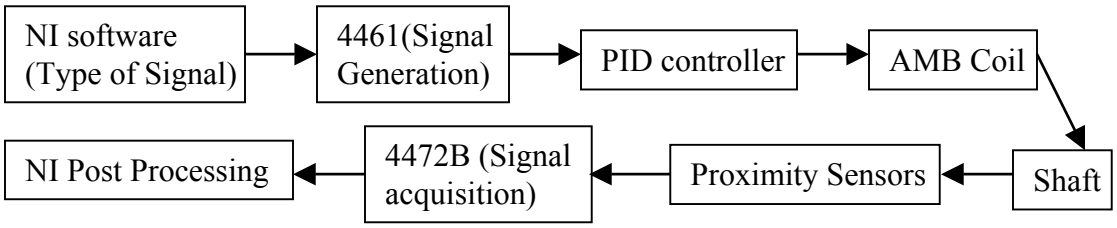

Figure 2.17. Data flow thru test rig.

One problem to overcome using the PXI controller was proper triggering of the two cards. The current setup begins with the 4461 card reading the tachometer signal and waiting for a threshold value to be met from a tachometer pulse. When a pulse is found by the 4461 card, a digital trigger is sent to the output channel of the same card as well as the 4472B card to begin. The one limiting factor from this setup is the lack of a retriggerable counter that could restart triggering on a tachometer pulse for averaged data. In the future, another card with a counter could be inserted into the PXI chassis to overcome this problem.

2.4 Vibration Analysis

Vibration is the branch of engineering that deals with repetitive motion of mechanical systems (Inman 2001). Using vibration analysis allows for the prediction of system responses such as natural frequencies. The simplest Single Degree of Freedom (SDOF) system can be modeled using Equation 2.1 where ω_n is the undamped natural frequency, m is the mass of the system, and k is the stiffness.

$$\omega_n = \sqrt{\frac{k}{m}} \tag{2.1}$$

Equation 2.1 leaves out one important variable which is damping. Damping is usually represented by the variable c, but generally is represented by a damping ratio ζ.

$$\zeta = \frac{c}{2\sqrt{km}} \tag{2.2}$$

Damping changes the natural frequency to a damped natural frequency ω_d as shown in Equation 2.3. A damped natural frequency will always be lower than the natural frequency. In general, damping is a good parameter to have because it removes energy from the system in question.

$$\omega_d = \omega_n \sqrt{1-\zeta^2} \tag{2.3}$$

In reality, most real systems have multiple degrees of freedom and can be represented by an NxN matrix of mass, stiffness, and damping values shown in Equation 2.4. This equation makes a large assumption that C is a symmetric matrix.

$$M\ddot{x} + C\dot{x} + Kx = 0 \tag{2.4}$$

A rotating machine complicates analysis due to rotation. Many different effects can influence a shafts response such as gyroscopics, shaft bow, and unbalance. Some of the most influential characteristics are the stiffness and damping of the bearings as well as the type of bearing used. Ehrich (1999) provides a large table of possible rotating machinery faults in

"Handbook of Rotordynamics." A few common faults and associated vibration responses are shown in Table 2.3.

Table 2.3. Rotating machine malfunctions.

Fault	Frequency*	Spectrum, time domain, orbit shape	Correction
Mass unbalance	1X	Distinct 1X with much lower values of 2X and 3X, etc.	Field or shop balancing
Misalignment	1X,2X, etc.	Distinct 1X with equal or higher values of 2X and 3X, etc.	Perform hot and/or cold alignment
Shaft bow	1X	Dropout of vibration around critical speed in Bode plot	Heating or peening to straighten rotor
Bearing wear	1X, subharmonics, orders	High 1X, high ½X, sometimes 1 ½ or orders; can not be balanced	Replace bearing
Asymmetric rotor	2X	½ critical speed appears on Bode plot	Eliminate asymmetry
Cracked rotor	1X, 2X	High 1X, ½ critical speeds may show up on coast down	Remove rotor
Rubs	¼ X, 1/3 X, ½ X, or orders	External loops in orbit	Eliminate condition such as bow and mass unbalance

*1X = one times operating speed.

A natural or damped natural frequency can be altered by changing either the mass, stiffness, or damping of a system. Take for instance a cracked shaft. Instead of the cracked shaft having a uniform stiffness during rotation like a healthy shaft, a cracked shaft will have a time varying stiffness as seen in Figure 2.18 and 2.19. In Figure 2.18, the stiffness K_2 may be larger than K_1 when the crack is facing down because shaft deflection may open the crack. The stiffness K_2 may still be greater but could also equal K_1 when the crack is facing up due to the reversal in shaft deflection under gravity.

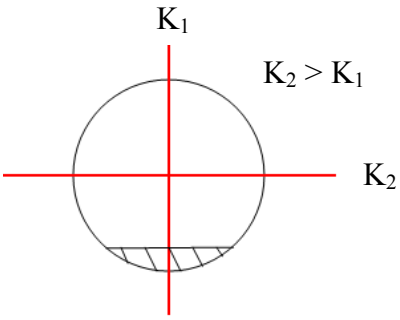

Figure 2.18. Shaft with crack facing down.

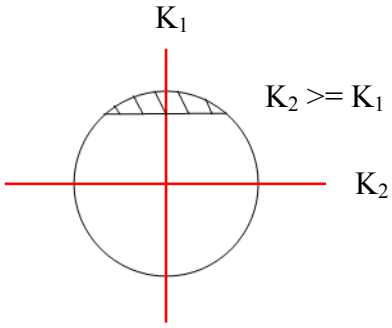

Figure 2.19. Shaft with crack facing up.

During the development phase for this project, a finite element model was made using DyRoBeS™. DyRoBeS™ was used as a tool to help ensure that a critical speed would be within the maximum motor speed. A version of that model was made from the actual final specifications of the test rig, but there were still some variables that were not known exactly such as the exact stiffness of the ball bearings and true PID parameters used for the AMB. Instead, the model was varied for three cases. The first case assumed no stiffness and damping from the AMB. However, the second case added a constant 2500 lb/in for stiffness and a very low value for damping, and the third case kept the amount of damping the same with an increase in stiffness to 5000 lb/in. A summary of the first four frequencies for this model can be seen in Table 2.4 with assumed ball bearing stiffness of 150,000 lb/in. The corresponding mode shapes for the same four frequencies with an AMB stiffness of 2500 lb/in are shown in Figures 2.20, 2.21, 2.22, and 2.22.

Table 2.4. DyRoBeS™ frequency data.

	AMB stiffness			
Mode Frequency (Hz)	k=0 lb/in	k=2500lb/in	k=5000 lb/in	actual measured frequency
First mode	42.3	73	91.41	56.5
Second mode	262	271	280.4	224
Third mode	682.7	682.8	682.8	512.5
Fourth mode	1116.9	1118.5	1120.1	794

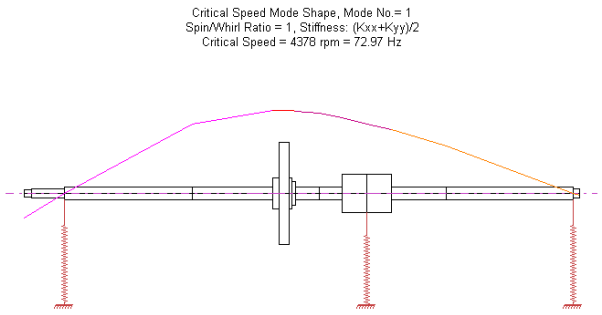

Figure 2.20. First mode calculated by DyRoBes for AMB stiffness of 2500 lb/in.

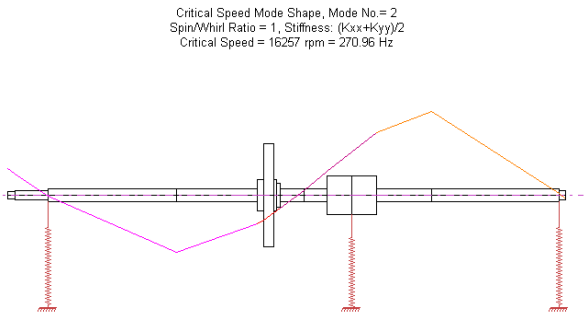

Figure 2.21. Second mode calculated by DyRoBes for AMB stiffness of 2500 lb/in.

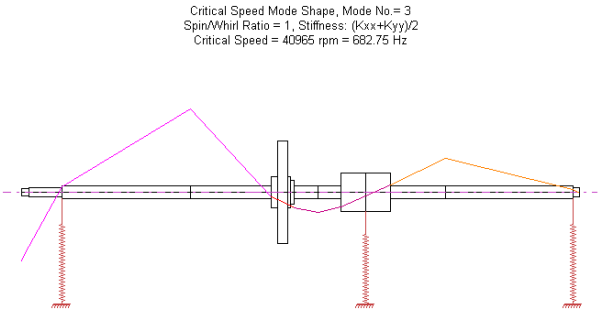

Figure 2.22 Third mode calculated by DyRoBes for AMB stiffness of 2500 lb/in.

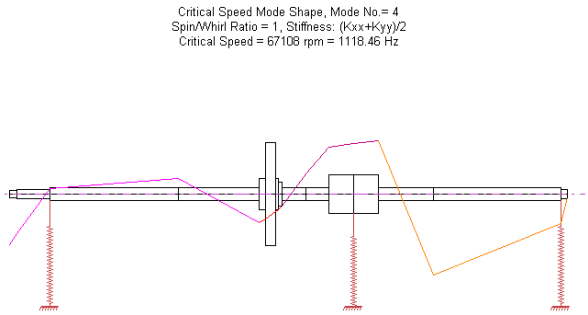

Figure 2.23. Fourth mode calculated by DyRoBes for AMB stiffness of 2500 lb/in.

This research aims to focus on the response of cracked shaft by mimicking this fault with a notch as mentioned previously. Cracked shafts are faults that can be difficult to detect. According to Enrich (1999), cracked shafts exhibit higher 1X components and possible super harmonics on coast down. These types of responses will be monitored during research, and other types of methods will be tested such as modal analysis. Modal analysis was chosen because the data will be represented in the frequency domain, and many faults in rotating machinery are diagnosed and documented in the frequency domain. Most frequency data for rotating machinery was taken using a FFT, but this research is focused on using a frequency response function, which is the next topic discussed.

2.5 Modal analysis

Experimental modal analysis is a method for finding the natural frequencies and mode shapes of a particular system by applying an input force to the system and monitoring the vibrational response as shown in Figure 2.24. The relationship of the output X(ω) over the input F(ω) gives the transfer function H(ω) also known as the Frequency Response Function (FRF), which describes how the system will respond at a given frequency ω. This relationship for frequency indicates that the system can and most likely will vary per frequency value or spectral line.

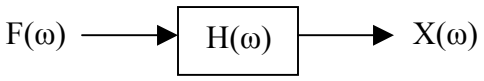

Figure 2.24. Transfer function relationship of a generic system.

Analytically, modal analysis is governed by Equation 2.5 where the transfer function H(ω) is a function of all the system parameters such as modal mass M_n and damping, but also included is the location *k* of the forcing function as well as the location *i* of the measured response. The variables *i* and *k* not only indicate the spatial location of forcing and measurement, but also the mode shape vector ϕ at the combination of these spatial locations for a given natural frequency *n*.

$$H(\omega)_{ik} = \frac{X(\omega)_i}{F(\omega)_k} = \sum_{n=1}^{N} \frac{({}_n\phi_i)({}_n\phi_k)}{(-\omega^2 + \omega_n^2 + j2\zeta\omega\omega_n)(M_n)} \tag{2.5}$$

As mentioned previously, experimental modal analysis is a method of finding natural frequencies and mode shapes of a system. Specifically, the natural frequencies are found by observing the many output parameters of modal analysis such as magnitude and phase. Magnitude plots are generally one of the more popular plots of a FRF and contain the magnitude response of the system as a function of frequency. In a system where the natural frequencies are well spread apart, known as a decoupled system, there will be clear peaks that indicate natural frequencies. If one compares the frequency value at a peak in a magnitude plot to that of the phase plot, there is usually a change of 90 degrees phase near the same frequency value as the peak in the magnitude plot. When measuring position or acceleration, the imaginary component includes the mode shape vector at a particular natural frequency. With sufficient points measured in a system, a mode shape can be constructed for a particular natural frequency. One

other modal parameter not yet discussed, but equally important, is coherence. Coherence is a measure of how much the input correlates to the output scaled from zero to one with zero indicating no correlation and one indicating perfect correlation. Coherence validates a measurement on a per frequency basis to insure that the transfer function is acceptable and not a measurement of noise or poor system response. The key to coherence is spectral averaging. Spectral averaging helps to average noise in a measurement from either the input output or both. Most every test for this research used a total of 10 spectral averages. A plot of the magnitude, phase, imaginary, and coherence due to a W-axis chirp generated by the AMB and measured at the 45° inboard proximity probe with a healthy shaft is shown in Figure 2.25. The magnitude plots in this paper have units of mils/volt because the shaft response measured by proximity probes is converted to mils, but the excitation signal generated is in volts.

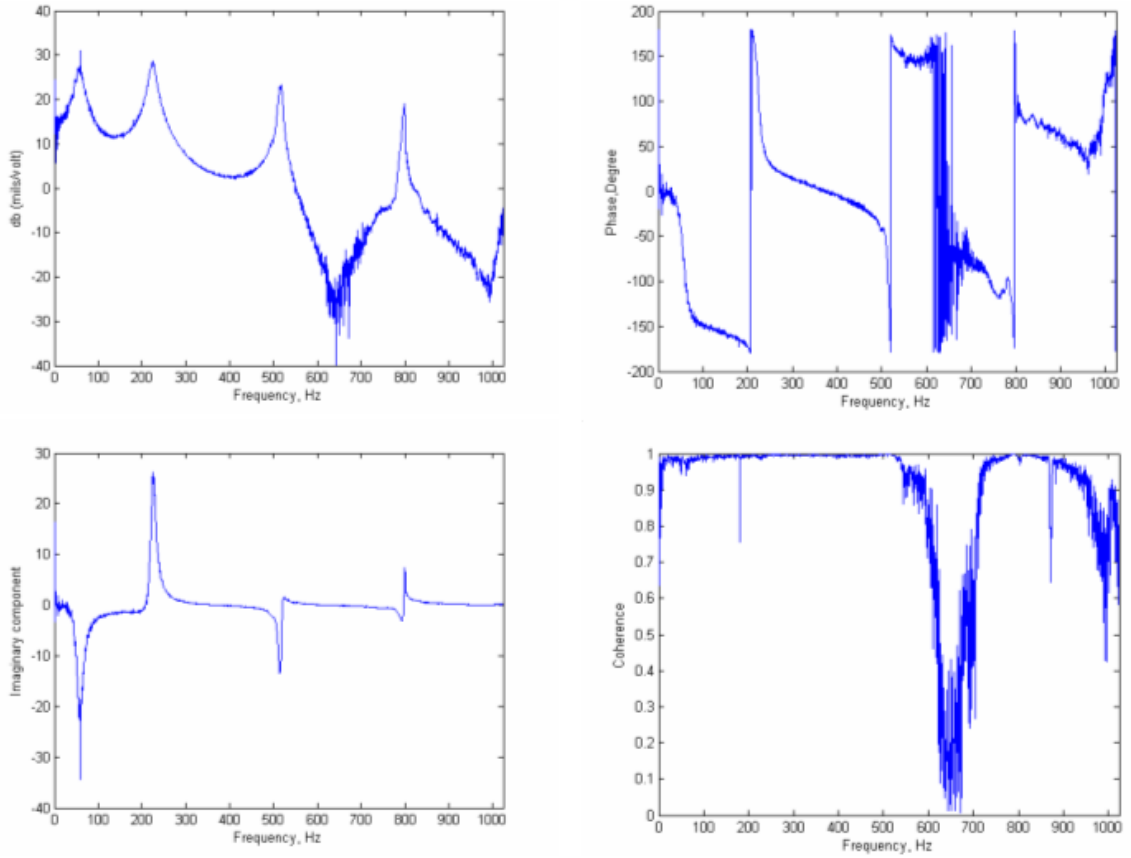

Figure 2.25. Plot of magnitude, phase, imaginary, and coherence of healthy shaft measured by the 45° inboard probe due to a W-axis chirp.

Input forces for modal analysis take on many different types of forms according to the system and the desired outputs. Some of the input forces include hammer impacts, noise signals like Gaussian signals, and ramping sinusoids called chirps. This research focused on using a

chirp and Gaussian input generated by the AMB to excite the shaft, but most results presented in this paper are due to a chirp.

Response of a system can be measured in many different ways, but one of the most popular for structural dynamics is the accelerometer. Some accelerometers have good frequency response at frequencies as low as 1 or 2 hz and up to 10khz (Reliability Direct). Accelerometers are used in rotating machinery, but usually on the machine casing. The most common form of measurement for rotating machines is a non-contact proximity probe. These types of probes have a slightly different response compared to accelerometers with good low frequency response and a flat response out to 1000 hz.

Chapter Three

Shaft Rub Results

3.1 Introduction to shaft rub

The first rotor fault investigated was shaft rub. Shaft rub occurs when a machine component moves into the orbital path of the shaft, or the shaft orbit grows sufficiently large to interfere with the surrounding components. This research will focus on the first by using a brass screw that is placed into contact with the rotor. Rub testing began with the static setup and the AMB positioned at midspan. During testing, the brass screw was positioned either 0°, 45°, 90°, 135°, or 180° in the proximity probe mount located at either the inboard or outboard locations shown in Figure 3.1. Both a chirp and Gaussian forcing function were used along both the V and W axis in the AMB to excite the shaft. One additional measure taken to attempt equal rub for each testing case was to apply the same amount of force that would yield an equal change in AMB currents. This was done manually by observing the top currents of the V and W axes of the AMB. The FRF bandwidth chosen was 1024 Hz because that frequency range included four modes of the shaft. A bandwidth of 1024 Hz and 2048 samples gives a frequency resolution of 0.5 Hz.

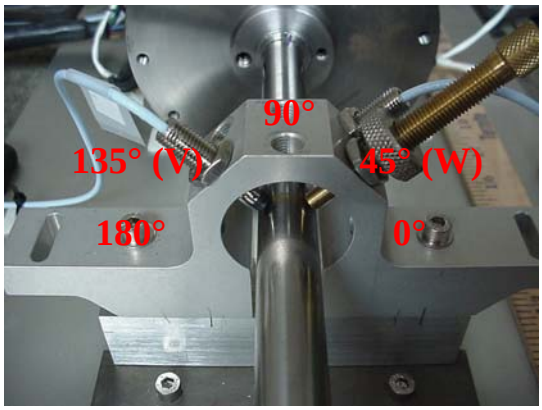

Figure 3.1. Static radial rub locations.

3.2 Static Shaft Rub Results

Results shown in this section are for a shaft at zero rpm and may be used as a pre-startup check for machinery. A shaft rub was easy enough to simulate for this research, but the amount of rub applied to a shaft can change the response of the shaft drastically. For instance, if there is a light rub applied to the shaft, the shaft may vibrate loosely touching and leaving at the point of the rub. However, if the rub is very heavy then the shaft may still vibrate easily but with the rub point acting like a hard stop or node. The first results seen in Figures 3.2 and 3.3 are from a light and hard inboard rub at 45° using a chirp on the W AMB axis measured at the inboard 45° probe and the 45° probe on the AMB. This test setup was again tested with an AMB gaussian forcing input and can be seen in Figures 3.4 and 3.5. As a proof of concept, the test was run once more with a W-axis AMB chirp and the rub location moved to the inboard 180° position shown in Figure 3.6.

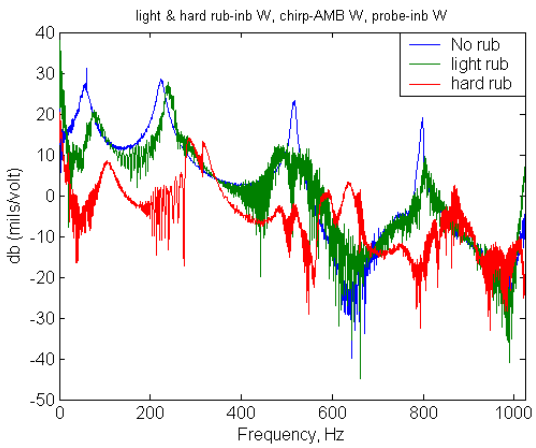

Figure 3.2. Magnitude response at the inboard 45° probe due to an inboard 45° light and hard rub at 0 rpm with W-axis chirp excitation.

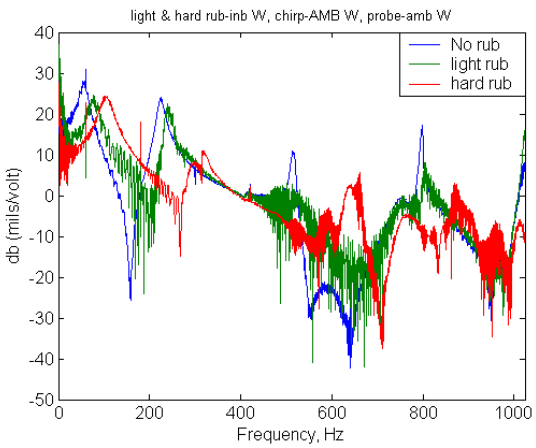

Figure 3.3. Magnitude response at the AMB 45° probe due to an inboard 45° light and hard rub at 0 rpm with W-axis chirp excitation.

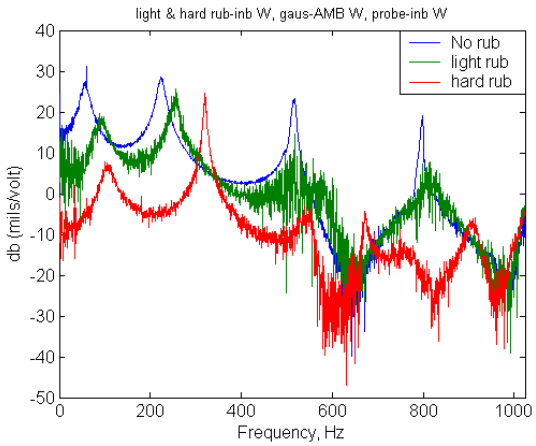

Figure 3.4. Magnitude response at the inboard 45° probe due to an inboard 45° light and hard rub at 0 rpm with W-axis gaussian excitation.

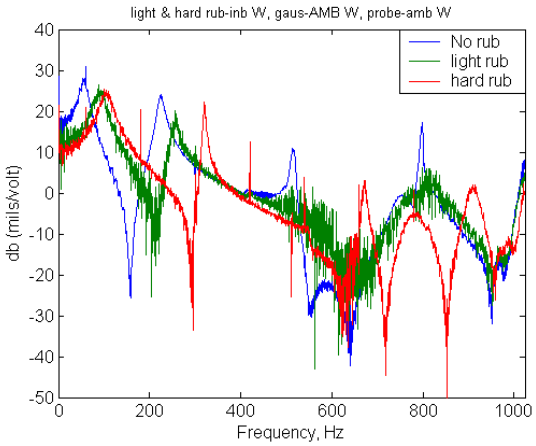

Figure 3.5. Magnitude response at the AMB 45° probe due to an inboard 45° light and hard rub at 0 rpm with W-axis gaussian excitation

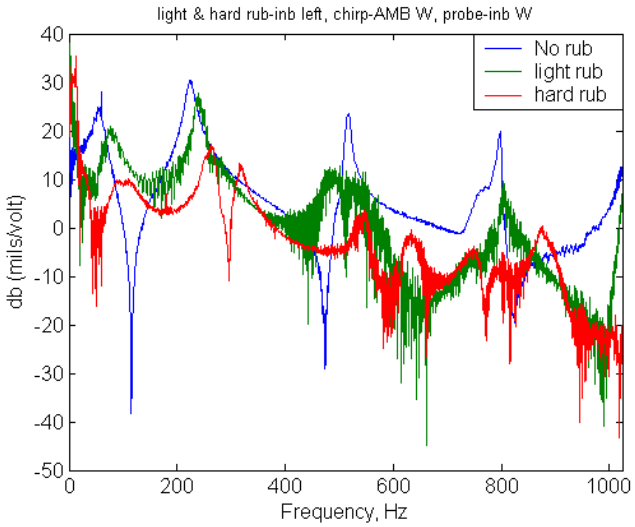

Figure 3.6. Magnitude response at the inboard 45° probe due to an inboard 180° light and hard rub at 0 rpm with W-axis chirp excitation.

It appears from the previous plots that a light rub tends to make the magnitude plots have a certain amount of noise, which might indicate the shaft bouncing against the brass screw, but one other effect to notice is that the hard rub tends to clean up the noise in the magnitude. This is also found when comparing the coherence for a no-rub, light rub, and heavy rub on the 45° axis for a W-axis chirp measured at the inboard and AMB 45° probes as shown in Figures 3.7 and 3.8. The main trend to focus on is the increasing frequency in the modes as the rub pressure increases, which is evident by all probes. There is also a decrease in magnitude at the rub location that is less evident at the probes further away from the rub.

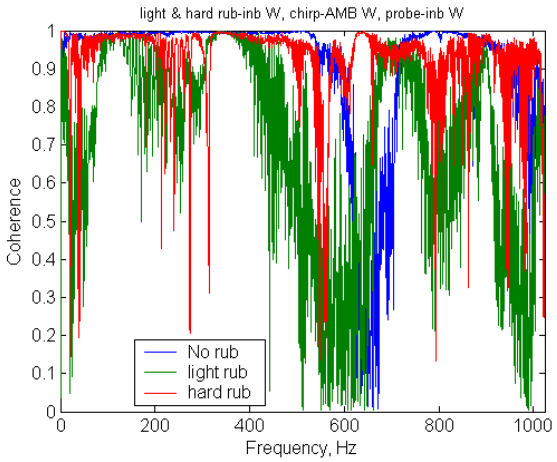

Figure 3.7. Coherence at the inboard 45° probe due to an inboard 45° light and hard rub at 0 rpm with W-axis chirp excitation.

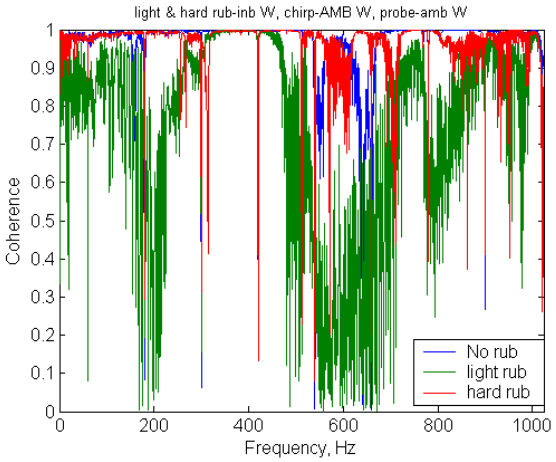

Figure 3.8. Coherence at the AMB 45° probe due to an inboard 45° light and hard rub at 0 rpm with W-axis chirp excitation.

It is difficult to distinguish from test to test how much rub pressure was applied especially when moving the brass screw to different radial positions. In an effort to overcome this problem, the AMB current was then observed and rub pressure was applied with equal current change from test case to test case. The next static data includes a light rub at all five of the radial test positions and at both the inboard and outboard proximity probe mounts. The goal now is to determine if radial position and axial position can be determined by taking an FRF of the shaft.

To find axial position of a rub, focus on the first mode magnitude response. Take for instance a rub at the inboard 45° probe location. The difference in first mode magnitude between a healthy shaft and a rubbed shaft at the inboard probe will be more than the change in magnitude seen at the AMB and outboard probes. Total difference of the magnitude varies depending on which radial position is chosen while using a W axis AMB chirp. An example of the amplitude change on the first mode can be seen in Figures 3.9, 3.10, and 3.11 for a 45° inboard and outboard rub measured at the inboard, AMB, and outboard 45° probe with a W-axis AMB chirp.

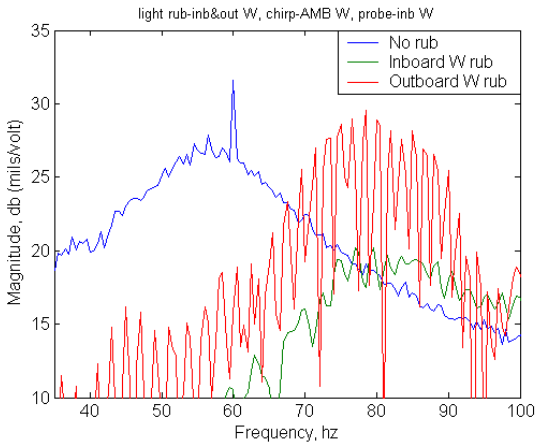

Figure 3.9. Magnitude response at the inboard 45° probe due to an inboard and outboard 45° light rub at 0 rpm with W-axis chirp excitation.

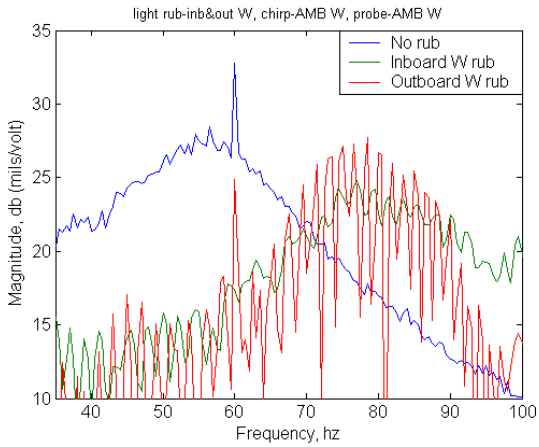

Figure 3.10. Magnitude response at the AMB 45° probe due to an inboard and outboard 45° light rub at 0 rpm with W-axis chirp excitation.

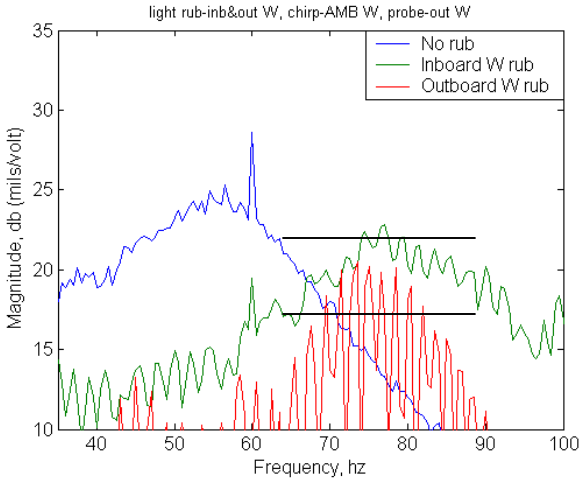

Figure 3.11. Magnitude response at the outboard 45° probe due to an inboard and outboard 45° light rub at 0 rpm with W-axis chirp excitation.

A summary of all five radial rub locations at both the inboard and outboard locations are shown in Table 3.1. If bouncing behavior was seen in the magnitude response, then an average magnitude was chosen as seen in Figure 3.11 by the black lines. The data in Table 3.1 from all five radial positions does consistently indicate approximate axial location along the shaft when comparing the change in magnitude at each probe compared to where the rub is simulated. As an example, the inboard 45° probe shows the largest change in magnitude when the rub is in fact inboard, and the AMB probe shows less magnitude change with the outboard probe showing even less magnitude change. This trend is the same for all the inboard rub tests and the reverse is

true for all the outboard tests. There is one data point highlighted, which shows almost matching magnitude changes for an inboard and outboard rub. However, if the other probe magnitudes are compared, the trend still exists with lowering magnitudes away from the rub location.

Table 3.1. Magnitude difference between a healthy shaft and a light inboard and outboard rub.

Magnitude Difference in dB between Healthy and Light Inboard Rub

Rub angle	*0°*	*45°*	*90°*	*135°*	*180°*
Inboard 45° probe	10.3	9	10.6	6.8	12.8
AMB 45° probe	8.2	4.4	7.4	5.7	9.4
Outboard 45° probe	7.8	3.1	5.8	5.2	8.1
Correct rub location	YES	YES	YES	YES	YES

Magnitude Difference in dB between Healthy and Light Outboard Rub

Rub angle	*0°*	*45°*	*90°*	*135°*	*180°*
Inboard 45° probe	5.6	3.8	3.6	6	4.8
AMB 45° probe	9.4	6.4	6.1	9.3	7.9
Outboard 45° probe	18.3	8.5	8.3	14	12.8
Correct rub location	YES	YES	YES	YES	YES

To determine the radial position of a rub was more difficult than expected. Observing the changes in magnitude and frequency are not always clear and can vary. Instead, focus was made on the changes in mode shape as a rub was moved along each radial position. This process begins with the healthy shaft and the natural frequency of each of the modes in the FRF. These frequency values correspond to an imaginary component that when plotted can produce a mode shape. Take for example the first mode in the healthy system at 56.5 Hz. If the imaginary value at 56.5 Hz is taken from the inboard, AMB, and outboard 45° probes; respectfully, then a mode shape can be constructed as shown in Figure 3.12.

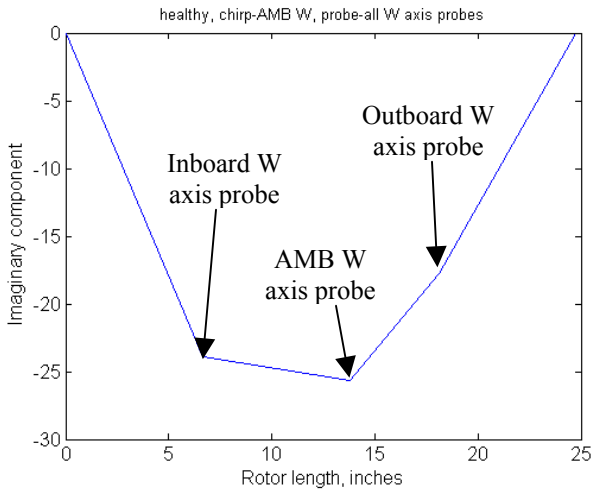

Figure 3.12. Healthy shaft modeshape along W axis at 0 rpm due to a W-axis AMB chirp.

If all the rub cases are plotted against the healthy case, some information can be found that may give insight to the radial location of the rub. The first case to consider is shown in Figures 3.13 and 3.14 for the 45° and 135° axis at 1st mode with a W axis AMB chirp. In Figure 3.13, the rub on the 45° axis has a large effect when compared to the healthy mode shape. As the rub rotates away from the axis of excitation, the mode shapes grow with the rub on the 135° axis acting the most similar to a healthy shaft. It makes sense that the 135° axis would have the most similar mode shape compared to the healthy due to the location of rub 90° off the axis of forcing. If the 135° axis mode shape of Figure 3.14 is considered, then the above statement is false, and the mode shape does not increase as the rub rotates away from the axis of excitation. The same trend as Figure 3.13 exists for the second mode shown in 3.15, but again the off axis 135° mode shape in Figure 3.16 does not increase as the rub rotates away from the axis of excitation. These mode shape trends may help locate the radial position of a rub before a machine start-up.

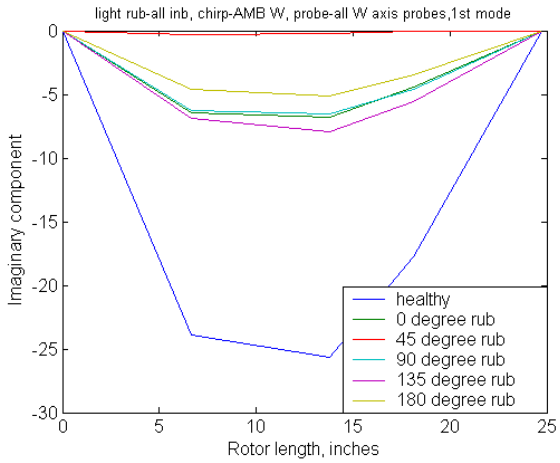

Figure 3.13. First mode shape of 45° axis for 0°,45°,90°,135°,180° inboard radial rubs.

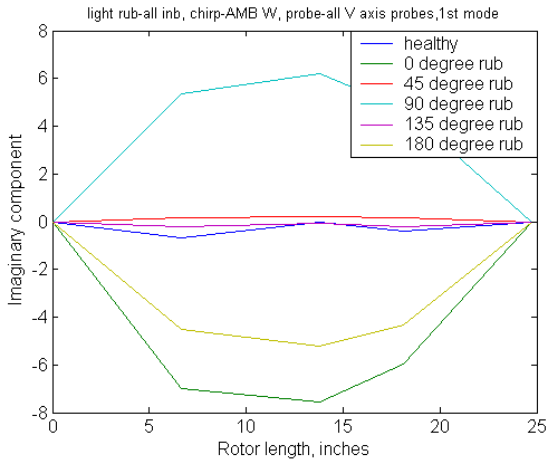

Figure 3.14. First mode shape of 135° axis for 0°,45°,90°,135°,180° inboard radial rubs.

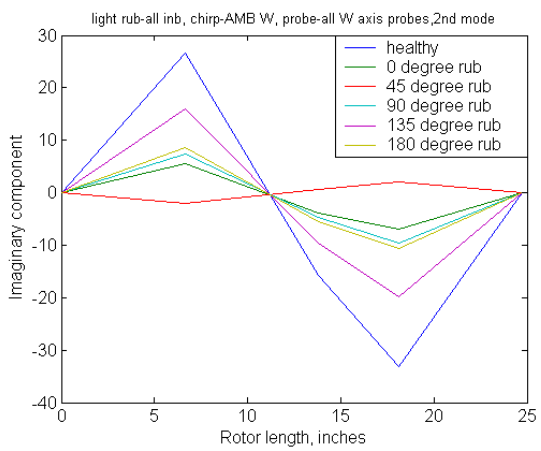

Figure 3.15. Second mode shape of 45° axis for 0°,45°,90°,135°,180° inboard radial rubs.

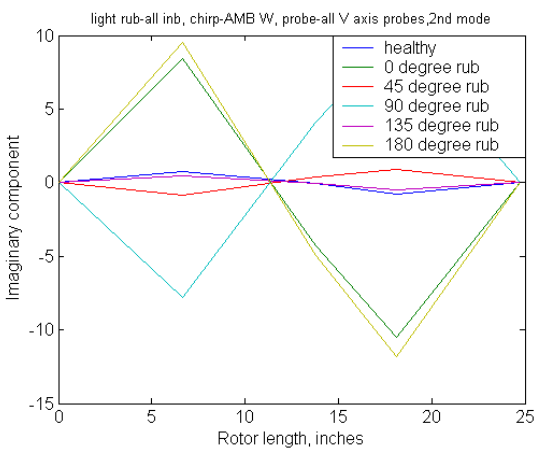

Figure 3.16. Second mode shape of 135° axis for 0°,45°,90°,135°,180° inboard radial rubs.

3.3 Dynamic Shaft Rub Results

Dynamic rub testing was conducted with a rub at two radial positions. The first radial location was on the 45° axis in the proximity probe holder, while the other radial rub was applied on the 180° axis. These two axes can be seen in Figure 3.1 previously shown. Both radial positions were applied at the same inboard and outboard locations shown in Figure 2.10 for three dynamic test speeds of 600, 2400, and 5100 rpm. The first critical speed of the shaft is at 3400 rpm; therefore, speeds were specifically chosen to include a slow roll, subcritical, and supercritical test speed of the shaft.

Most rotating machines are monitored by some type of signal analyzer such as Bently's® ADRE® 208. ADRE® has the ability to take FFTs at running speed as well as during run up and run down. A FFT of a healthy shaft running at 600 rpm can be seen in Figures 3.17 and 3.18 for the inboard 45° and 135° axis probes. The same probe response can be seen in Figures 3.19 and 3.20 with a rub at the inboard 45° axis position. Note the many synchronous harmonics along the W axis probe and the slightly lower harmonics of the 135° axis probe.

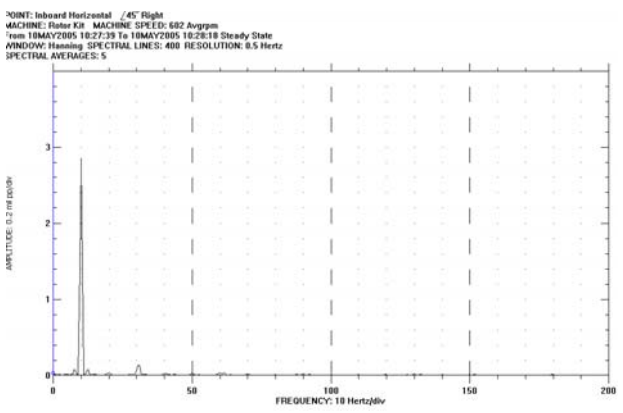

Figure 3.17. FFT of healthy shaft at inboard 45° axis running at 600rpm.

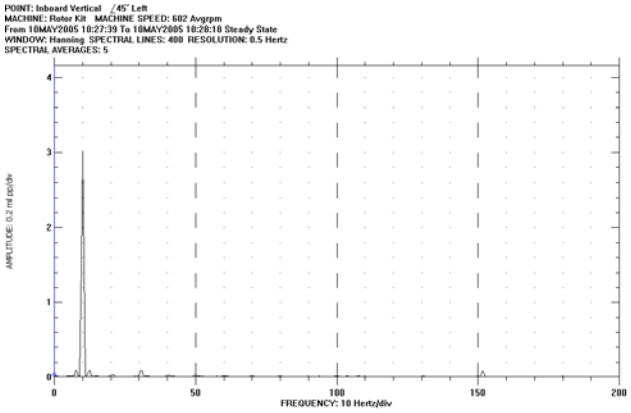

Figure 3.18. FFT of healthy shaft at inboard 135° axis running at 600 rpm.

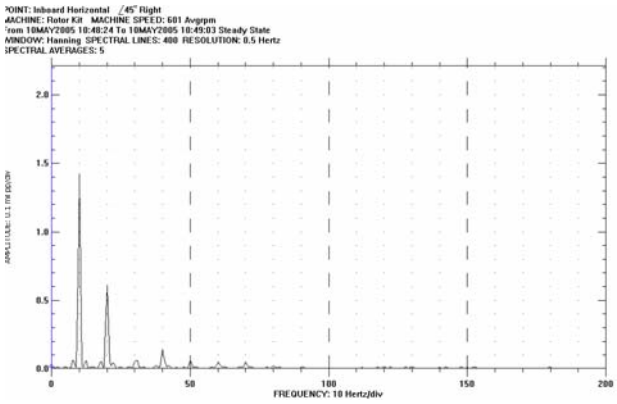

Figure 3.19. FFT at inboard 45° axis running with a 45° axis rub at 600rpm.

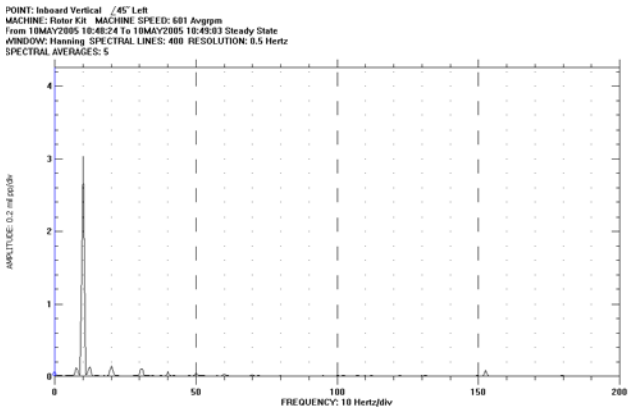

Figure 3.20. FFT at inboard 135° axis running with a 45° axis rub at 600 rpm.

The first dynamic results using an FRF for the 600 rpm case are next. By using an FRF instead of a FFT, multiple shaft modes can be monitored at a single running speed where as an FFT may only show certain harmonics of that running speed. Be aware that these dynamic FRFs are not as clean as static FRFs. There is line noise and line harmonics in the data from the AMB controller.

A light and heavy rub were again considered at both the inboard and outboard locations along the 45° axis with a W-axis chirp. These results vary slightly from that of the static case as shown in Figure 3.21. Zoomed sections of the first and second mode from Figure 3.21 can be seen in Figures 3.22 and 3.23. Instead of a nice clean reduction in the magnitudes and a well defined increase in the frequencies, the reductions in magnitudes are less, but the largest change appears to be a splitting of the main natural frequencies. This splitting of frequencies is evident

for the first three modes. A comparison of the 135° rub with a W-axis chirp can be seen in Figure 3.24 with zoomed plots of the first and second mode shown in Figures 3.25 and 3.26. This plot does vary at the first and third modes with the largest change still at the second mode. It may also be beneficial to observe coherence as shown in Figure 3.27 because the coherence shows decline as the rub pressure increases. Figure 3.27 is the coherence plot from a 45° inboard light and hard rub measured at the inboard 45° probe. A decline in FRF coherence may indicate a rub while running at a slow roll speed.

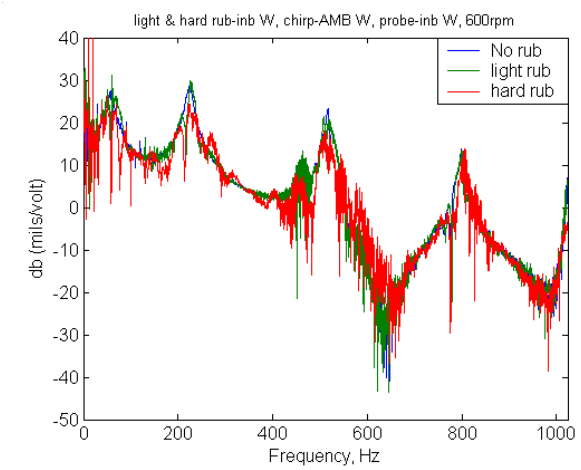

Figure 3.21. Inboard light and hard 45° rub at 600 rpm with W-axis chirp measured at the inboard 45° probe.

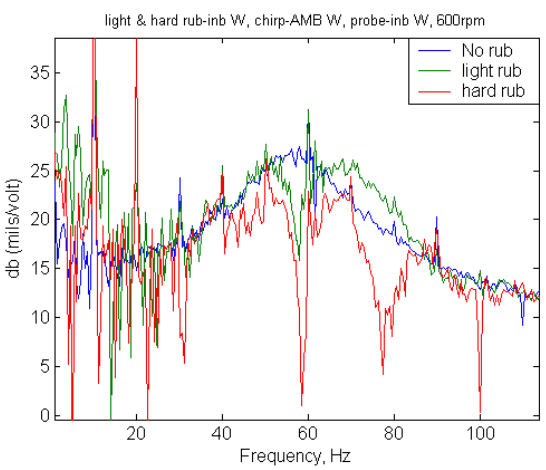

Figure 3.22. First mode for an inboard light and hard 45° rub at 600 rpm with W-axis chirp measured at the inboard 45° probe.

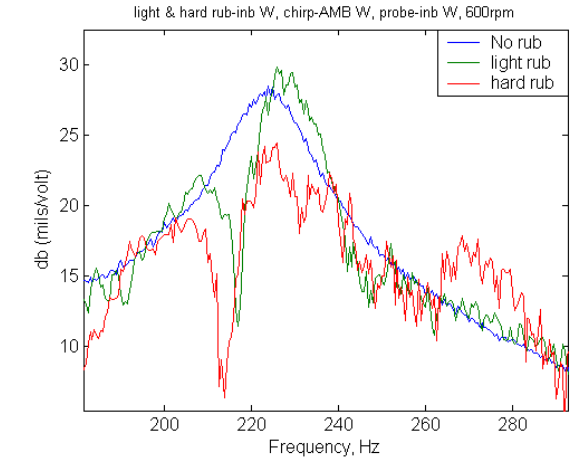

Figure 3.23. Second mode for an inboard light and hard 45° rub at 600 rpm with W-axis chirp measured at the inboard 45° probe.

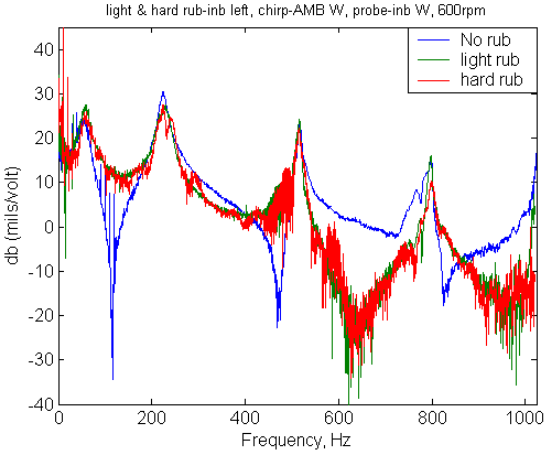

Figure 3.24. Inboard light and hard 135° rub at 600 rpm with W-axis chirp measured at inboard 45° probe.

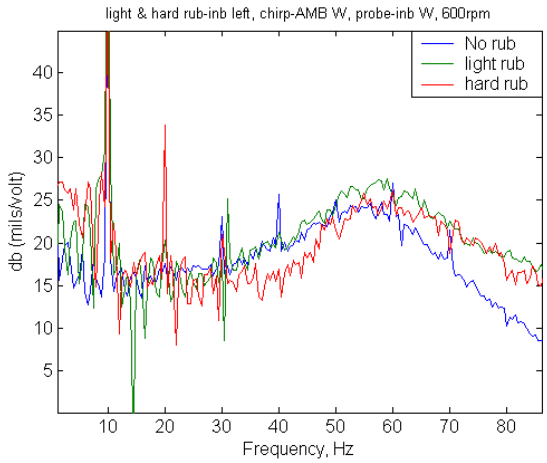

Figure 3.25. First mode for an inboard light and hard 135° rub at 600 rpm with W-axis chirp measured at the inboard 45° probe.

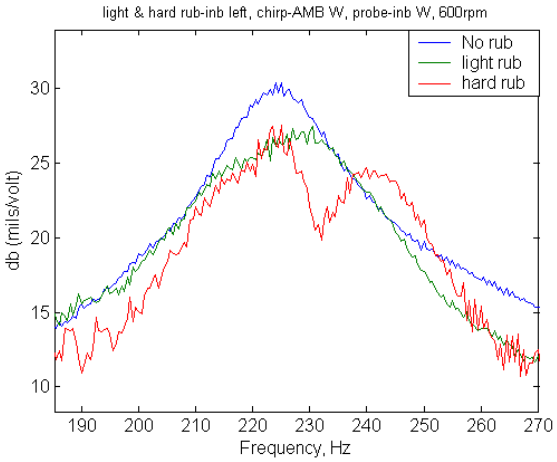

Figure 3.26. Second mode for an inboard light and hard 135° rub at 600 rpm with W-axis chirp measured at the inboard 45° probe.

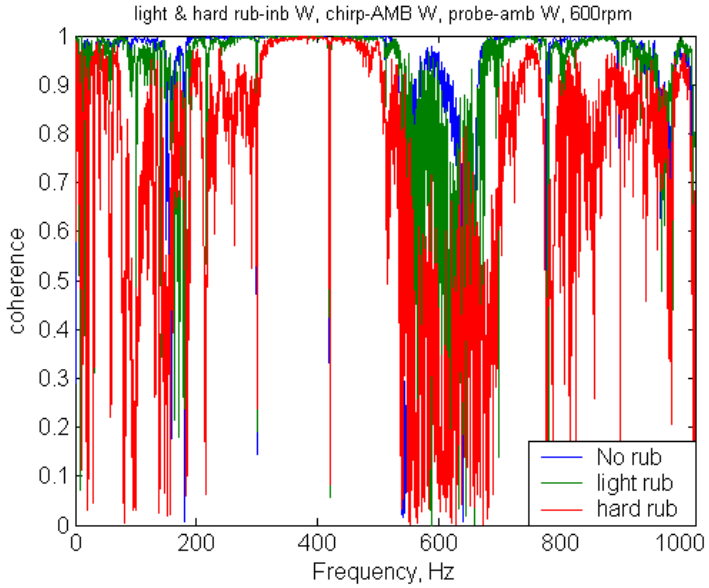

Figure 3.27. Coherence of a light and hard 45° degree rub measured at the inboard 45° probe while running at a slow roll speed of 600 rpm.

The next results are for the 2400 rpm test speed. ADRE® was used again to take a healthy and rub FFT at running speed for the inboard 45° axis probe as seen in Figures 3.28 and 3.29. There are not as many harmonics for this test case as with the 600 rpm speed.

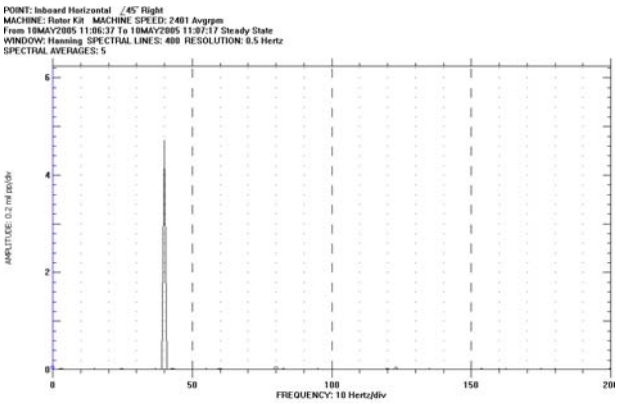

Figure 3.28. FFT of healthy shaft at inboard 45° axis running at 2400rpm.

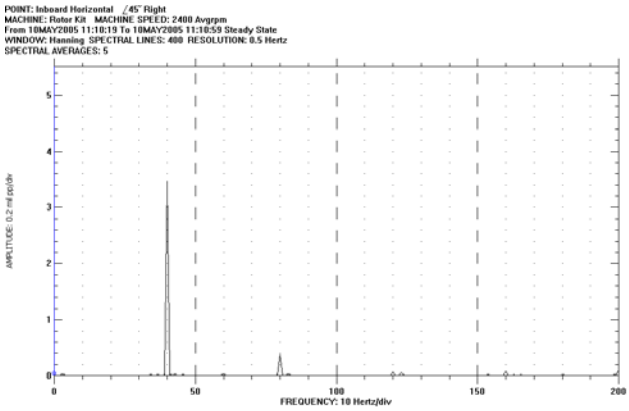

Figure 3.29. FFT at inboard 45° axis running with a 45° axis rub at 2400 rpm.

Results from the FRFs at the 2400 rpm test case do not show definite trends except for growing amounts of noisy magnitudes as the rub pressure increases. A plot of the inboard 45° probe can be seen in Figure 3.30, and a zoomed portion can be seen in Figure 3.31 showing the possible running speed harmonics. The possible running speed harmonics are marked with circles in Figure 3.31.

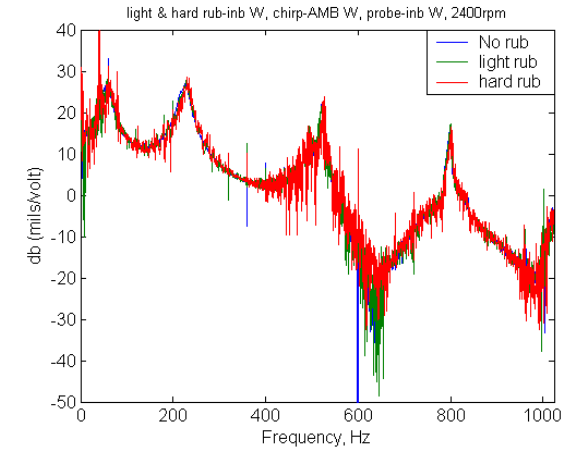

Figure 3.30. Inboard light and hard 45° rub at 2400 rpm with W-axis chirp measured at inboard 45° probe.

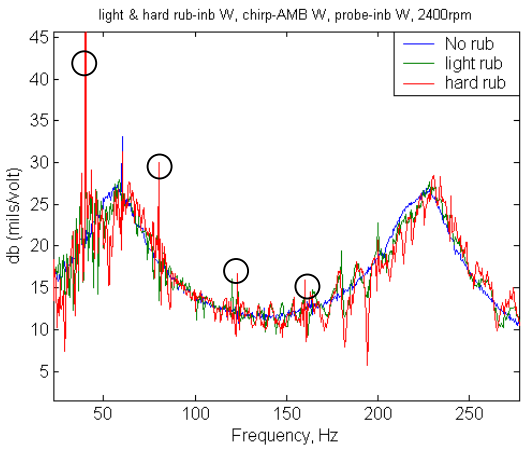

Figure 3.31. Zoomed portion of first and second mode from Figure 3.30.

The last dynamic rub results are for the 5100 rpm test speed. A healthy and rub FFT can be seen in Figure 3.32 and 3.33. This 5100 rpm speed has similar results compared to the lower running speed in that the healthy plot has one main frequency and the rub plot has a 2X component. One problem with these FFTs is the lack of bandwidth at these higher speeds.

ADRE® is limited to 400 spectral lines over any chosen frequency range. In order to keep the 0.5 hz resolution, the frequency range was kept the same.

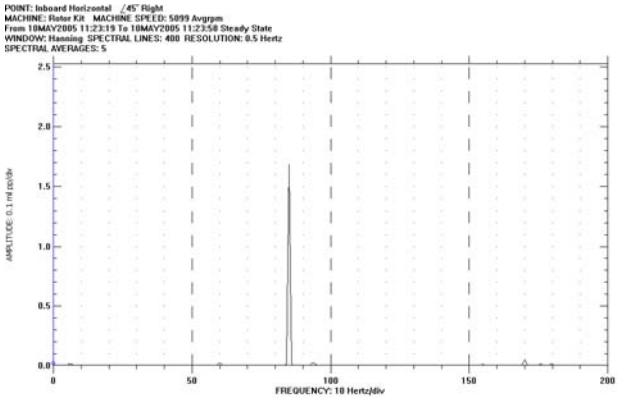

Figure 3.32. FFT of healthy shaft at inboard 45° axis running at 5100rpm.

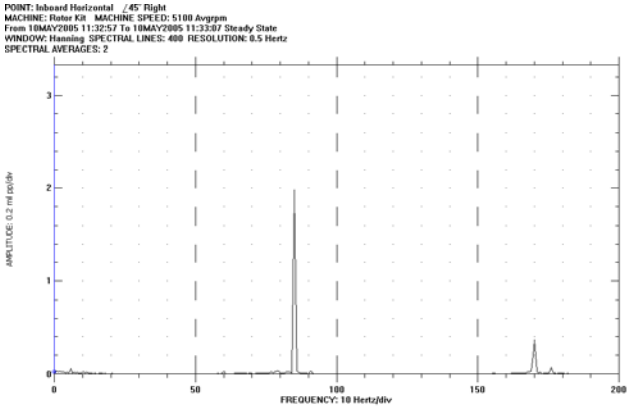

Figure 3.33. FFT at inboard 45° axis running with a 45° axis rub at 5100 rpm.

Results of the final FRF data favors earlier trends when the magnitude was reduced and the frequency shifted, but only for the hard rub. The light rub still has more noise than the healthy system as seen in Figure 3.34 for the inboard W probe. A zoomed portion of the first two modes can be seen in Figure 3.35 again with the running speed harmonics circled. One problem with dynamic rub is creating the same rub from test to test, which was a similar problem with the static testing. It is much harder to monitor current change running dynamically because the currents are sinusoids that get very noisy when a rub is initiated. One other problem with this dynamic rub testing was the brass screw. The faster the shaft is rotating, the faster the brass wears away. This leads to lessening rub as spectrum averages are taken, which may remove any major trends in the data.

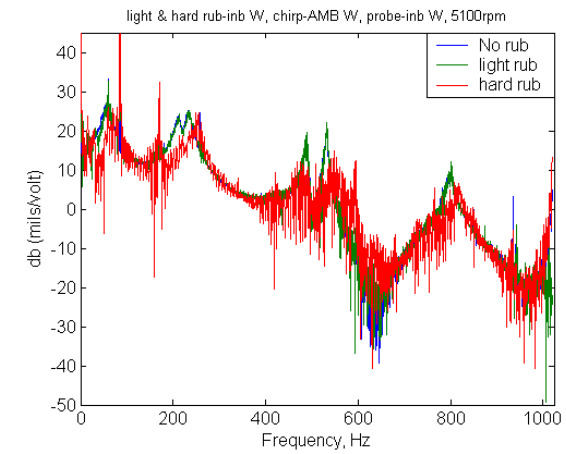

Figure 3.34. Inboard light and hard 45° rub at 5100 rpm with W-axis chirp measured at inboard 45° probe.

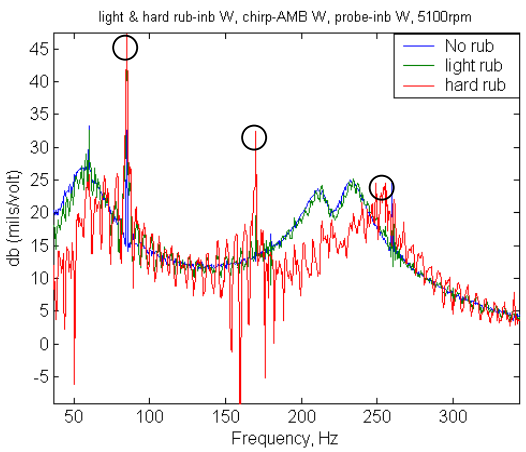

Figure 3.35. Zoomed portion of first and second mode from Figure 3.34.

3.4 Chapter Three summary

The static rub tests show that as rub pressure increases, the natural frequencies of the modes increase and the magnitudes for each frequency decrease. Results also show that a rub may be tracked along the axis of a shaft by comparing the magnitude differences from each position probe. An initial attempt to narrow down the location of the rub around the circumference of the shaft was made with marginal results by examining mode shapes.

Rub phenomena were also examined at tree dynamic test speeds of 600, 2400, and 5100 rpm which correspond to a slow roll, subcritical speed, and supercritical speed, respectfully. The dynamic results show that a light rub will cause ripples in the magnitude response of the FRF. A hard rub can cause significant ripples in the magnitude response at the slow roll speed of 600 rpm, but this ripple is less evident at the higher dynamic speeds of 2400 and 5100 rpm. There is also a loss of coherence as rub pressure increases.

Chapter four

Notched Shaft Results

4.1 Introduction to a Notched Shaft

A notched shaft was the next fault investigated in this research. The purpose of using a notch is to mimic the properties of a crack. This type of approach will not exactly copy a crack especially a breathing crack, but it will give a variable shaft stiffness. Test rig setup for the notch uses the midspan placement of the AMB shown in Figure 4.1. Static testing rotates the notch to five different angular locations while forcing with a W-axis AMB chirp. These five test positions are shown in Figure 4.2 and are designated by 0°, 45°, 90°, 135°, and 225°.

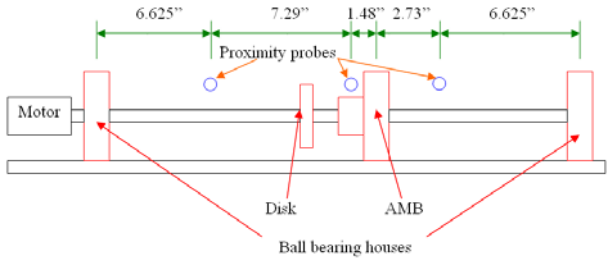

Figure 4.1. Midspan AMB diagram.

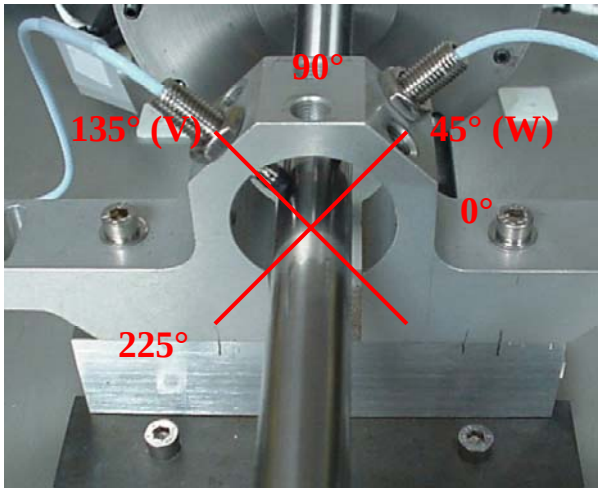

Figure 4.2. Axes of notch orientation observed from motor side.

4.2 Static Notched Shaft Results

As with the rub, notch testing will start with a zero running speed. The first data taken was for a healthy system. Next the shaft was notched to 10% diameter and the data retaken. This method was the same for the next two notch depths. Instead of showing each progression in notch, a summary plot will be given showing the 90° and 225° facing notch. These plots can be seen in Figures 4.3 and 4.4. The force for the plots shown was a W-axis AMB chirp measured at

the inboard 45° axis probe. There is little to no change in the first two modes of the shaft as shown in Figures 4.5 and 4.6 for the 90° facing notch and Figures 4.7 and 4.8 for the 225° facing notch. The largest change is seen in the third mode shown in Figures 4.9 and 4.10, which shows decreasing frequency change especially with 40% damage. However, the decreases in the third mode frequency are not always proportional with the amount of damage mostly for the 10 and 25% scenario. The 40% damaged shaft consistently shows lower frequencies up to 25 Hz for the 225° facing case. One last major result shows up in Figures 4.9 thru 4.10. For any direction that the notch faces, other than the axis of forcing and the 135° axis shown in Figure 4.11, the third mode splits. This is evident if Figures 4.9 and 4.10 are compared. Subsequently, the 135° axis facing notch has the least amount of frequency change due likely to the notch orientation contributing little change to the shaft stiffness when compared to a healthy shaft. A summary of the change in third mode for the 90° and 225° probes is shown in Table 4.1.

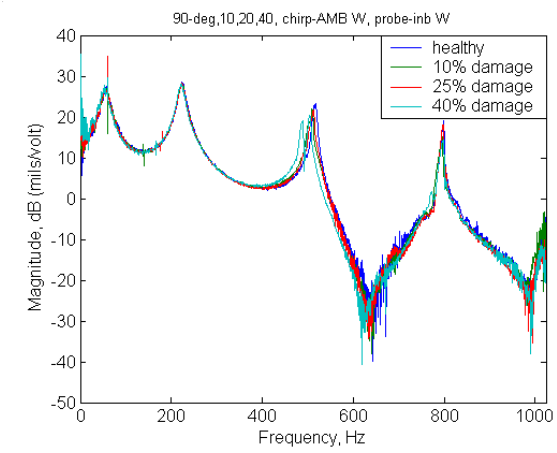

Figure 4.3. Response of a healthy, 10%, 25%, and 40% 90° facing notch measured at the 45° inboard probe with W-axis AMB chirp.

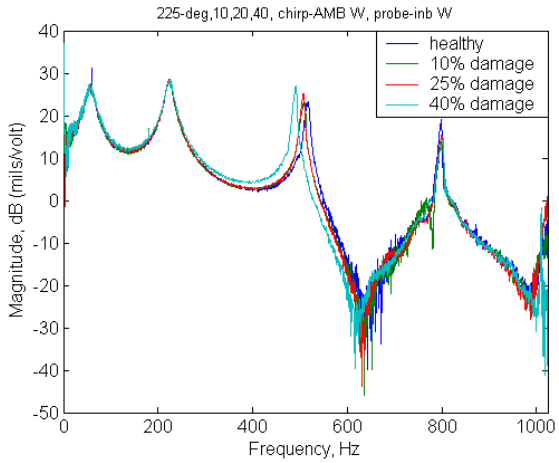

Figure 4.4. Response of a healthy, 10%, 25%, and 40% 225° facing notch measured at the 45° inboard probe with W-axis AMB chirp.

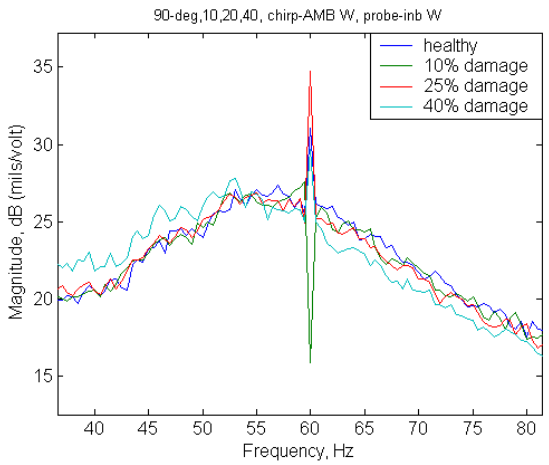

Figure 4.5. First mode of a healthy, 10%, 25%, and 40% 90° facing notch measured at the 45° inboard probe with W-axis AMB chirp.

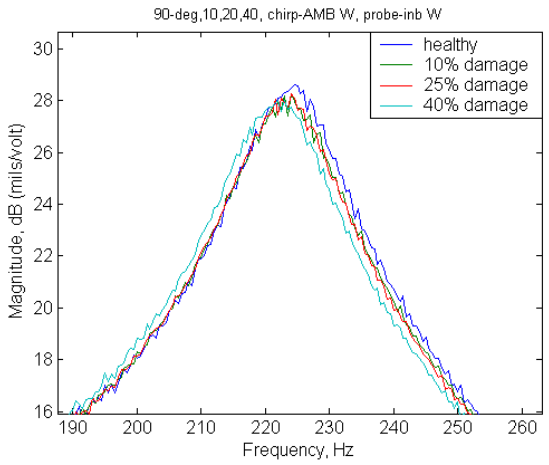

Figure 4.6. Second mode of a healthy, 10%, 25%, and 40% 90° facing notch measured at 45° inboard probe with W-axis AMB chirp.

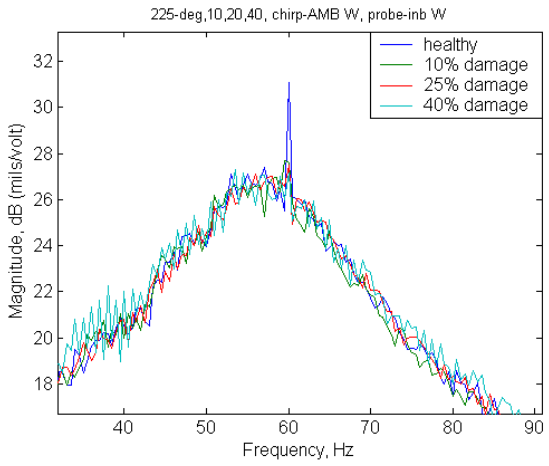

Figure 4.7. First mode of a healthy, 10%, 25%, and 40% 225° facing notch measured at the 45° inboard probe with W-axis AMB chirp.

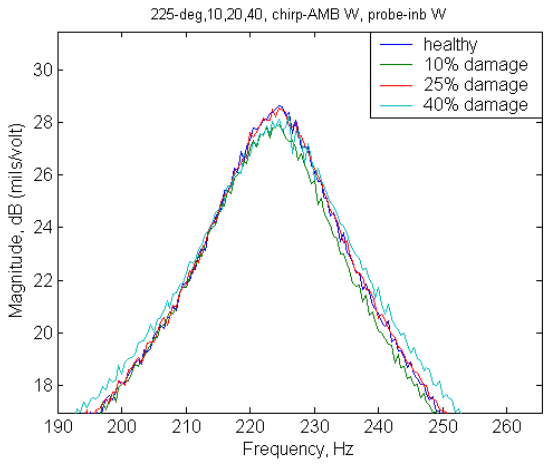

Figure 4.8. Second mode of a healthy, 10%, 25%, and 40% 225° facing notch measured at 45° inboard probe with W-axis AMB chirp.

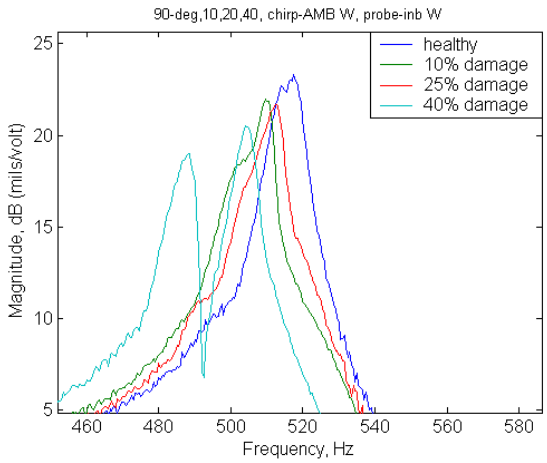

Figure 4.9. Third mode of a healthy, 10%, 25%, and 40% 90° facing notch measured at the 45° inboard probe with W-axis AMB chirp.

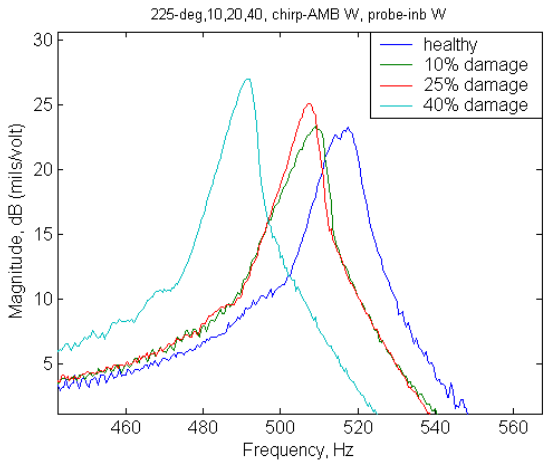

Figure 4.10. Third mode of a healthy, 10%, 25%, and 40% 225° facing notch measured at 45° inboard probe with W-axis AMB chirp.

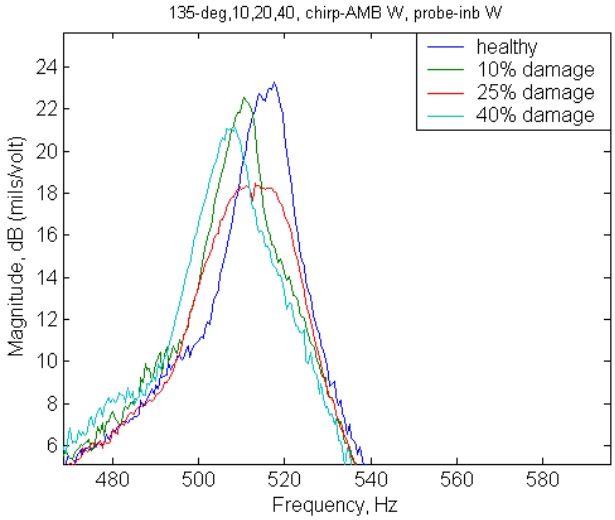

Figure 4.11. Third mode of a healthy, 10%, 25%, 40% 135° facing notch measured at the 45° inboard probe with W-axis AMB chirp.

Table 4.1. Change in third mode frequency for all notch depths for both 90° and 225° probes shown in hz and percent change.

	Shaft notch depth		
Notch Angle	*10%*	*25%*	*40%*
90°	6.5(-1.26%)	4.5(-0.87%)	12(-2.32%)
255°	7(-1.35%)	9(-1.74%)	25(-4.84%)

*Values shown in Hz and percent change.

One possible change that may have caused the discrepancy between the 10 and 25% notch facing 90° could be dynamic testing in between the static testing. For example, after the data for the 10% static case was taken, dynamic tested was then performed. This dynamic testing required some amount of balance correction due to the amount of shaft bow that occurred after the material was removed. Shaft bow originally was not an expected result from material removed, and the bow actually progressed with each increase in notch depth. So it is possible that either the bow had a significant influence on the response, or the geometry of the shaft changed even more while running thru first critical speed.

4.3 Dynamic Notched Shaft Results

Dynamic notch testing occurred at test speeds of 600, 2400, and 5100 rpm. A healthy shaft run up from ADRE® is shown in Figure 4.12, which is post balanced with no slow roll compensation. Also shown in Figure 4.13 is a cascade plot that indicates no sub or super-harmonics. Both Figure 4.12 and 4.13 are the responses from the inboard 45° probe.

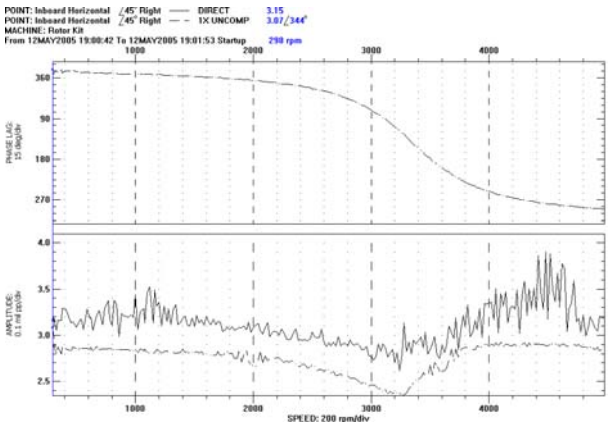

Figure 4.12. Bode plot for healthy run up on inboard 45° axis probe.

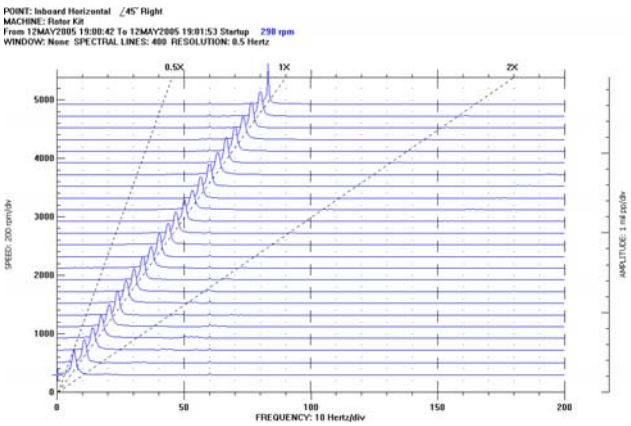

Figure 4.13. Cascade plot for run up on inboard 45° axis probe.

4.3.1 600 rpm test speed

The first dynamic test speed is 600 rpm. Data shown for this speed will include FFTs and FRFs for each notch depth. Note that FFTs taken at 600 rpm are responses for the shaft with no balance weight correction for each notch case. This will not be true with the 5100 rpm testing

which is above the first critical speed of 3400 rpm. In most cases unless otherwise noted, figures will be responses from the inboard 45° axis probe.

FFTs are seen in Figures 4.14, 4.15, 4.16, and 4.17 for a healthy, 10%, 25%, and 40% notched shaft, respectfully. As the notch becomes deeper, the 1X amplitude actually lessens by 0.6 mils peak-to-peak (p-p) for the 10% notch, 1.8 mils peak-to-peak (p-p) for the 25% notch, but grows again for a total change of 1.0 mils p-p for the 40% notch. Also apparent in these plots are harmonics of the 600 rpm running speed, which is 10 hz. These harmonics are relatively small and only increase slightly.

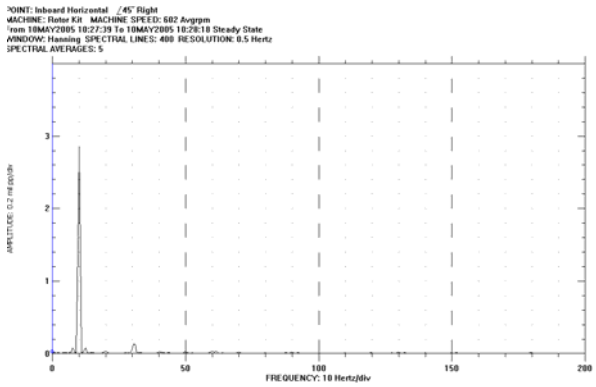

Figure 4.14. FFT of healthy shaft at inboard 45° axis running at 600rpm.

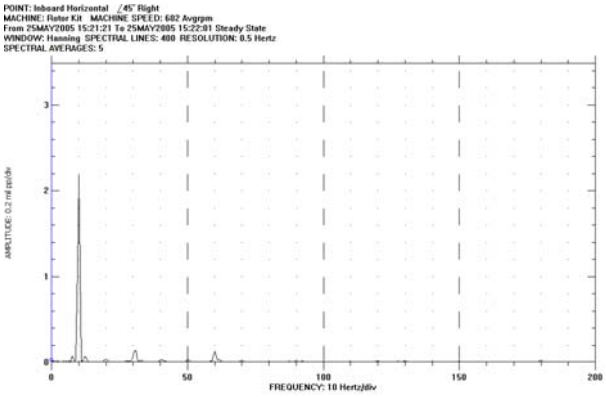

Figure 4.15 FFT of shaft with 10% notch at inboard 45° axis running at 600rpm.

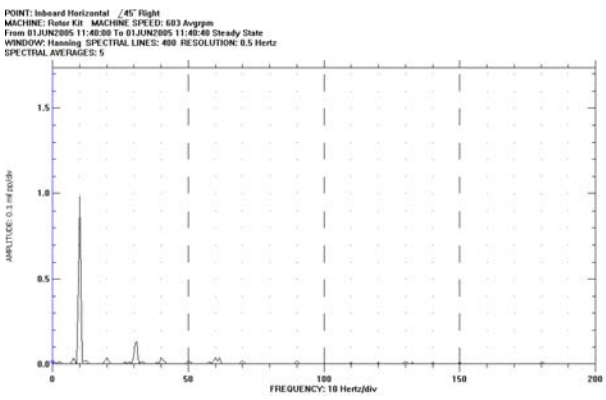

Figure 4.16. FFT of shaft with 25% notch at inboard 45° axis running at 600rpm.

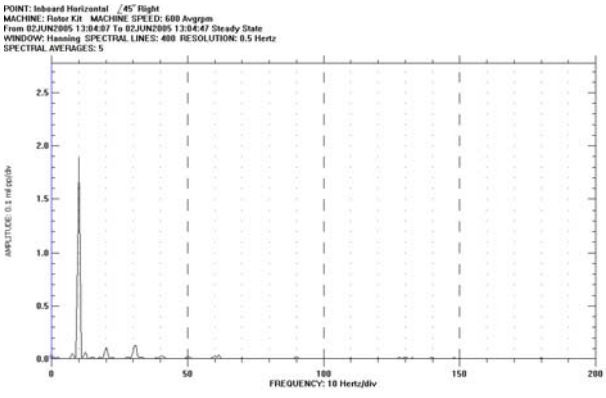

Figure 4.17. FFT of shaft with 40% notch at inboard 45° axis running at 600rpm.

Running FRFs for 600 rpm indicate very little to no change in the first or second modes as shown for Figures 4.18 and 4.19, but the third mode does show change especially for the 40% notch depth shown in Figure 4.20. The full spectrum plot can be seen in Figure 4.21. As before, the 10 and 25% notches do not show a significant change in decreasing frequency, but the 40% notch has an approximate drop in frequency of 19 Hz or a change.

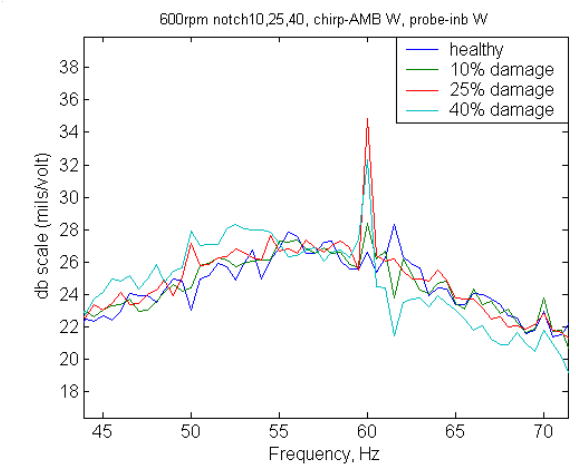

Figure 4.18. First mode of a midspan notch at 600 rpm measured at the 45° inboard probe with W-axis AMB chirp.

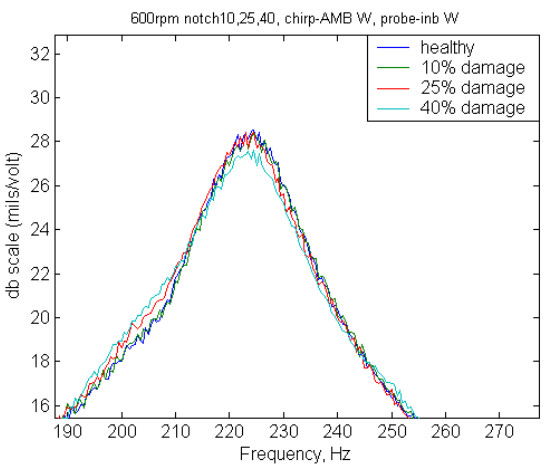

Figure 4.19. Second mode of a midspan notch at 600 rpm measured at the 45° inboard probe with W-axis AMB chirp.

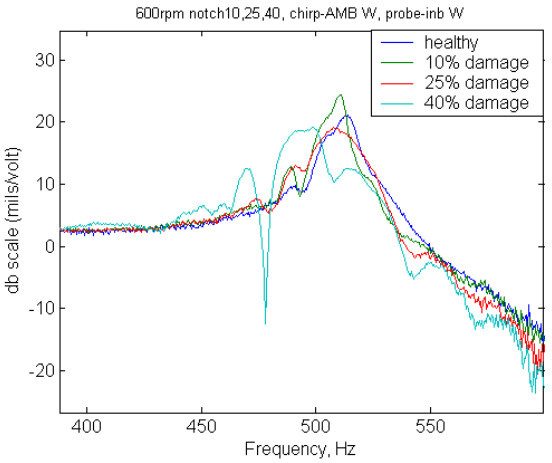

Figure 4.20. Third mode of a midspan notch at 600 rpm measured at the 45° inboard probe with W-axis AMB chirp.

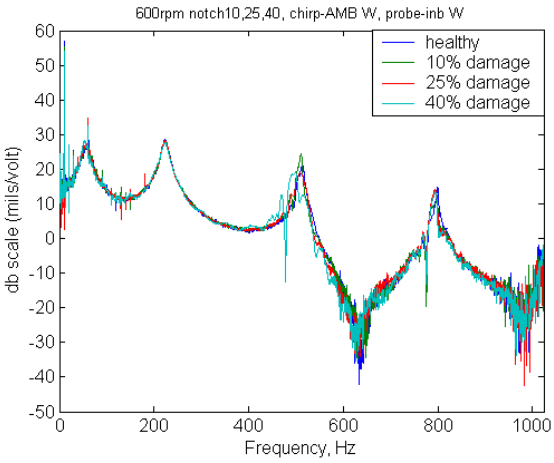

Figure 4.21. Full spectrum of a midspan notch at 600 rpm measured at the 45° inboard probe with W-axis AMB chirp.

4.3.1 2400 rpm test speed

Data for the 2400 rpm test speed is next. The FRFs at this running speed show a lot of noise in the spectrum. As mentioned before, some of this noise is due to the AMB controller and some is due to running speed components.

FFTs for the 2400 rpm test speed can be seen in Figures 4.22, 4.23, 4.24, and 4.25 for a healthy, 10%, 25%, and 40% notched shaft, respectfully. As the notch gets deeper, the 1X amplitude originally at 4.8 mils p-p decreases to 1.5 mils p-p. The amplitude continues to grow for the next two notch depths with the last notch depth of 40% requiring a small amount of balance weight to safely reach 2400 rpm. This was due to the bow induced in the shaft as well as the removal of shaft material. Also note the lack of significant running speed harmonics.

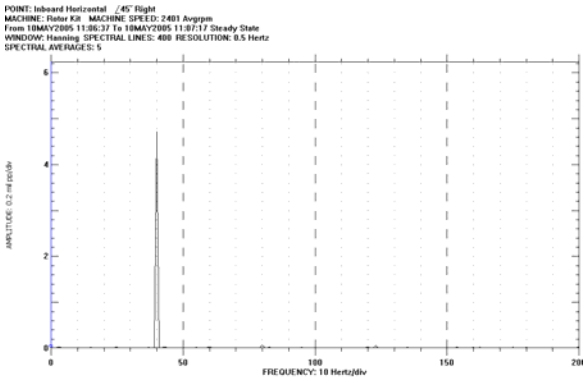

Figure 4.22. FFT of healthy shaft at inboard 45° axis running at 2400rpm.

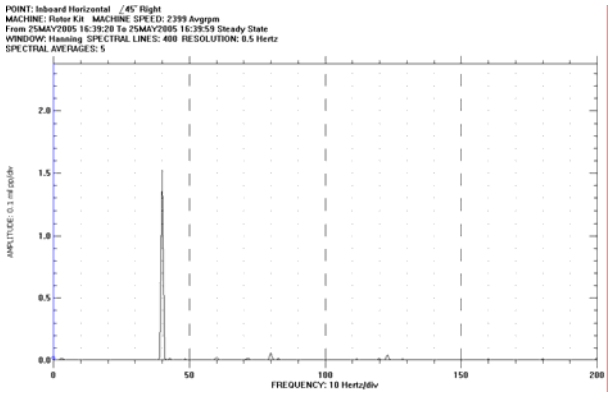

Figure 4.23. FFT of shaft with 10% notch at inboard 45° axis running at 2400rpm.

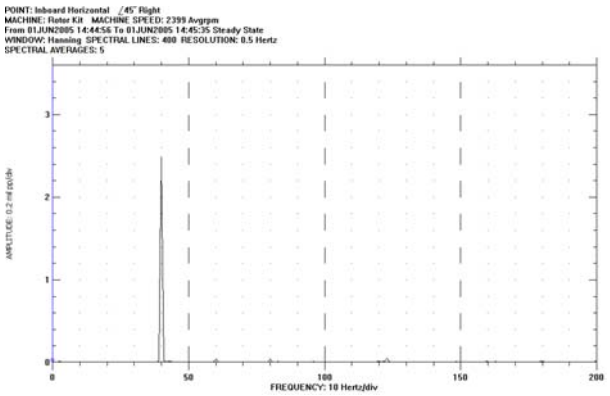

Figure 4.24. FFT of shaft with 25% notch at inboard 45° axis running at 2400rpm.

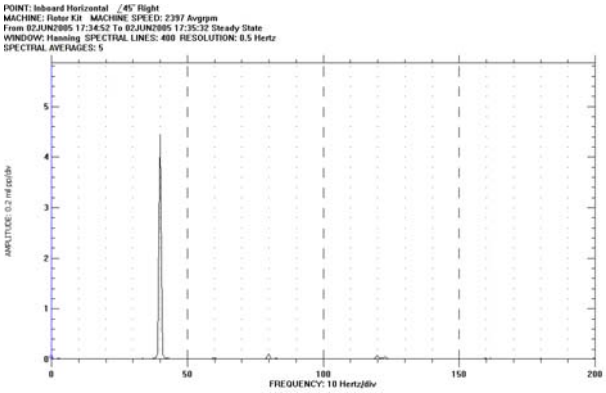

Figure 4.25. FFT of shaft with 40% notch at inboard 45° axis running at 2400rpm.

Unlike the 600 rpm case, the change in third mode is more clearly progressive for every increase in notch depth as shown in Figure 4.26, but the first and second modes still do not change as shown in Figures 4.27 and 4.28. The full spectrum plot is shown in Figure 4.29. Another observation to make is the split in third mode. The healthy shaft has this split, and the responses from the notches also have a split just with lower frequency. One other interesting feature to notice is the increase in magnitude ripple as the notch depths increase. This ripple is evident early on with the 10% notch, but it really grows as the damage worsens. If the change in the higher frequency peak is compared, a 10% notch has a 3 hz change in mode frequency. This increases to 7.5 hz for the 25% notch case, and 18 hz for the 40% case.

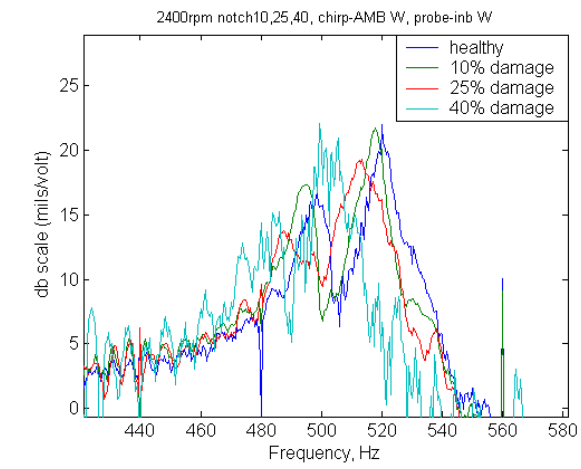

Figure 4.26. Third mode of a midspan notch at 2400 rpm measured at the 45° inboard probe with W-axis AMB chirp.

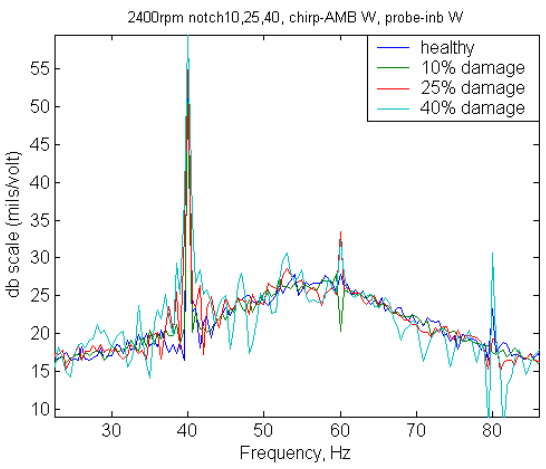

Figure 4.27. First mode of a midspan notch at 2400 rpm measured at the 45° inboard probe with W-axis AMB chirp.

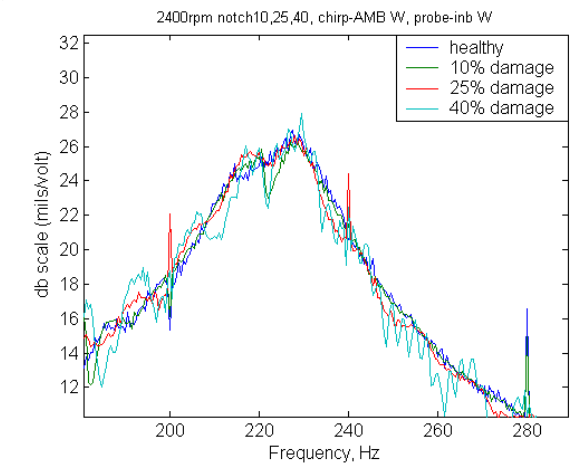

Figure 4.28. Second mode of a midspan notch at 2400 rpm measured at the 45° inboard probe with W-axis AMB chirp.

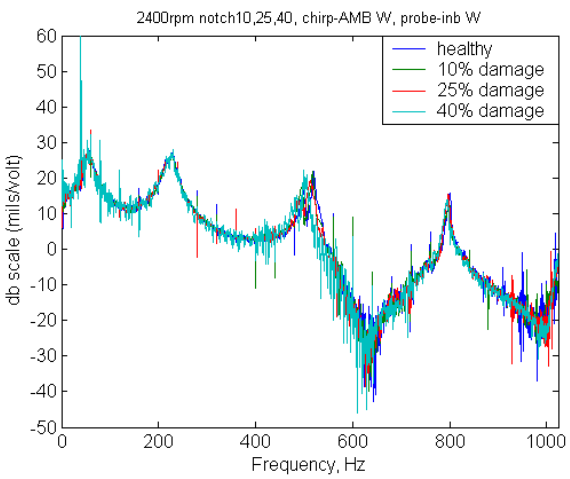

Figure 4.29. Full spectrum of a midspan notch at 2400 rpm measured at the 45° inboard probe with W-axis AMB chirp.

4.3.1 5100 rpm test speed

The last dynamic test speed is 5100 rpm. This was the more difficult speed to test because it required passing thru the first critical speed, which under normal shaft conditions was not a problem. However, as the notch depth increased, the shaft bow and unbalance would also increase. Too much shaft bow can make balancing difficult. The run up for this final speed with a 40% notch post balanced can be seen in Figure 4.30. Responses from the FFTs can be seen in Figures 4.31, 4.32, 4.33, and 4.34 for a healthy, 10%, 25%, and 40% notched shaft, respectfully. These plots may not be good indicators of changes caused by the notch due to the amount of growing shaft bow.

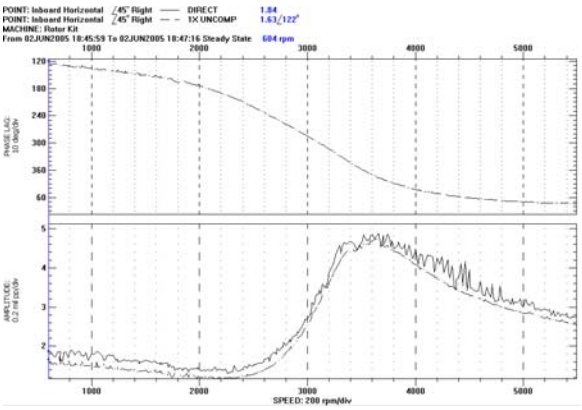

Figure 4.30. Balanced run-up for 40% notch.

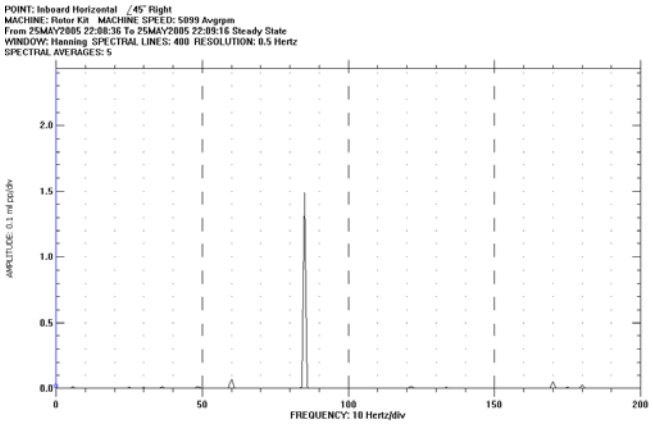

Figure 4.31. FFT of healthy shaft at inboard 45° axis running at 2400rpm.

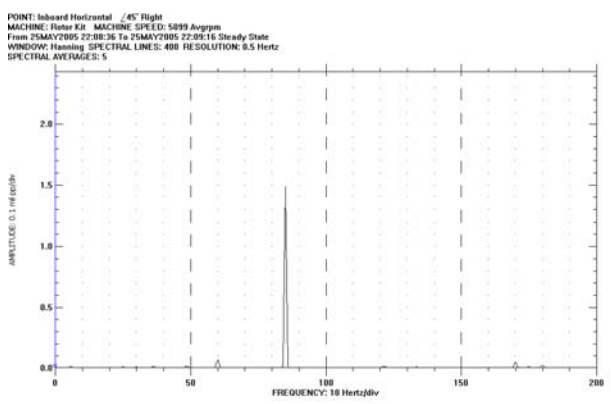

Figure 4.32. FFT of shaft with 10% notch at inboard 45° axis running at 5100rpm.

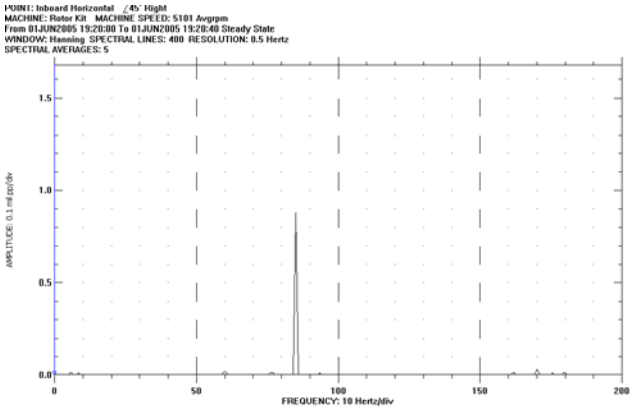

Figure 4.33. FFT of shaft with 25% notch at inboard 45° axis running at 5100rpm.

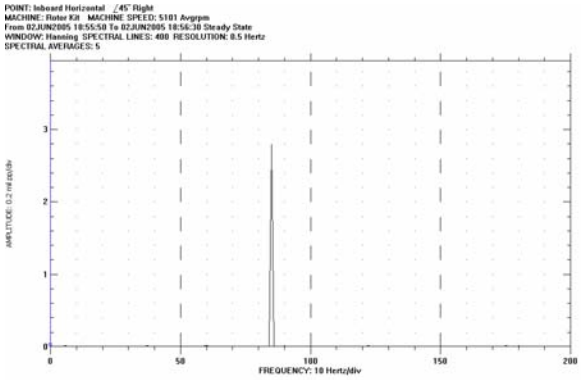

Figure 4.34. FFT of shaft with 40% notch at inboard 45° axis running at 5100rpm.

The FRF data for this 5100 rpm speed resembles that of the static and 600 rpm case with low contrast between the 10 and 25% notch depth as shown in Figure 4.35 for the full spectrum plot. There is still no change in the first and second modes as shown in Figure 4.36 and 4.37. Frequency shifts for the 10 and 25% notch depth do vary from that of the healthy shaft by 3 Hz for the higher frequency peak of the third mode but by the same amount. A notch depth of 40% has the largest frequency shift of approximately 15 Hz as seen in Figure 4.38.

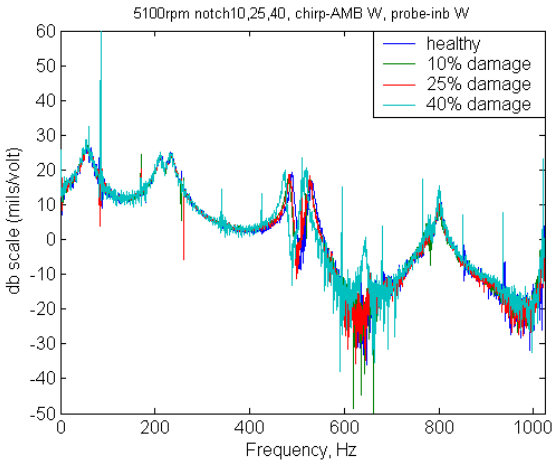

Figure 4.35. Full spectrum of a midspan notch at 5100 rpm measured at the 45° inboard probe with W-axis AMB chirp.

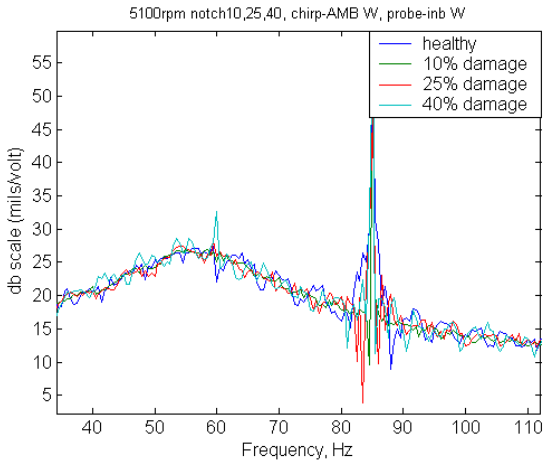

Figure 4.36. First mode of a midspan notch at 5100 rpm measured at the 45° inboard probe with W-axis AMB chirp.

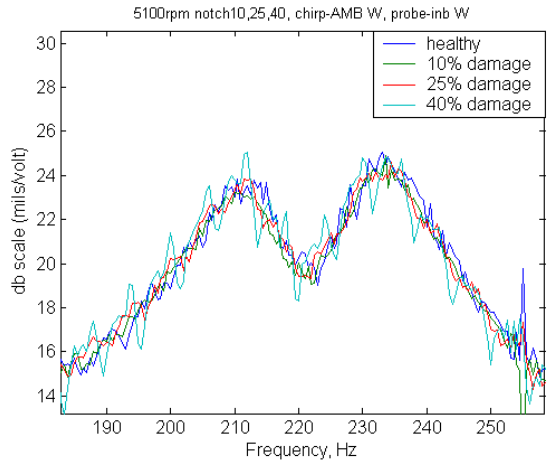

Figure 4.37. Second mode of a midspan notch at 5100 rpm measured at the 45° inboard probe with W-axis AMB chirp.

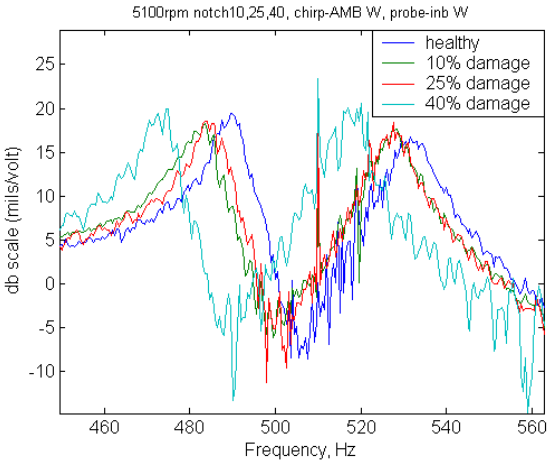

Figure 4.38. Third mode of a midspan notch at 5100 rpm measured at the 45° inboard probe with W-axis AMB chirp.

4.4 Chapter Four Summary

Static testing was at times inconclusive when comparing the difference between 10% and 25% notch depth, but the 40% notch depth consistently showed a decreasing frequency shift in the third mode up to 25 Hz depending on which direction the notch faced with respect to the direction of applied force. Another interesting find is the splitting of this third mode with damage. This split shows up when the notch is faced in some direction other than the forcing

direction. Therefore, the split is not seen when the notch faces the forcing axis and when the notch is facing 90° away from the forcing axis. Dynamic testing with a notch yielded similar results. At times the difference between the 10 and 25% notch is negligible, but the difference between the 40% notch and the healthy shaft can be as high as 19 hz. A summary of the static and dynamic notch results can be seen in Table 4.2.

Table 4.2. Summary of static and dynamic third mode frequency shifts due to progressive notch.

	Shaft notch depth		
Notch Angle	*10%*	*25%*	*40%*
90°	6.5(-1.26%)	4.5(-0.87%)	12(-2.32%)
255°	7(-1.35%)	9(-1.74%)	25(-4.84%)
Speed (rpm)	*10%*	*25%*	*40%*
600	3.5(-0.68%)	5.5(-1.07%)	19(-3.70%)
2400	2.5(-0.48%)	7(-1.35%)	18(-3.46%)
5100	3.5(-0.66%)	4(-0.75%)	13(-2.45%)

*Values shown in Hz and percent change.

Chapter Five

EDM Notch Results

5.1 Introduction to EDM Notch Shaft

The final goal of this research was to mimic a crack as closely as possible. With the notch work done, a smaller notch could be investigated. A wire EDM machine was able to cut a midspan 25 and 40% notch into two shafts with an approximate notch width of 0.0027 inches (0.069mm). The same types of static and dynamic testing were performed with the EDM notch as were with the regular notch, but a change in AMB placement was also investigated. This would verify if changes in the third mode would still occur with forcing from a different axial location.

5.2 Static EDM Notched Shaft Results for midspan AMB setup

Up until this time, the same shaft was used to conduct the rub and notch testing, but with the switch to the EDM shafts this was about to change. One downside to using the EDM shaft is the lack of a healthy baseline from that shaft. Instead, a healthy case was taken from an undamaged shaft for reference. The first data discussed will come from the same midspan configuration used up to this point with a W-axis chirp. As with the static notch, only 90° and 225° facing EDM notches will be used of the five notch directions. These plots can be seen in Figures 5.1 and 5.2 for the full spectrum, respectfully. Zoomed plots of the first and second mode for the 90° facing EDM notch are shown in Figures 5.3 and 5.4, and Figures 5.5 and 5.6 show the first and second modes for the 225° EDM notch. The zoomed third mode is shown in Figures 5.7 and 5.8. It appears that the EDM notch still behaves much like a large notch with respect to the third mode splitting when the notch faces some other direction besides the axis of forcing. The only exception to this is the 135° axis seen in Figure 5.9. A summary of the 90° and 225° facing EDM notch is shown in Table 5.1. Values given in Table 5.1 show change in

third mode frequency with respect to a healthy shaft as well as the percent change measured at the inboard 45° probe.

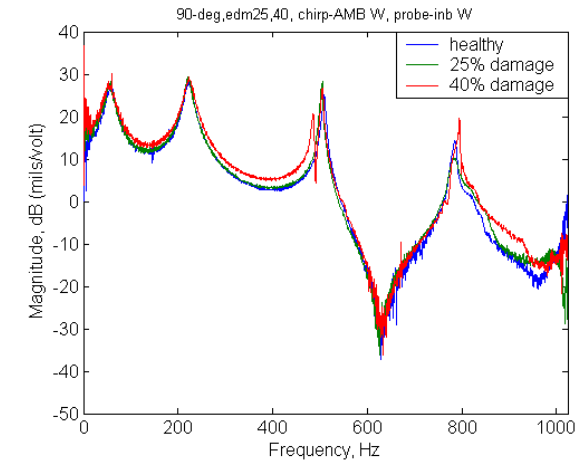

Figure 5.1. Response of a healthy, 25%, and 40% 90° facing EDM notch measured at the 45° inboard probe with W-axis AMB chirp.

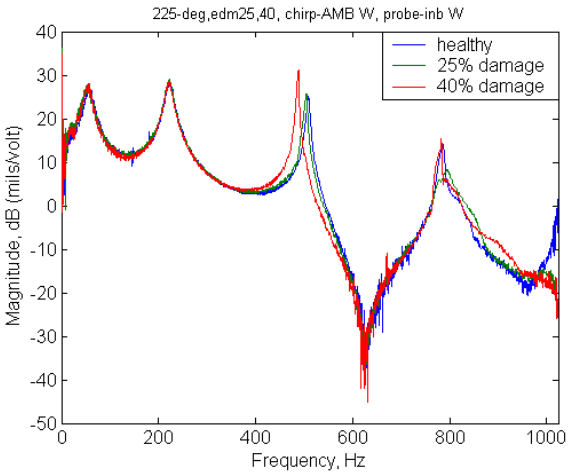

Figure 5.2. Response of a healthy, 25%, and 40% 225° facing EDM notch measured at the 45° inboard probe with W-axis AMB chirp.

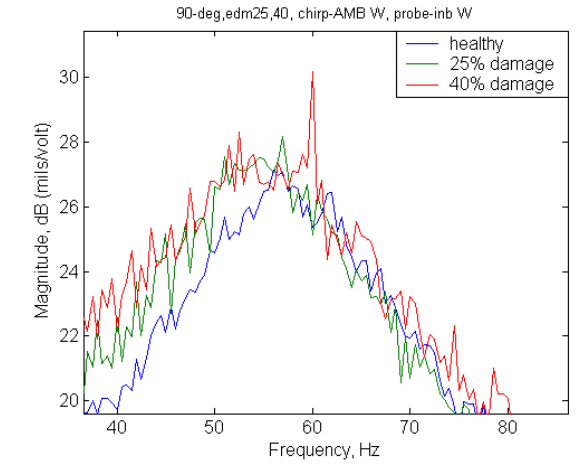

Figure 5.3. First mode of a healthy, 25%, and 40% 90° facing EDM notch measured at the 45°inboard probe with W-axis AMB chirp.

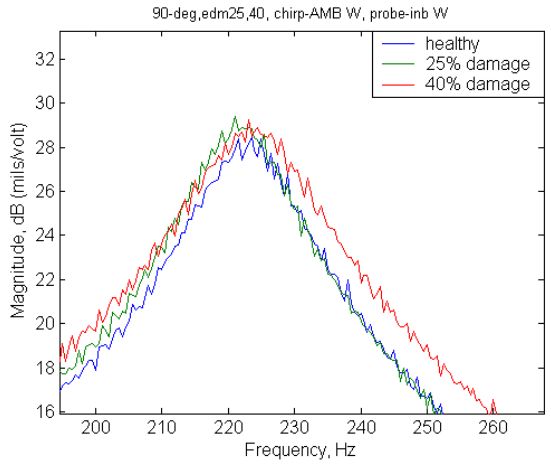

Figure 5.4. Second mode of a healthy, 25%, and 40% 90° facing EDM notch measured at 45° inboard probe with W-axis AMB chirp.

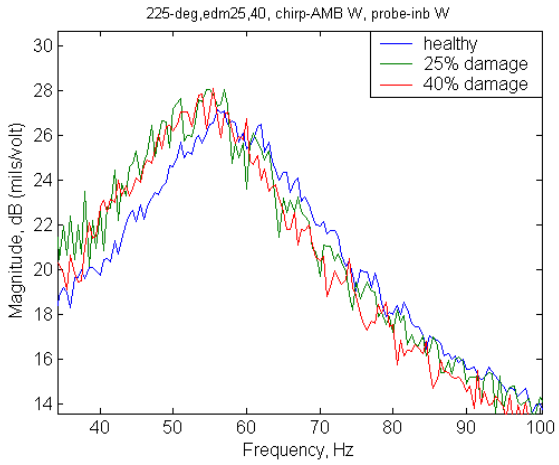

Figure 5.5. First mode of a healthy, 25%, and 40% 225° facing EDM notch measured at the 45°inboard probe with W-axis AMB chirp.

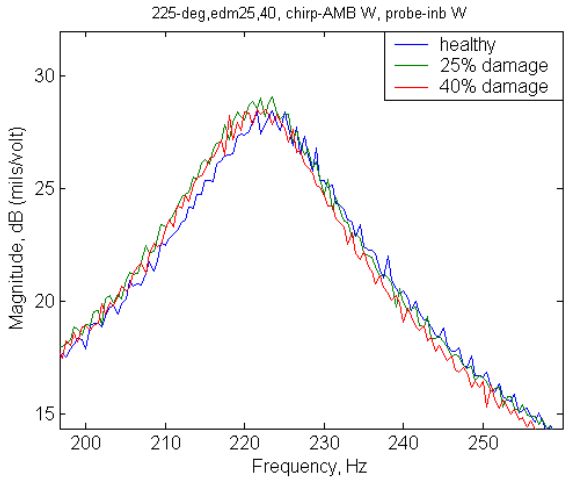

Figure 5.6. Second mode of a healthy, 25%, and 40% 225° facing EDM notch measured at 45° inboard probe with W-axis AMB chirp.

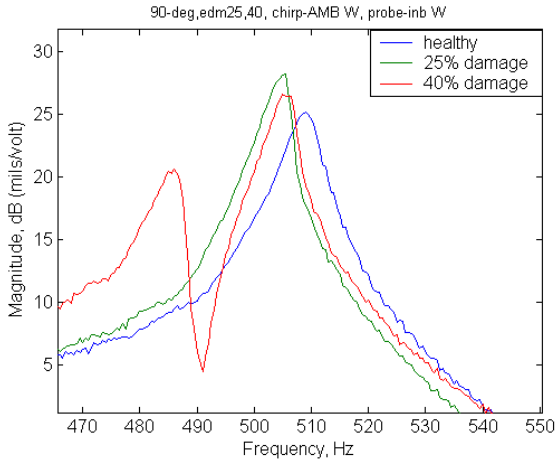

Figure 5.7. Third mode of a healthy, 25%, and 40% 90° facing EDM notch measured at the 45°inboard probe with W-axis AMB chirp.

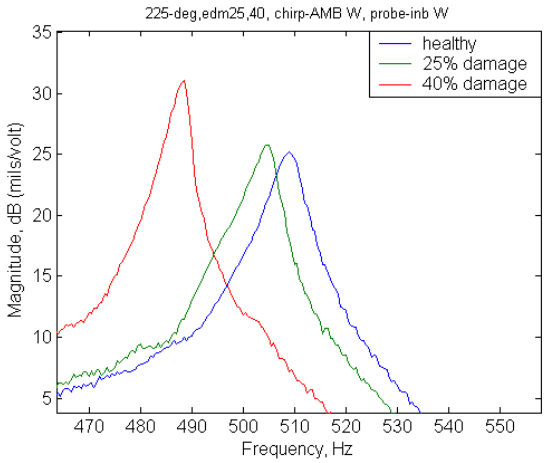

Figure 5.8. Third mode of a healthy, 25%, and 40% 225° facing EDM notch measured at 45° inboard probe with W-axis AMB chirp.

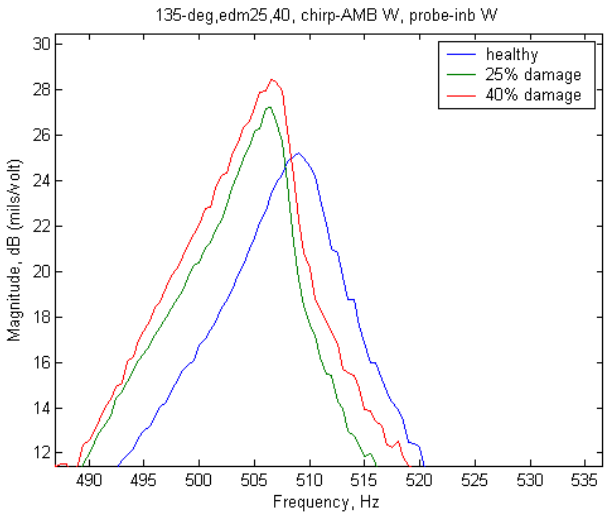

Figure 5.9. Third mode of a healthy, 25%, 40% 135° facing EDM notch measured at the 45° inboard probe with W-axis AMB chirp.

Table 5.1. Change in third mode frequency for both 90° and 225° facing EDM notch depths at the inboard 45° probe shown in Hz and percent change for the midspan AMB.

	Shaft notch depth	
Notch Angle	*25%*	*40%*
90°	3.5(-0.69%)	3.5(-0.69%)
255°	4.5(-0.88%)	20.5(-4.03%)

*Values shown in Hz and percent change.

5.3 Static EDM Notched Shaft Results for outboard AMB setup

When the test rig is setup with the AMB in the outboard position seen in Figure 5.10, there is a general frequency shift down for all the modes. This is due likely to the shaft length between the inboard ball bearing and the AMB getting larger. To keep with the established format, Figures 5.11 and 5.12 will show the full spectrum response of the 90° facing and 225° facing static cases, and Figures 5.13, 5.14, 5.15, and 5.16 will show the zoomed portions of the first and second mode for the 90° and 225° facing notch, respectively. The third mode for both the 90° and 225° facing EDM notch can be seen in Figures 5.17 and 5.18. Even with the different AMB position, the third mode still splits when the notch is facing a direction other than the forcing axis. The 135° facing EDM notch also shows some decrease in frequency in the third mode shown in Figure 5.19. With the AMB positioned further away, there seems to be less frequency change with damage. For example, the 90° positioned 25% EDM notch shows a 3.5

Hz change, and the 40% scenario shows only a 6 Hz difference. Results for the 225° axis show a 3.5 Hz change with 25% damage, but approximately 19.5 Hz difference for the 40% case.

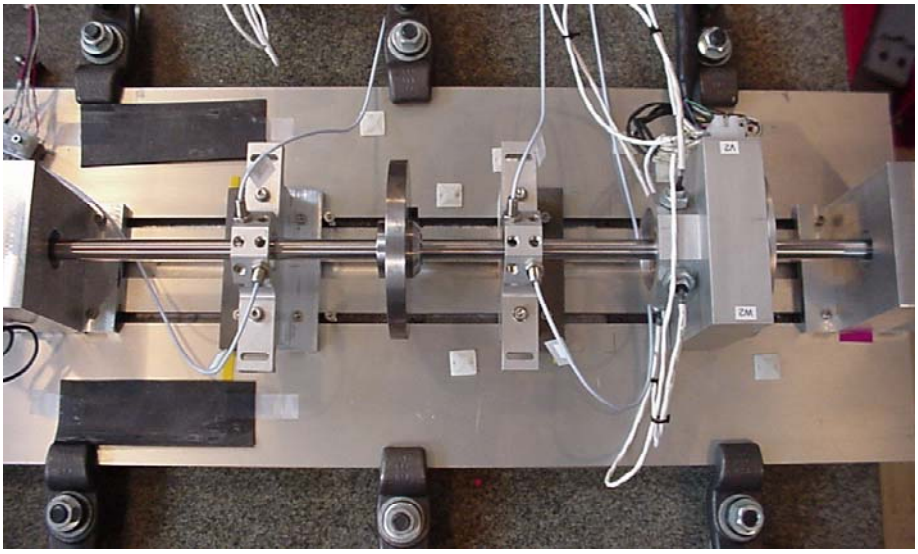

Figure 5.10. Outboard AMB setup.

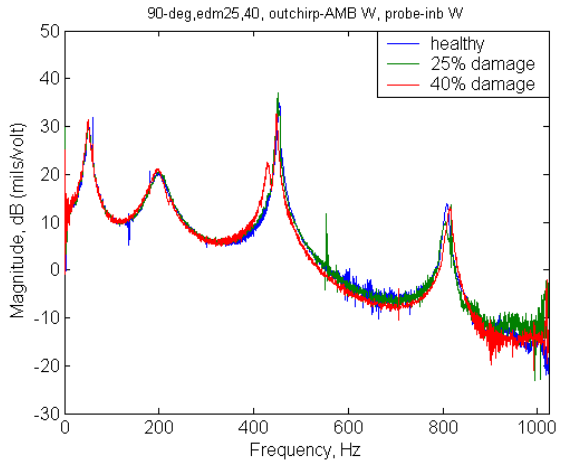

Figure 5.11. Response of a healthy, 25%, and 40% 90° facing EDM notch measured at the 45° inboard probe with W-axis outboard AMB. chirp.

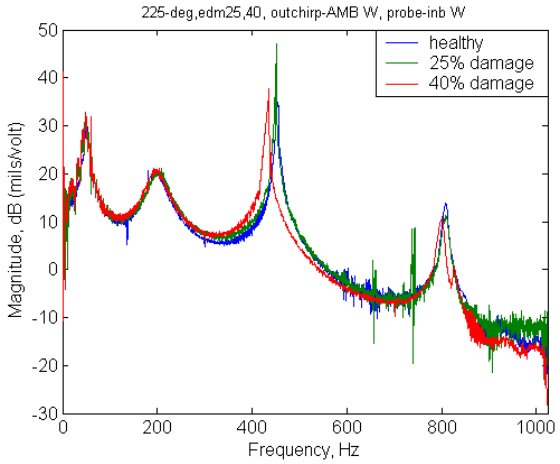

Figure 5.12. Response of a healthy, 25%, and 40% 225° facing EDM notch measured at the 45° inboard probe with W-axis outboard AMB chirp.

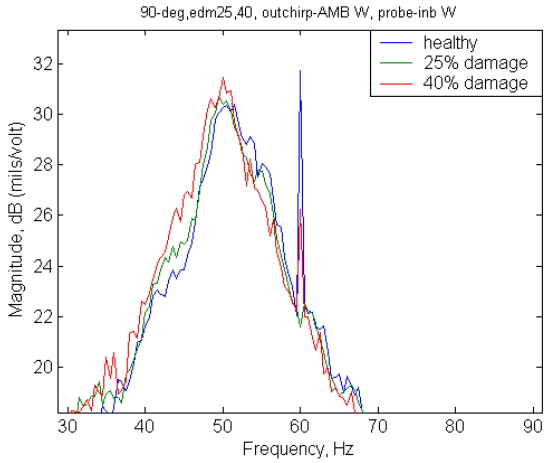

Figure 5.13. First mode of a healthy, 25%, and 40% 90° facing EDM notch measured at the 45°inboard probe with W-axis outboard AMB chirp.

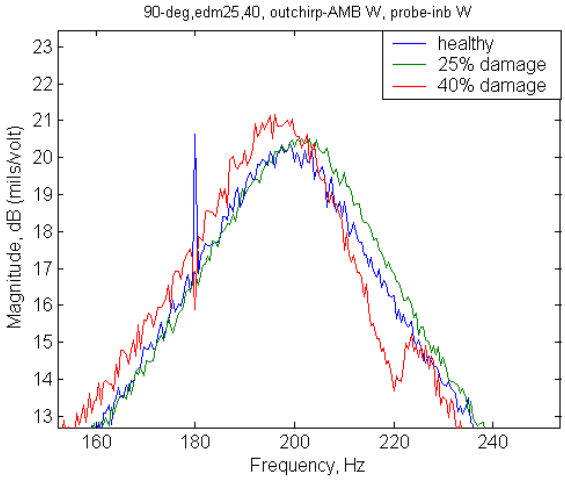

Figure 5.14. Second mode of a healthy, 25%, and 40% 90° facing EDM notch measured at 45° inboard probe with W-axis outboard AMB chirp.

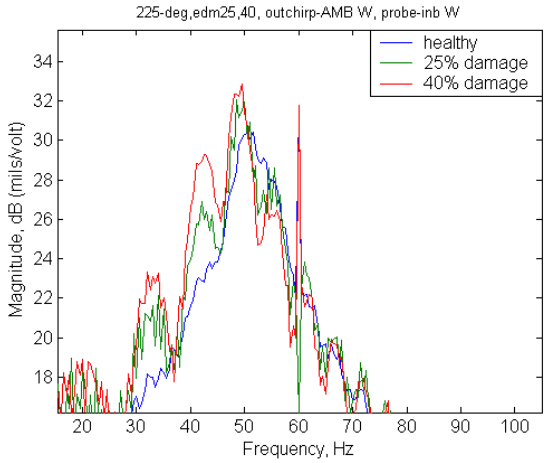

Figure 5.15. First mode of a healthy, 25%, and 40% 225° facing EDM notch measured at the 45°inboard probe with W-axis outboard AMB chirp.

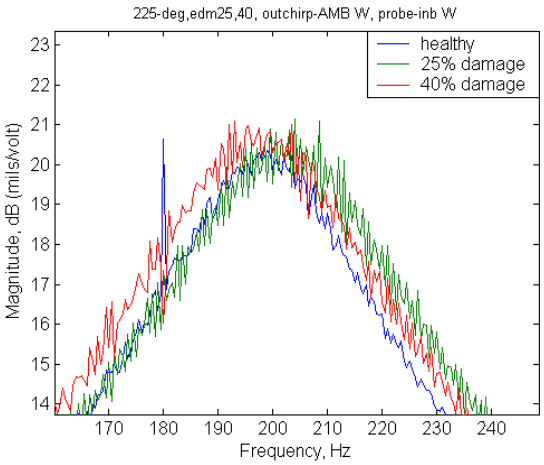

Figure 5.16. Second mode of a healthy, 25%, and 40% 225° facing EDM notch measured at 45° inboard probe with W-axis outboard AMB chirp.

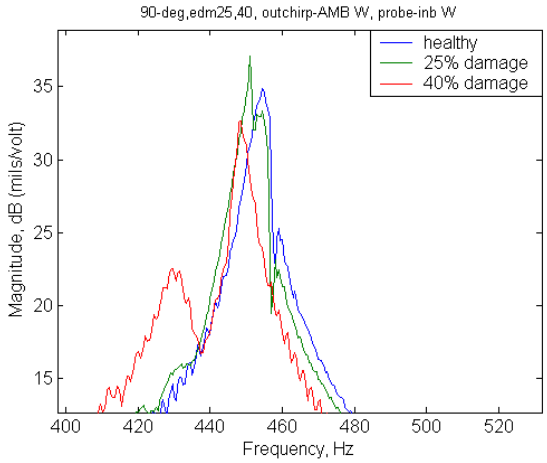

Figure 5.17. Third mode of a healthy, 25%, and 40% 90° facing EDM notch measured at the 45°inboard probe with W-axis outboard AMB chirp.

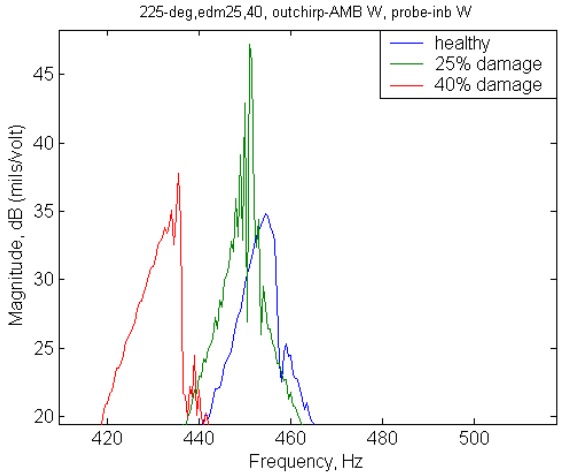

Figure 5.18. Third mode of a healthy, 25%, and 40% 225° facing EDM notch measured at 45° inboard probe with W-axis outboard AMB chirp.

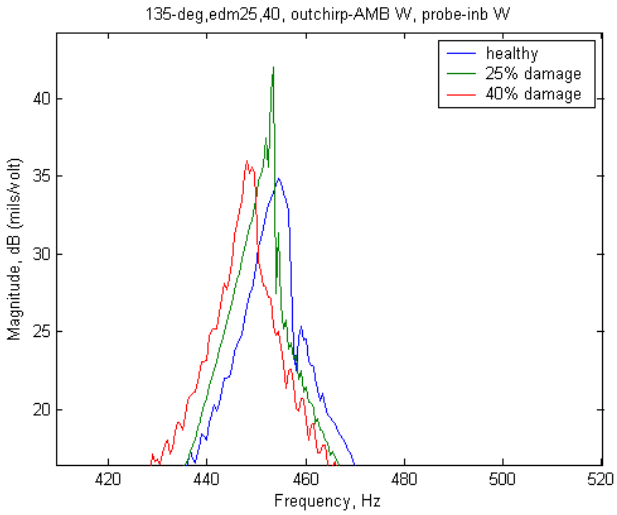

Figure 5.19. Third mode of a healthy, 25%, 40% 135° facing EDM notch measured at the 45° inboard probe with W-axis outboard AMB chirp.

Table 5.2. Change in third mode frequency for both 90° and 225° facing EDM notch depths at the inboard 45° probe shown in Hz and percent change for the outboard AMB.

	Shaft notch depth	
Notch Angle	*25%*	*40%*
90°	3.5(-0.77%)	6(-0.1.32%)
255°	3.5(-0.77%)	19.5(-4.29%)

*Values shown in Hz and percent change.

5.4 Dynamic EDM Notched Shaft Results for midspan AMB

Dynamic testing will again be performed at 600, 2400, and 5100 rpm. The first dynamic results are FFT plots for the midspan AMB placement seen in Figures 5.20, 5.21, and 5.22. These results do not vary much, with 1X amplitudes holding steady, but there is a possible increase in harmonic amplitudes for the 40% EDM notch. Although small, the 40% EDM 2X component doubles to about a 0.1 mils peak to peak (p-p) up from the 0.05mils p-p in the previous healthy case. This observation by itself means little when compared to the amount of amplitude seen in the healthy case.

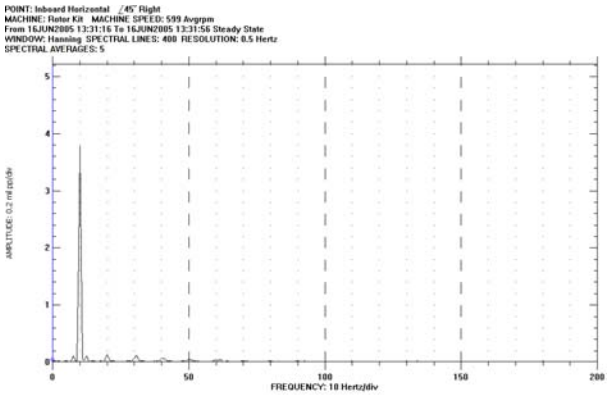

Figure 5.20. FFT at inboard 45° probe of healthy shaft running at 600rpm with midspan AMB.

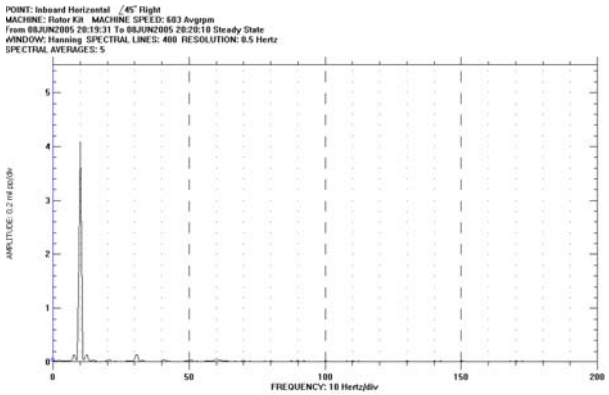

Figure 5.21. FFT at inboard 45° probe of 25% EDM notch running at 600rpm with midspan AMB.

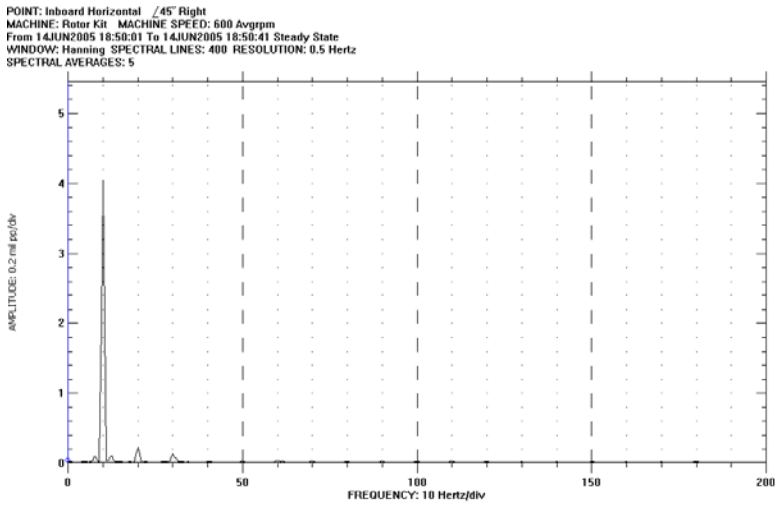

Figure 5.22. FFT at inboard 45° probe of 40% EDM notch running at 600 rpm with midspan AMB.

Results for the FRF data look promising with good separation between the 25% and 40% EDM notch as seen in Figure 5.23 for the 45° inboard probe. The first and second modes show no change and are shown in Figures 5.24 and 5.25. A zoomed section of the third mode can be seen in Figure 5.26. This zoomed section shows a 6.5 Hz drop between the healthy shaft and the 25% EDM notched shaft as well as a 13.5 Hz difference for the 40% EDM shaft. Note the lack of change for the first and second modes for all three cases. There are actually changes in the fourth mode as well as shown in Figure 5.27, but these are not consistent for each damage case.

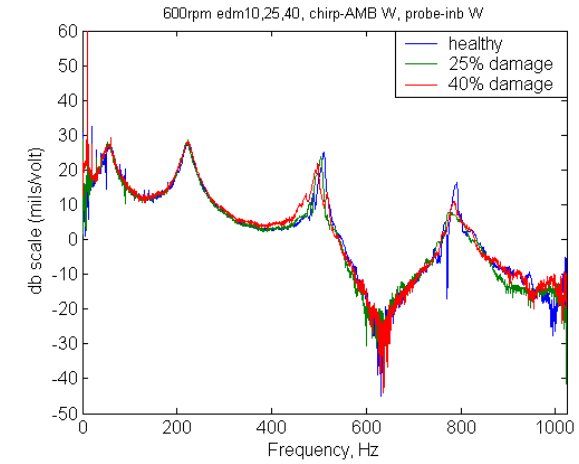

Figure 5.23. Full spectrum of an EDM notch at 600 rpm measured at the 45° inboard probe with W-axis midspan AMB chirp.

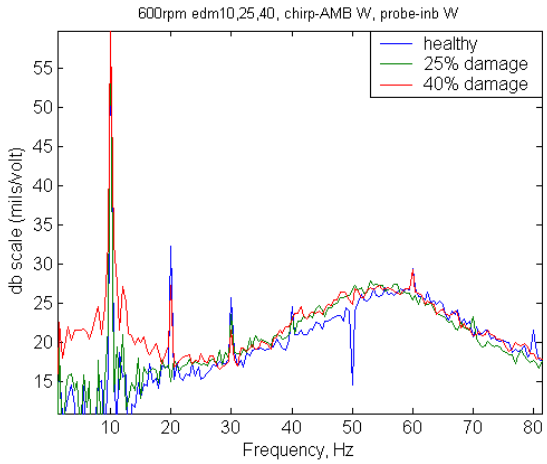

Figure 5.24. First mode of an EDM notch at 600 rpm measured at the 45° inboard probe with W-axis midspan AMB chirp.

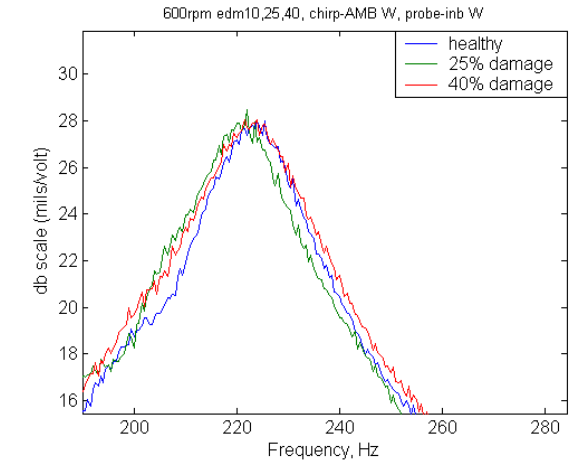

Figure 5.25. Second mode of an EDM notch at 600 rpm measured at the 45° inboard probe with W-axis midspan AMB chirp.

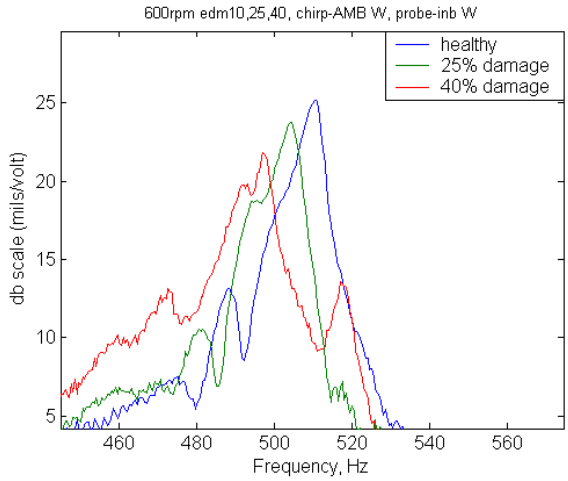

Figure 5.26. Third mode of an EDM notch at 600 rpm measured at the 45° inboard probe with W-axis midspan AMB chirp.

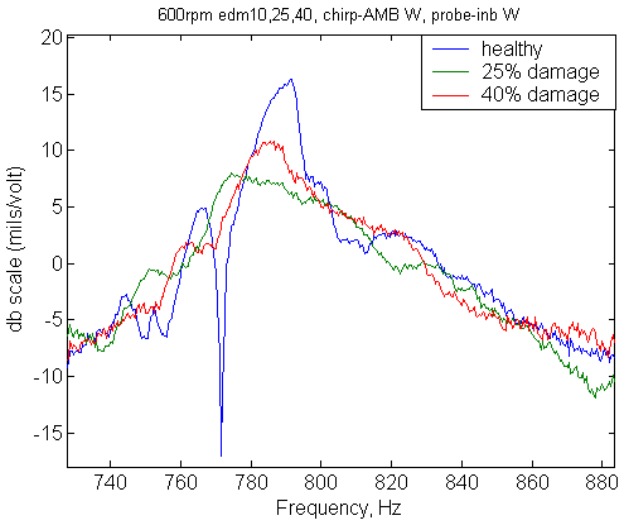

Figure 5.27. Fourth mode of an EDM notch at 600 rpm measured at the 45° inboard probe with W-axis midspan AMB chirp.

The next results are for the midspan AMB at 2400 rpm. Again, FFT data was taken with ADRE® as seen in Figures 5.28, 5.29, and 5.30. Amplitudes for the 1X component do increase in this case, but not uniformly. As with the 600 rpm speed, there is a mild 2X component for the 40% EDM notch, but otherwise not much change.

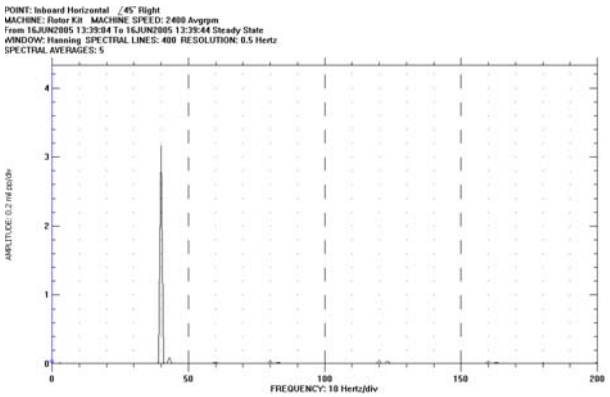

Figure 5.28. FFT at inboard 45° probe of healthy shaft running at 2400rpm with midspan AMB.

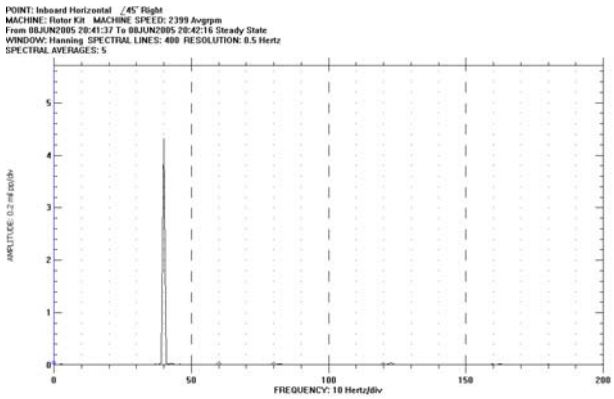

Figure 5.29. FFT at inboard 45° probe of 25% EDM notch running at 2400rpm with midspan AMB.

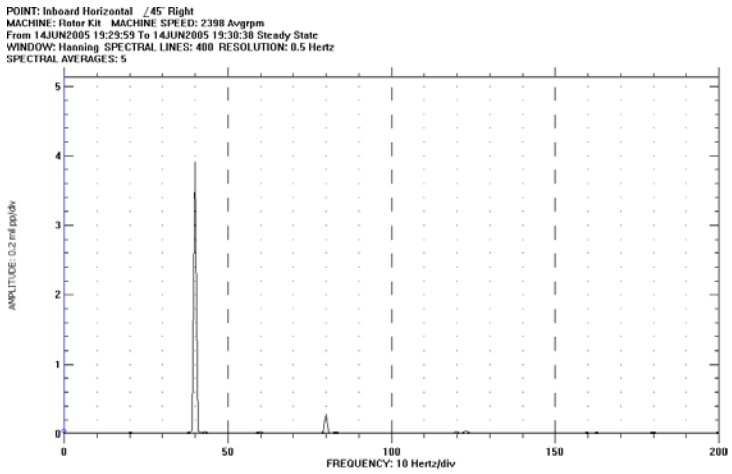

Figure 5.30. FFT at inboard 45° probe of 40% EDM notch running at 2400 rpm with midspan AMB.

Results for the 2400 rpm speed using an FRF can be seen below in Figures 5.31, 5.32, 5.33, and 5.34 for the full spectrum, first mode, second mode, and third mode, respectfully. There is an approximate change of 7.5 Hz between the healthy shaft and the 25% EDM shaft if measured for the latter peaks, which has been the pattern in this paper. A 40% EDM notch shows a 11.5 Hz change from the healthy shaft, which is very similar to the change seen in the 600 rpm speed.

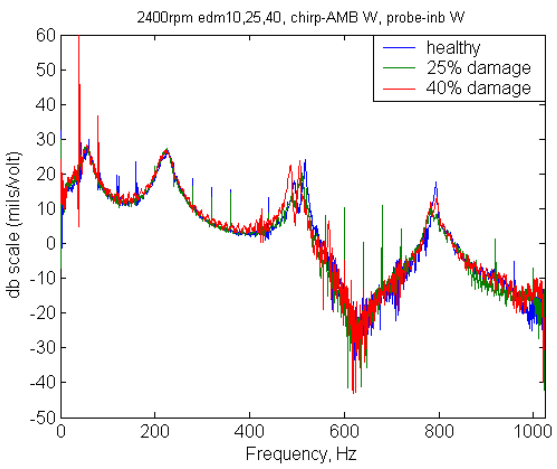

Figure 5.31. Full spectrum of an EDM notch at 2400 rpm measured at the 45° inboard probe with W-axis midspan AMB chirp.

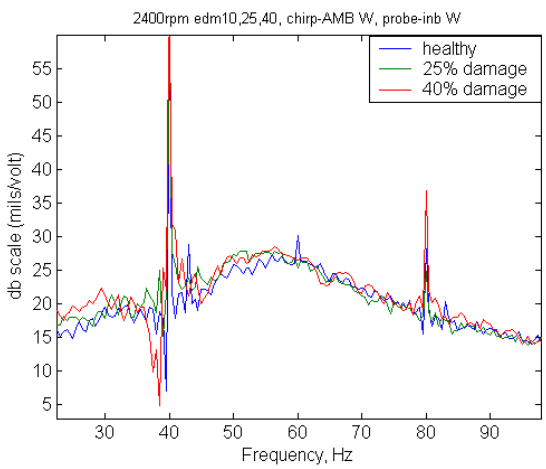

Figure 5.32. First mode of an EDM notch at 2400 rpm measured at the 45° inboard probe with W-axis midspan AMB chirp.

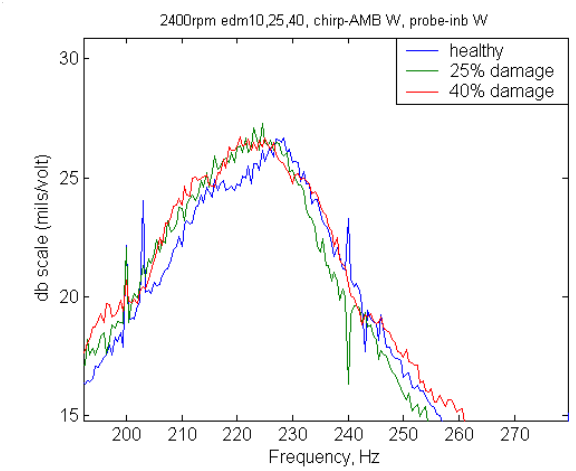

Figure 5.33. Second mode of an EDM notch at 2400 rpm measured at the 45° inboard probe with W-axis midspan AMB chirp.

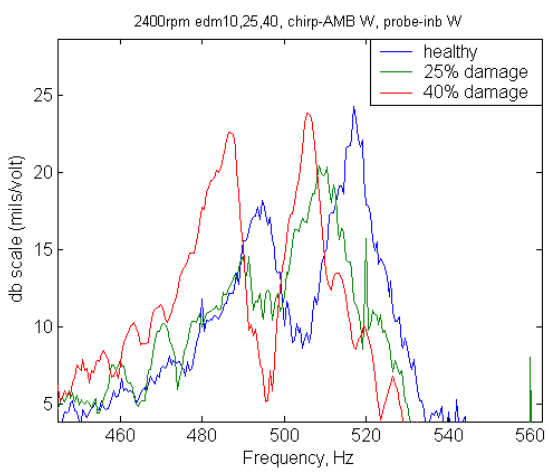

Figure 5.34. Third mode of an EDM notch at 2400 rpm measured at the 45° inboard probe with W-axis midspan AMB chirp.

The last dynamic results for the midspan AMB at 5100 rpm can be seen in Figures 5.35, 5.36, and 5.37. These results remain consistent with the 2400 and 600 rpm speeds. Amplitudes for the 1X component are actually slightly higher for the 600 rpm speed, but remain at 3 mils p-p for the 2400 and 5100 rpm speeds. The 2X component of the 40% EDM notch does show up again, but it is very small at 0.5 mils p-p.

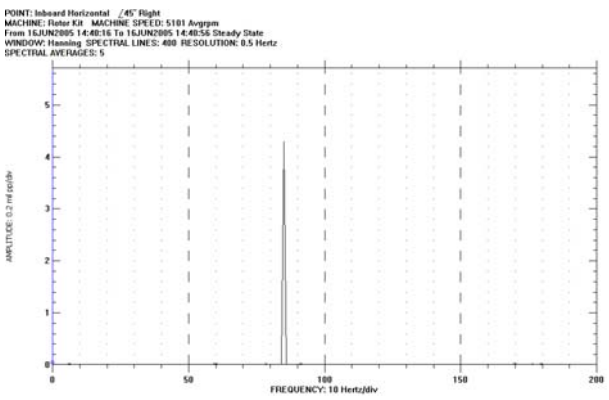

Figure 5.35. FFT at inboard 45° probe of healthy shaft running at 5100rpm with midspan AMB.

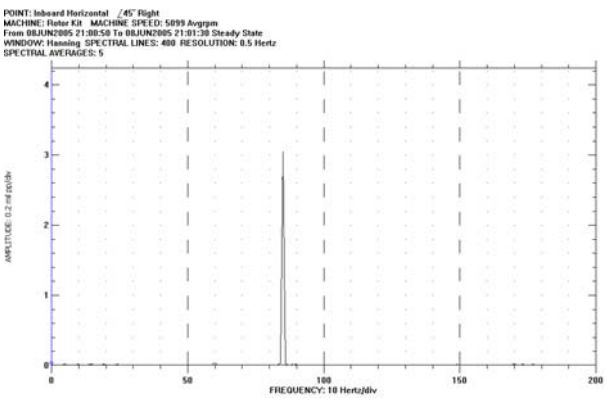

Figure 5.36. FFT at inboard 45° probe of 25% EDM notch running at 5100rpm with midspan AMB.

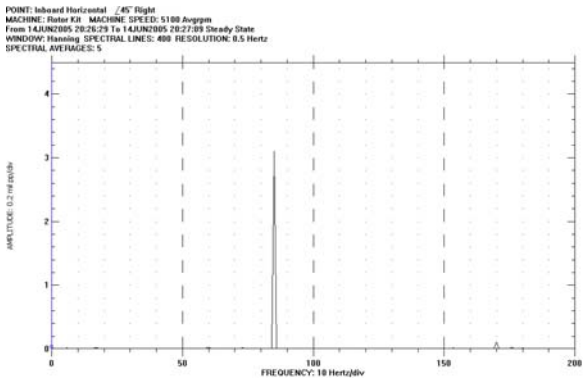

Figure 5.37. FFT at inboard 45° probe of 40% EDM notch running at 5100 rpm with midspan AMB.

The response for the midspan AMB at 5100 rpm still remains consistent with the previous speeds of 600 and 2400 rpm as shown in Figures 5.38, 5.39, 5.40, and 5.41 for the full spectrum, first mode, second mode, and third mode, respectfully. Although the 25% EDM notch case varies by 10.5 hz at 5100 rpm instead of the 6 or 7 hz seen by the previous speeds. Total difference by the 40% case is also slightly higher with a 14.5 hz drop from the healthy speed.

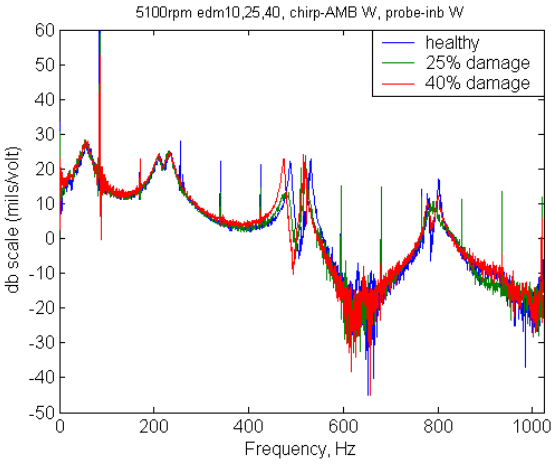

Figure 5.38. Full spectrum of an EDM notch at 5100 rpm measured at the 45° inboard probe with W-axis midspan AMB chirp.

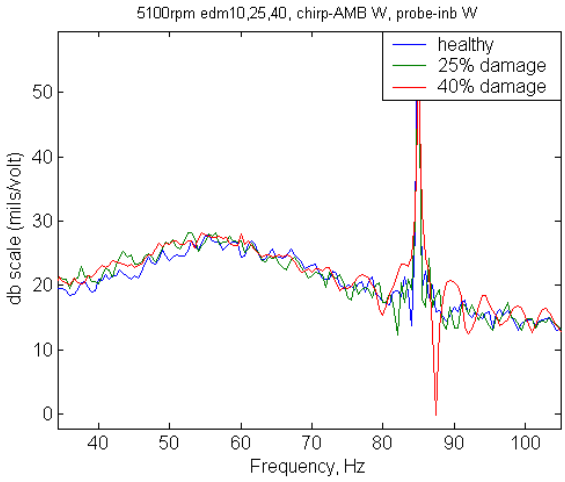

Figure 5.39. First mode of an EDM notch at 5100 rpm measured at the 45° inboard probe with W-axis midspan AMB chirp.

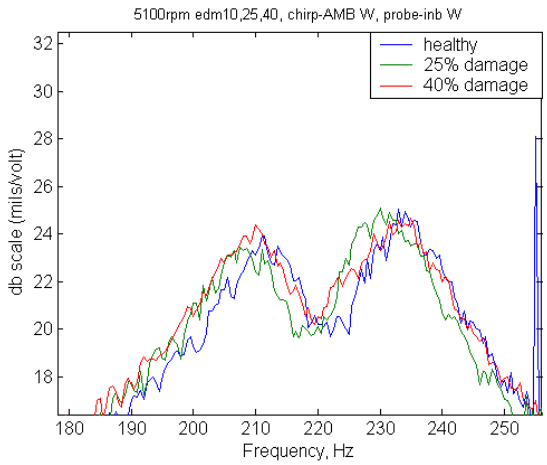

Figure 5.40. Second mode of an EDM notch at 5100 rpm measured at the 45° inboard probe with W-axis midspan AMB chirp.

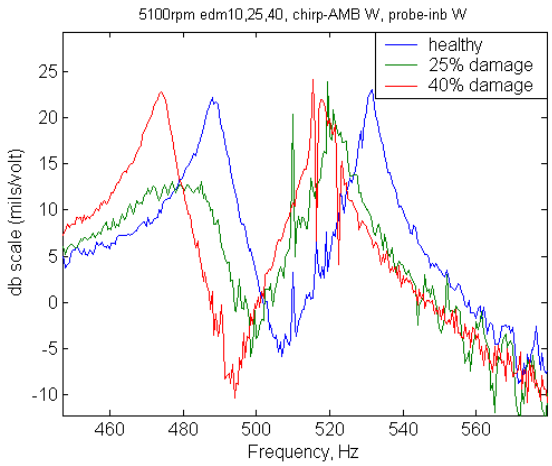

Figure 5.41. Third mode of an EDM notch at 5100 rpm measured at the 45° inboard probe with W-axis midspan AMB chirp.

Table 5.3. Change in third mode frequencies at 600, 2400, 5100 rpm for EDM notch depths at the inboard 45° probe shown in Hz and percent change for the midspan AMB.

	Shaft notch depth	
Speed (rpm)	*25%*	*40%*
600	6.5(-1.27%)	13.5(-2.64%)
2400	7.5(-1.45%)	11.5(-2.22%)
5100	10.5(-1.98%)	14.5(-2.73%)

*Values shown in Hz and percent change.

5.5 Dynamic EDM Notched Shaft Results for midspan AMB

The next series of data is for the outboard AMB position. This data is a repeat essentially of the first 600, 2400, and 5100 rpm test speeds. Amplitudes for the FFTs can be seen in Figures 5.42, 5.43, and 5.44. The 1X components actually increase as damage gets worse up to 8.5 mils p-p, but harmonics of running speed stay very low.

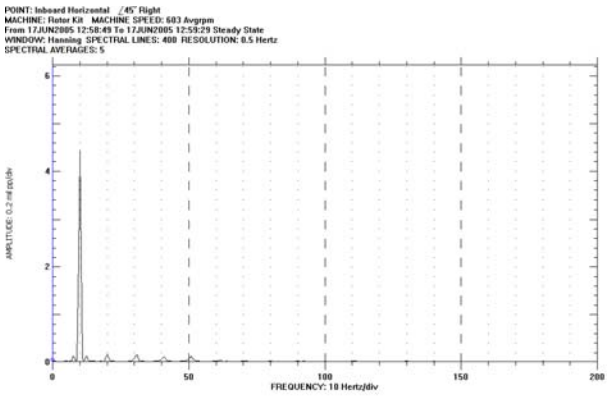

Figure 5.42. FFT at inboard 45° probe of healthy shaft running at 600rpm with outboard AMB.

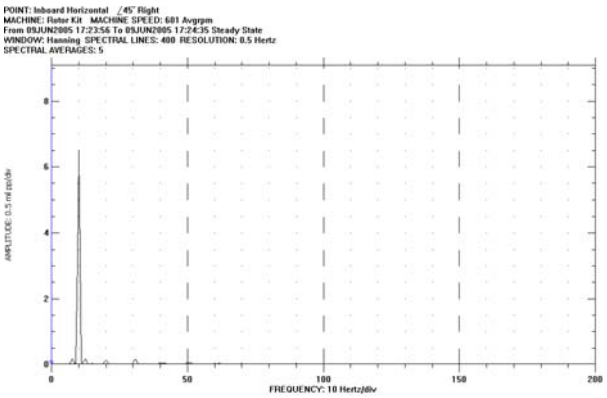

Figure 5.43. FFT at inboard 45° probe of 25% EDM notch running at 600rpm with outboard AMB.

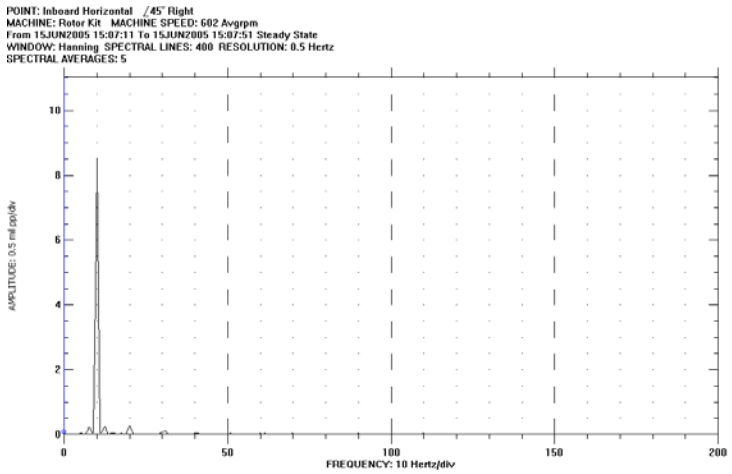

Figure 5.44. FFT at inboard 45° probe of 40% EDM notch running at 600 rpm with outboard AMB.

Data from the FRFs at 600 rpm for the outboard AMB can be seen in Figures 5.45, 5.46, 5.47, and 5.48 for the full spectrum, first mode, second mode, and third mode, respectfully. There seems to be more ripple in the magnitude response than compared to some of the midspan AMB tests. If the frequency peaks located to the right of the third mode are considered, then a 25% EDM notch loses about 3.5 Hz from the healthy shaft value, and the 40% EDM notch lowers by 14.5 Hz.

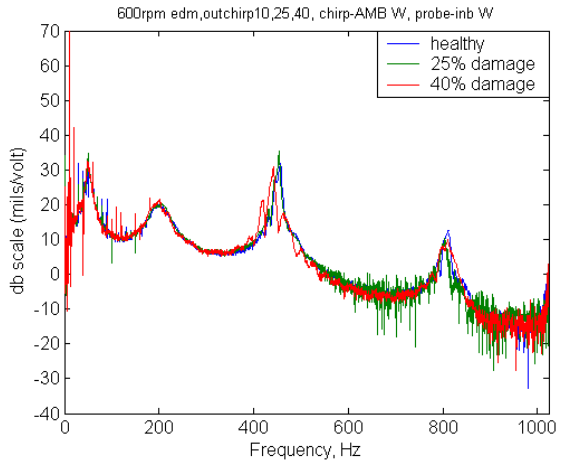

Figure 5.45. Full spectrum of an EDM notch at 600 rpm measured at the 45° inboard probe with W-axis outboard AMB chirp.

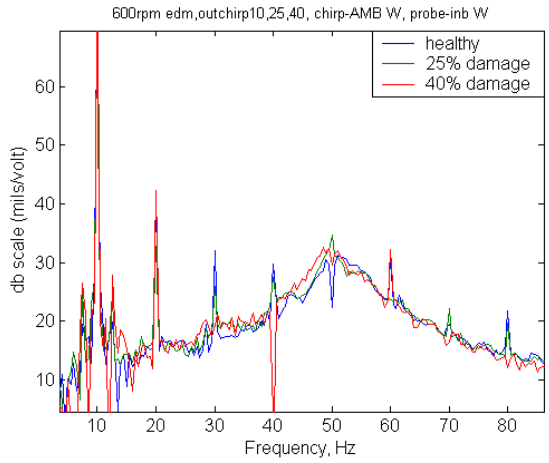

Figure 5.46. First mode of an EDM notch at 600 rpm measured at the 45° inboard probe with W-axis outboard AMB chirp.

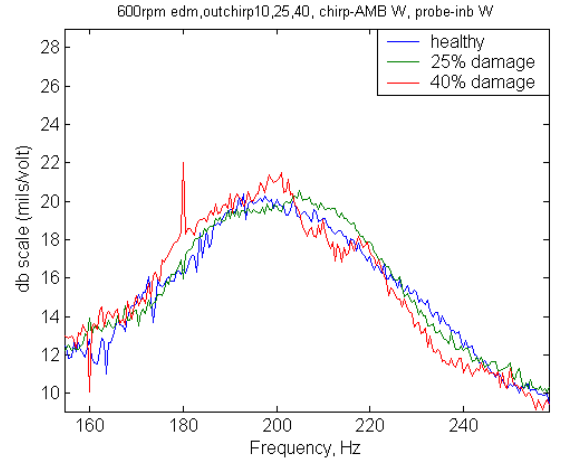

Figure 5.47. Second mode of an EDM notch at 600 rpm measured at the 45° inboard probe with W-axis outboard AMB chirp.

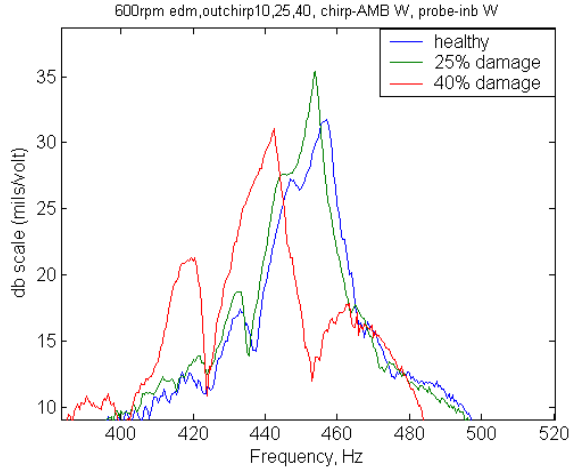

Figure 5.48. Third mode of an EDM notch at 600 rpm measured at the 45° inboard probe with W-axis outboard AMB chirp.

Spectrum data for the 2400 rpm outboard AMB can be seen in Figures 5.49, 5.50, 5.51. These FFT amplitudes for 2400 rpm are consistent with the changes seen in the 600 rpm case. Amplitudes for the 1X component start at 3.6 mils p-p and grow to 8 mils p-p for the 40% EDM notch case. There is still very little running speed harmonics with a possible 0.25 mils p-p for the 2X harmonic in Figure 5.51.

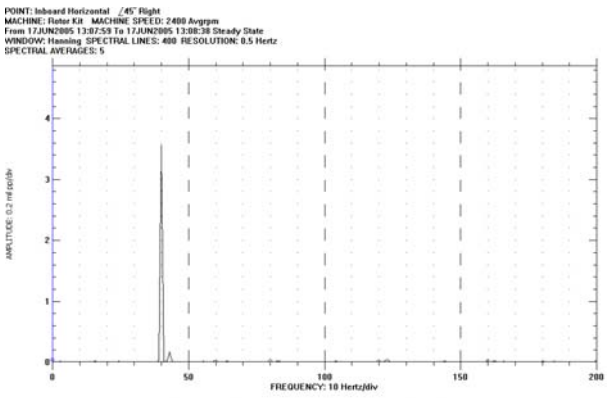

Figure 5.49. FFT at inboard 45° probe of healthy shaft running at 2400rpm with outboard AMB.

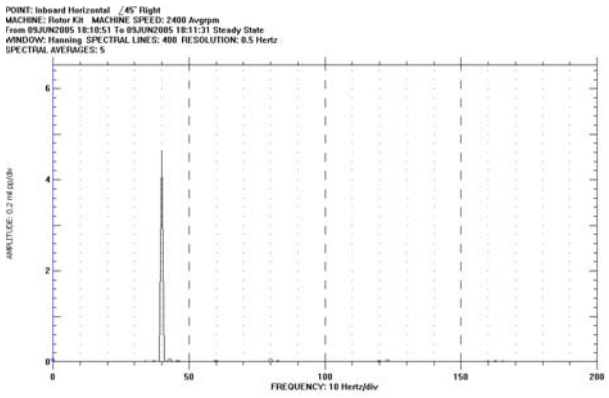

Figure 5.50. FFT at inboard 45° probe of 25% EDM notch running at 2400rpm with outboard AMB.

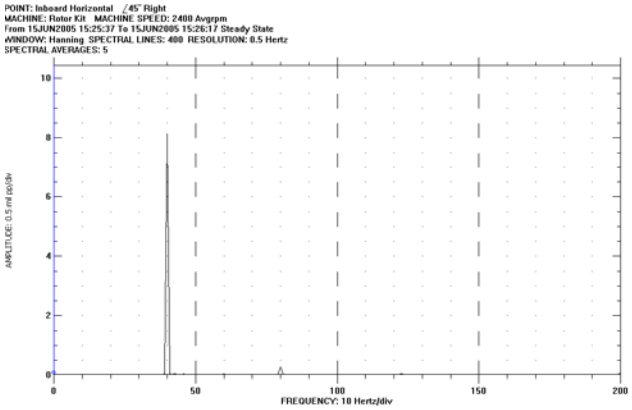

Figure 5.51. FFT at inboard 45° probe of 40% EDM notch running at 2400 rpm with outboard AMB.

Frequencies from the third mode at 2400 rpm stay consistent with that previously seen. The data for the inboard W axis probe can be seen in Figures 5.52, 5.53, 5.54, and 5.55. This data shows a 4 Hz decrease for the 25% EDM notch as well as 12.5 Hz drop for the 40% case. Similar to the 600 rpm speed, there seems to be a large amount of ripple especially in the 40% EDM case.

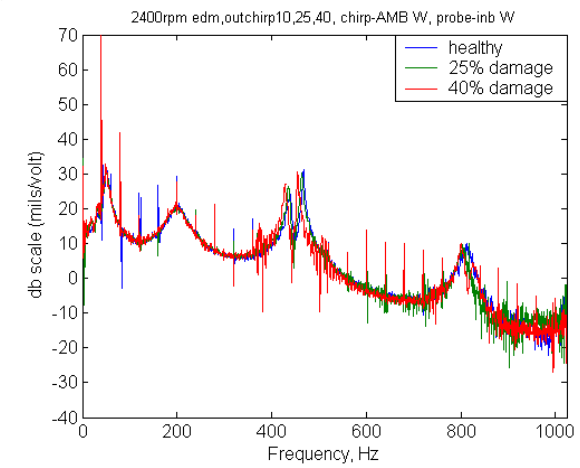

Figure 5.52. Full spectrum of an EDM notch at 2400 rpm measured at the 45° inboard probe with W-axis outboard AMB chirp.

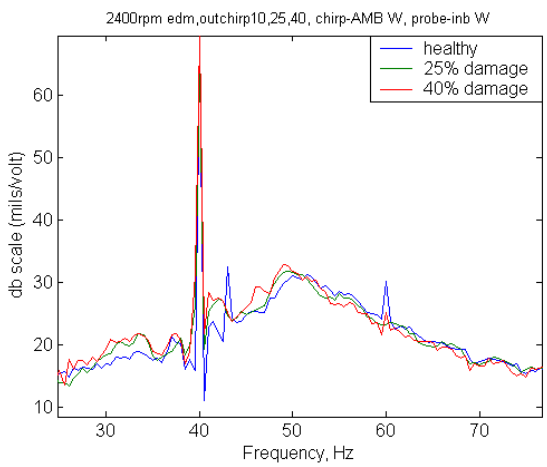

Figure 5.53. First mode of an EDM notch at 2400 rpm measured at the 45° inboard probe with W-axis outboard AMB chirp.

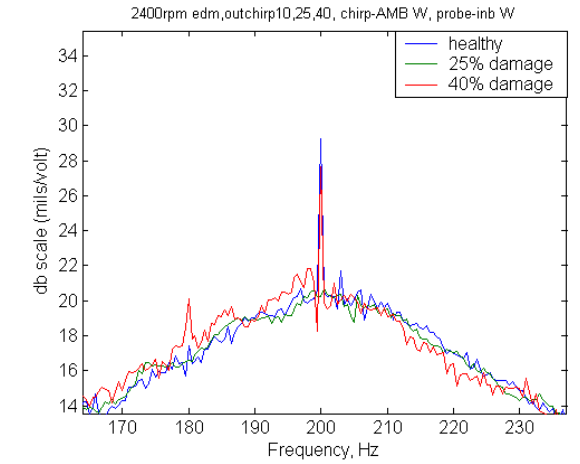

Figure 5.54. Second mode of an EDM notch at 2400 rpm measured at the 45° inboard probe with W-axis outboard AMB chirp.

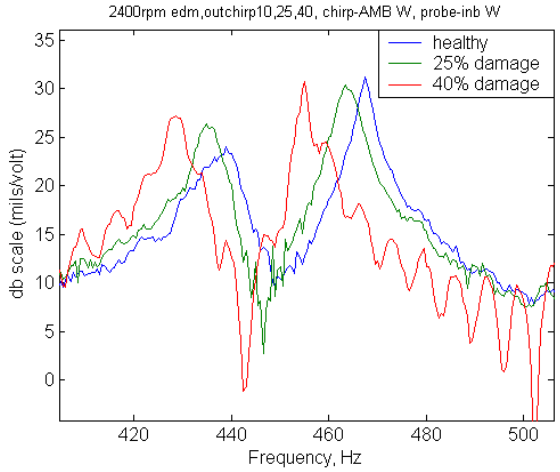

Figure 5.55. Third mode of an EDM notch at 2400 rpm measured at the 45° inboard probe with W-axis outboard AMB chirp.

The last FFT data at 5100 rpm is very clean with respect to running speed harmonics as shown in Figures 5.56, 5.57, and 5.58. Even the 2X component normally found in the 40% EDM notch case is not recognizable. Amplitudes of the 1X component do grow to 8.3 mils p-p from approximately 4.4 mils p-p.

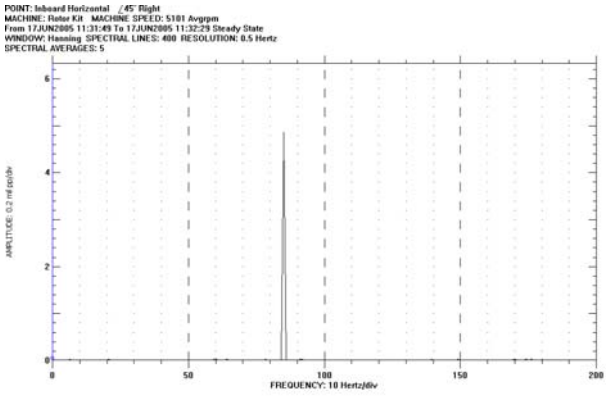

Figure 5.56. FFT at inboard 45° probe of healthy shaft running at 5100rpm with outboard AMB.

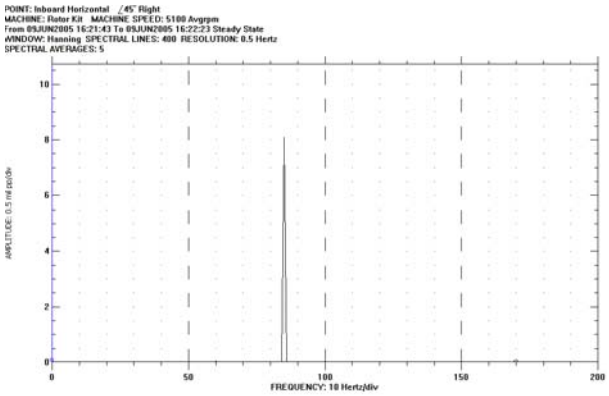

Figure 5.57. FFT at inboard 45° probe of 25% EDM notch running at 5100rpm with outboard AMB.

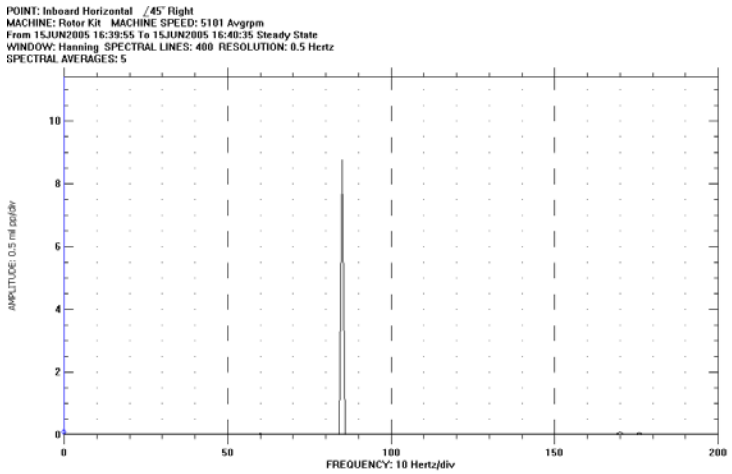

Figure 5.58. FFT at inboard 45° probe of 40% EDM notch running at 5100 rpm with outboard AMB.

The final FRF for the 5100 rpm case with outboard positioned AMB can be seen in Figures 5.59, 5.60, 5.61, and 5.62 for the full spectrum, first mode, second mode, and third mode, respectfully. Most of the ripple for the speed is gone, but the shifts in frequencies still exist. If the higher frequency peaks are used for third mode, then there is a 5 Hz change from the healthy shaft to the 25% EDM notch. The 40% EDM is actually lower than normal with a lower value of 9.5 Hz.

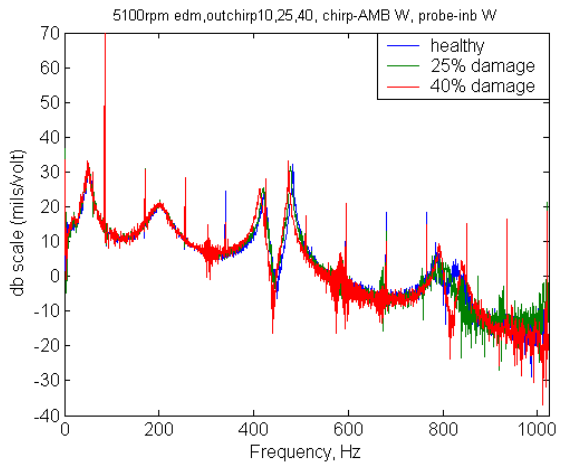

Figure 5.59. Full spectrum of an EDM notch at 5100 rpm measured at the 45° inboard probe with W-axis outboard AMB chirp.

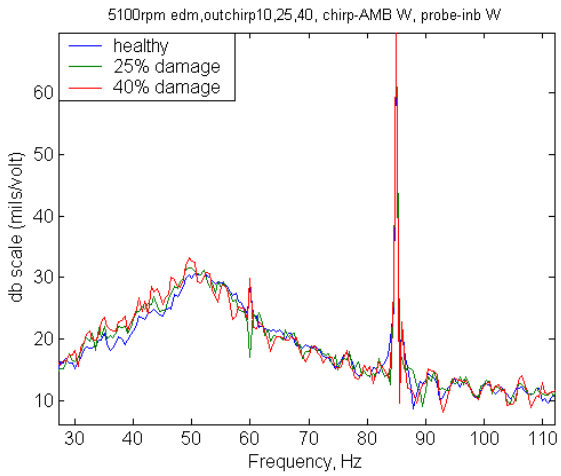

Figure 5.60. First mode of an EDM notch at 5100 rpm measured at the 45° inboard probe with W-axis outboard AMB chirp.

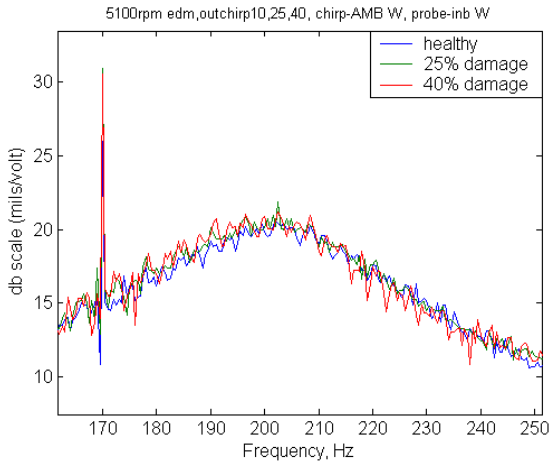

Figure 5.61. Second mode of an EDM notch at 5100 rpm measured at the 45° inboard probe with W-axis outboard AMB chirp.

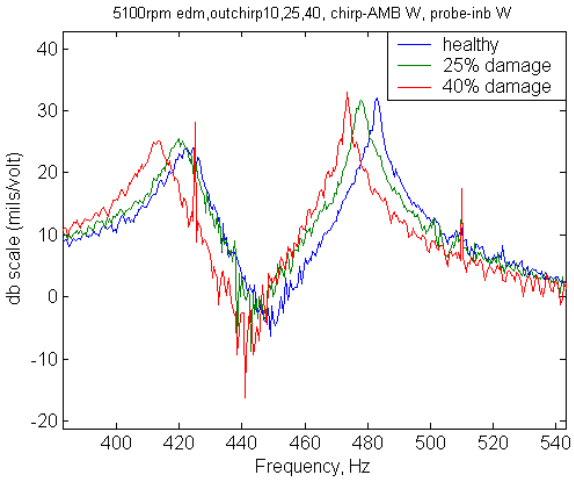

Figure 5.62. Third mode of an EDM notch at 5100 rpm measured at the 45° inboard probe with W-axis outboard AMB chirp.

Table 5.4. Change in third mode frequencies at 600, 2400, 5100 rpm for EDM notch depths at the inboard 45° probe shown in Hz and percent change for the outboard AMB.

	Shaft notch depth	
Speed (rpm)	*25%*	*40%*
600	3.5(-0.77%)	14.5(-3.17%)
2400	4(-0.86%)	12.5(-2.67%)
5100	5(-1.04%)	9.5(-1.97%)

*Values shown in Hz and percent change.

5.4 Chapter five summary

The static results for the midspan AMB are very similar to that of the large notch. When the notch faces either the axis of excitation or is 90° off axis direction, then the third mode shows very little to no signs of splitting, but if the EDM notch is rotated toward a different axis then the third mode splits. Some tests also show a large amount of ripple in the magnitude response with damage. A summary table of the static and dynamic results from the inboard and outboard AMB position with W-axis chirp can be seen in Table 5.5.

Table 5.5. Summary of static and dynamic third mode frequency shifts due to EDM notch depth of 25% and 40% for an inboard and outboard AMB set-up.

	Midspan AMB			**Outboard AMB**	
	Shaft notch depth			Shaft notch depth	
Notch Angle	*25%*	*40%*	Notch Angle	*25%*	*40%*
90°	3.5(-0.69%)	3.5(-0.69%)	90°	3.5(-0.77%)	6(-0.1.32%)
255°	4.5(-0.88%)	20.5(-4.03%)	255°	3.5(-0.77%)	19.5(-4.29%)
Speed (rpm)	*25%*	*40%*	Speed (rpm)	*25%*	*40%*
600	6.5(-1.27%)	13.5(-2.64%)	600	3.5(-0.77%)	14.5(-3.17%)
2400	7.5(-1.45%)	11.5(-2.22%)	2400	4(-0.86%)	12.5(-2.67%)
5100	10.5(-1.98%)	14.5(-2.73%)	5100	5(-1.04%)	9.5(-1.97%)

*Values shown in Hz and percent change.

Chapter Six

Conclusions

6.1 Summary of Thesis

This thesis introduces a method of modal analysis testing for a shaft supported in conventional bearings by using an Active Magnetic Bearing (AMB) as an actuator. The goal of this research was to prove that rotor health monitoring could be achieved while the shaft was rotating with the addition of the AMB. Many different types of faults exist for rotating machinery, but the two chosen for this work were shaft rub and shaft crack.

The test rig consisted of a shaft that is 24 inches (610mm) long and 0.625 inches (15.9mm) in diameter supported with ball bearings. An AMB was placed at approximately midspan with two position probes located nearby for AMB control. Four more proximity probes were located along the shaft with two at approximately ¼ span and two at ¾ span. A shaft rub was first investigated by applying contact from a brass screw at both the inboard and outboard proximity probe mount locations. To simulate cracks, a 0.025 inch (0.635mm) wide notch was made at midspan with progressive depths of 10, 25, and 40% of the shaft diameter. This method was later refined by using an EDM notch that was 0.0027 inches (0.069mm) wide for two depths of 25 and 40% the shaft diameter. All faults were tested with a chirp input into the W-axis of the AMB, but a gaussian input was also tested to compare results. The chirp data is mostly used in this thesis for consistency, but the gaussian input also gave similar results.

6.2 Conclusions

The following are results from rub and notch testing with an AMB W-axis chirp measured at the inboard 45° probe.

- With the shaft at 0 rpm, static rub testing shows an increase in mode frequencies and a decrease in the magnitude response as rub force increases. Static results also indicate that

a rub can be tracked along the axis of the shaft by comparing the magnitude differences from each proximity probe to that of a healthy baseline.

- Dynamic rubs show a bouncing or rippled magnitude response for both light and hard rubs. One can also monitor coherence because as rub pressure increases the coherence lowers.
- Static (0rpm) notch testing indicates no change in the first and second mode as notch depth increases, but the third mode shows a decrease in the frequency as notch depth increases. Third mode will also split in most cases when the notch is rotated to a direction other than that of the axis of excitation. The exception to this splitting is seen when the notch faces the axis of excitation and when the notch is rotated 90° away from the axis of excitation. A summary of the third mode frequency decrease from the healthy baseline can be seen in Table 6.1 for all three notch depths. Also shown in Table 6.1 is the percent change in third mode frequency.

Table 6.1. Static and dynamic third mode results for three progressive notch depths with a W-axis AMB chirp measured on the inboard 45° probe.

	Shaft notch depth		
Notch Angle	*10%*	*25%*	*40%*
90°	6.5(-1.26%)	4.5(-0.87%)	12(-2.32%)
255°	7(-1.35%)	9(-1.74%)	25(-4.84%)
Speed (rpm)	*10%*	*25%*	*40%*
600	3.5(-0.68%)	5.5(-1.07%)	19(-3.70%)
2400	2.5(-0.48%)	7(-1.35%)	18(-3.46%)
5100	3.5(-0.66%)	4(-0.75%)	13(-2.45%)

*Values shown in Hz and percent change.

- Dynamic notch testing indicates no changes in the first and second modes, but the third mode frequency decreases. This decrease can be minimal when comparing the 10% and 25% notch depth, but the 40% notch depth can cause a drop in frequency up to 19 Hz for the 600 rpm dynamic speed. Table 6.1 also summarizes the dynamic results.
- Static (0rpm) EDM notch testing shows similar results compared to the large notch. The first and second mode frequencies do not change, but the third mode frequency decreases as the EDM notch deepens. There is also a splitting of third mode when the notch faces any other direction besides the axis of excitation and 90° opposite excitation. These

results are also the same when the AMB is moved toward the outboard direction as seen in Table 6.2.

Table 6.2. Static and dynamic third mode results for two EDM notch depths of 25 and 40% for an inboard and outboard AMB set-up.

	Midspan AMB			**Outboard AMB**	
	Shaft notch depth			Shaft notch depth	
Notch Angle	*25%*	*40%*	Notch Angle	*25%*	*40%*
90°	3.5(-0.69%)	3.5(-0.69%)	90°	3.5(-0.77%)	6(-0.1.32%)
255°	4.5(-0.88%)	20.5(-4.03%)	255°	3.5(-0.77%)	19.5(-4.29%)
Speed (rpm)	*25%*	*40%*	Speed (rpm)	*25%*	*40%*
600	6.5(-1.27%)	13.5(-2.64%)	600	3.5(-0.77%)	14.5(-3.17%)
2400	7.5(-1.45%)	11.5(-2.22%)	2400	4(-0.86%)	12.5(-2.67%)
5100	10.5(-1.98%)	14.5(-2.73%)	5100	5(-1.04%)	9.5(-1.97%)

*Values shown in Hz and percent change.

- Dynamic EDM notch results are still similar to the large notch results and are shown in Table 6.2 for both the midspan and outboard AMB. Magnitude responses also begin to have ripples thru out the response as the notch depth increases. There are also changes in the fourth mode, but no trends, with respect to notch depth, have been found.

6.3 Future Work

There are lots of different directions to explore with this method of AMB excitation in conjunction with conventional bearing supports. Further work could be done involving notches at different locations along the axis of a shaft. More evaluation could be made to determine how well the EDM notch really mimics a crack, and is the notch breathing? Higher modes should also be investigated as well as the optimal excitation force. However, another direction of research might involve disk faults.

References

1. Bently, D. E., "Studies Reveal Physical Phenomena of Rotor Rubs," *Orbit*, Bently-Nevada Corporation, Minden, Nev, 1983.

2. Dimarogonas, Andrew D., "Vibration of Cracked Structures: A State of the Art Review," Engineering Fracture Mechanics, 55(5):831-857, 1996.

3. Ehrich, Fredric F., Handbook of Rotordynamics. Revised Ed. Kriegar Publishing Company, Malabar, FL, 1999.

4. Eisenmann, R.C., Sr., and Eisenmann, R.C., Jr., Machinery Malfunction Diagnosis and Correction, Prentice-Hall, Upper Saddle River, NJ, 1998.

5. Eshleman, R.L., "Detection, Diagnosis and Prognosis: An Evaluation of Current Technology," Proceedings MFPG 44, Vibration Institute, 1990.

6. Gasch, R. (1993). "A Survey of the Dynamic Behavior of a Simple Rotor with a Transverse Crack," *Journal of Sound and Vibration*, V 160 n.2, pp313-332.

7. Hope, R.W., Tessier, L.P., Knospe, C., and Miyaji, T., 1998, "Adaptive Vibration Control of Industrial Turbomachinery, 98-GT-405," *International Gas Turbine & Aeroengine Congress & Exhibition.*

8. Humphris, R.R., "A Device for Generating Diagnostic Information for Rotating Machinery Using Magnetic Bearings," Proceedings of MAG '92, Magnetic Bearings, Magnetic Drives, and Dry Gas Seals Conference & Exhibition, Alexandria, VA, pp123-135.

9. Inman, Daniel J., Engineering Vibration. 2nd Ed. Prentice Hall, New Jersey, 2001.

10 Iwatsubo, T., Arii, S., "Detection of a Transverse Crack in a Rotor Shaft by Adding External Force," Proceedings of ImechE Conference, 1992, paper #C432/093,pp275-482

11 Kasarda, M.E.F., Allaire, P.E., Humphris, R.R., Gunter, E.J., "The Effect of an Electromagnetic Damper on Vibrations in Rotating Machinery," Vibration Analysis-Analytical and Computational, ASME, DE-Vol. 37, September 1991, pp. 245-251.

12 Kirk, Gordon, R., Rotordynamics Class Notes. Fall 2002.

13 Mani, G., Quinn, D., Bash, T., Kasarda, M., Inman, D., Kirk, R.G., "Damage Detection of a Rotating Cracked Shaft Using an Active Magnetic Bearing as a Force Actuator," Conference Proceedings, 9th International Symposium on Magnetic Bearings (ISMB9), Lexington, KY, Aug3-6, 2004

14 Mitchell, J.S., Introduction to Machinery Analysis and Monitoring, Penn Well Publishing, Tulsa, OK, 1993.

15 Papadopoulos, C.A., Dimarogonas, A.D., "Coupled Vibration of Cracked Shafts," Journal of Vibrations and Acoustics, Oct 1992, Vol 114, pp461-467.

16 Pottie, K., Matthijssen, J. G., Norbart, C.J.J., Gielen, LJP., "Modal parameter estimation of rotating machinery,"IMechE, 1999.

17 Pusey, H.C., "An Historical View of Mechanical Failure Prevention," Proc. 11th Biennial Conference on Reliability Stress Analysis and Failure Prevention, ASME, 1995.

18 Reliability Direct. www.reliabilitydirect.com.

19 Sabnavis, G., Kirk, R. G., Kasarda, M., and Quinn, D., "Cracked Shaft Detection and Diagnostics: A Literature Review," Shock and Vibration Digest, Vol 36, No.4, July 2004 pp 287-296

20 Wicks, Al. Experimental Modal Analysis Class Notes. Spring 2004.

21 Zimmerman, David C., James, Jorge H III., Cao, Timothy T., "Experimental study of damage detection using modal, strain, and Ritz properties," Proceedings of IMAC '99, V1, SEM, Bethel, CT, USA. P 586-592.

Vita

Travis J. Bash was born on November 17, 1978 in Fort. Lauderdale Florida. His family then moved to Meadows of Dan Virginia in 1980 to provide a better location for a family. Travis graduated from Patrick County High School in 1996, and then from Patrick Henry Community College in 1998 with two associate degrees. He next moved on to mechanical engineering at Virginia Tech where he graduated in the spring of 2003 with a bachelor's degree. Travis decided to continue his education at Virginia Tech, and he finished his master's degree in mechanical engineering in December of 2005. He is now moving on to start a career with Caterpillar in Cary North Carolina.